Chair of Geology and Economic Geology

Doctoral Thesis

Evaluation of lumpy iron carriers by image processing

November 2018

Dipl.-Ing. Birgit Kain - Bückner, BSc

The ethics declaration must be signed, dated and enclosed in your thesis.

AFFIDAVIT

I declare on oath that I wrote this thesis independently, did not use other than the specified sources and aids, and did not otherwise use any unauthorized aids.

I declare that I have read, understood, and complied with the guidelines of the senate of the Montanuniversität Leoben for "Good Scientific Practice".

Furthermore, I declare that the electronic and printed version of the submitted thesis are identical, both, formally and with regard to content.

Datum 12.11.2018

Signature Author
Birgit, Kain - Bückner
Matriculation Number: 00335004

Abstract

Lumpy iron carriers are tested in many ways according to their physical, mechanical and chemical properties. However, the mineralogy and textural attributes are not part of a testing program for determination of the reducibility and behavior during the reduction process in the blast furnace. The mineral abundance, crystal size and shape, as well as the porosity play important roles for the reduction of lumpy iron carriers. The simplified pathway of the reduction is as follows: limonite -> hematite -> magnetite -> wuestite -> metallic iron. To determine the influence of the mineralogical and petrographic parameters on the reducibility, the image processing software VisuMet was developed. The algorithms are based on detailed microscopic investigations of twenty lumpy iron carrier samples before and after ISO-4695 testing.

Eight iron ore samples derive from different banded iron formation deposits in Australia, Africa, South America, China and India. In addition, a magmatic iron ore from the Kiruna deposit, Sweden, was evaluated. The iron ore samples can be divided into three groups due to their contents of limonite, hematite and magnetite. One group consists of lumpy iron ores with a certain amount of limonite and hematite. Another group comprises high grade hematitic iron ores and the last group consists of a magnetite ore from Kiruna. The nine investigated pellet samples are from world-wide traded pellet brands and mainly consist of hematite, magnetite and glass. The major differences affecting the reducibility of the pellet samples are pore size and distribution. The two sinter samples from Austria comprise the phases hematite, magnetite, calcio- and silicioferrites and glass.

VisuMet processes micro-images of polished sections of the samples and provides, beside the mineral abundance, a simulation of the reduction progress according to the shrinking core model and the Danielsson algorithm. It calculates the characteristic area degradation curve of lumpy iron ore samples and performs statistical analyses of pore sizes larger than 2 µm for pellet samples. The evaluations are compared to the results of ISO-4695 reduction tests of the respective samples. It was found that iron ores with a high proportion of limonite are reduced faster than pure hematite and magnetite ores. The rate of the area degradation of the lump ore samples correlates with the weight loss rate of the reduction test by a determination coefficient of 92 %. The mean equivalent pore diameter of the pellet samples and the time needed to reach 80 % reduction degree correlate with a coefficient of 91 %. However, the reduction rate correlates with a determination coefficient of 67 % with the mean equivalent pore diameter. The phase classification and quantification by VisuMet were compared to manual point counting of six polished sections from different lumpy iron carriers. The mineral abundance determination of VisuMet was well in accordance with optical microscopy.

Zusammenfassung

Stückige Eisenträger werden unterschiedlichen Testverfahren bezüglich ihrer physikalischen, mechanischen und chemischen Eigenschaften unterzogen. Allerdings ist die Mineralogie und das Gefüge nicht Bestandteil der üblichen Testverfahren, die Aufschluss über den Reduktionverhalten im Hochofen geben. Der Mineralbestand, die Kristallgröße und -form, sowie die Porosität, spielen eine entscheidende Rolle bei der Reduktion der stückigen Eisenträger. Der vereinfachte Reduktionsweg ist folgender: Limonit -> Hämatit -> Magnetit -> Wüstit -> metallisches Eisen. Um den Einfluss der mineralogisch-petrographischen Eigenschaften auf die Reduzierbarkeit abzubilden, wurde die Bildverarbeitungssoftware VisuMet entwickelt. Die Grundlage für die Algorithmen sind detaillierte mineralogisch-petrographische Untersuchungen von 20 stückigen Eisenträgern vor und nach einem ISO-4695 Reduktionstest.

Acht Eisenerzproben stammen von gebänderten Eisenerzlagerstätten aus Australien, Afrika, Südamerika, China und Indien. Außerdem wurde eine Probe der Lagerstätte Kiruna in Schweden verwendet. Die Eisenerzproben können in drei Gruppen hinsichtlich ihres Modalbestandes an Limonit, Hämatit und Magnetit eingeteilt werden. Eine Gruppe besteht aus Stückerzen mit einem gewissen Anteil an Limonit und Hämatit, eine weitere aus überwiegend hämatischen Erz und die Probe von Kiruna besteht aus magnetitischen Erz. Die neun untersuchten weltweit-gehandelten Pelletproben bestehen vorwiegend aus Hämatit, Magnetit und einer Glasphase. Das Hauptunterscheidungsmerkmal hinsichtlich der Reduzierbarkeit von Pellets ist jedoch die Porengröße. Die zwei untersuchten Sinterproben aus Österreich bestehen aus den Phasen Hämatit, Magnetit, Calcio- und Silizioferrit und Glas.

VisuMet verarbeitet Mikrobilder der polierten Anschliffe der Proben und liefert neben dem Modalbestand auch eine Simulation der fortschreitenden Reduktion anhand eines Schalenabbaumodells mittels Danielsson Algorithmus. Es berechnet für Eisenerzproben eine charakteristische Flächenabbaukurve und für Pelletproben eine statistische Auswertung der Porengröße > 2 µm. Diese Auswertungen wurden mit den Ergebnissen der ISO-4695 Reduktionstests der Proben verglichen. Es stellte sich heraus, dass Stückerze mit einem hohen Anteil an Limonit schneller reduzieren als reine Hämatit- und Magnetiterze. Die Rate des Flächenabbaus der Stückerzproben korreliert mit der Rate des Gewichtsverlustes beim Reduktionstest mit 92 %. Der mittlere äquivalente Porendurchmesser der Pelletproben korreliert mit einem Bestimmtheitsmaß von 91 % mit der Zeit, die für das Erreichen von 80 % Reduktionsgrad benötigt wird. Die Reduktionsrate hingegen korreliert nur zu 67 % mit dem mittleren Porendurchmesser. Die Phasenklassifizierung und -quantifizierung mittels VisuMet wurde mit einer händischen Punkteauszählung von sechs Anschliffen gegenübergestellt. Der Modalbestand stimmt zu 99 % überein.

Inhalt

List of Tables

List of Figures

1. Introduction

Many studies in recent years have focused on the chemical composition and technical parameters only to determine certain quality ranges for lumpy iron carriers like iron ores, pellets and sinters. Pellets are agglomerated iron ore fines. They are produced by rolling moist fines to balls and are shortly burned at ca. 1300 °C. Sinter is produced directly at iron making plants and the raw material consists mainly of iron ore fines, coke and flux. The composition is adjusted to specific blast furnace needs. The mixture is loaded on the sinter strand and is lighted. The flame front burns through the ca. 80 cm thick bed. The material is almost entirely molten and sticks together to form the sinter cake. After crushing and screening the sinter is transported to the blast furnace for charging. The blast furnace is the most frequently used iron making process route worldwide to produce pig iron. Lump iron ore, pellets, sinter, coke and flux are charged on the top of the blast furnace and heated up. The cohesive zone (900-1350 °C) is the region where the first melt appears (Babich 2008). The reduction reactions produce metallic iron droplets and slag. At the bottom of the hearth of the blast furnace the molten metal is collected and frequently tapped. The blast furnace produces pig iron and slag, beside top gas and flue dust.

The production of iron ore has been risen in the last decades, but the reserves of high-grade iron ores (> 60% Fe) have fallen dramatically. Now, low-grade ores or ore mixtures are used for iron production and their behavior can differ. The prediction of the reduction behavior during the process is important for a smooth operation. In addition, economical aspects, such as coke consumption, CO_2 emissions, etc. are getting more and more in focus. Normally, iron carriers are analyzed by different standard procedures. Some of them are the tumbler index, the reducibility or the reduction disintegration index. They are developed to predict the behavior of the material in different temperature zones of the blast furnace. Different researchers demonstrated that these standard procedures cannot answer all questions for the further usage of the raw material (Loo and Bristow 1998; Geerdes et al. 2015).

The mineralogy and texture, as well as the pore size distribution have not received much attention to determine the characteristics of lumpy iron carriers. The iron-bearing minerals have different reducibility and transform to metallic iron in the simplified path: limonite -> hematite -> magnetite -> wuestite. So, the grain size, the mineral distribution and the different textural features influence the reduction progress (Clout 2003; Lu 2015).

In general, the mineral abundance is determined by the optical microscopy point counting method on polished sections. This is very time consuming and the result depends to a certain extent on the responsible mineralogist. Today, two semi-automated systems are available to support the characterization of iron bearing materials. First are the scanning-electron microscope based systems and second the optical microscope based ones (Donskoi et al. 2013; Pirard et al. 2007). Both process micro-images using a software, but they do not evaluate the lumpy iron carriers' reducibility.

As a consequence, the research on this topic started in 2005 to characterize lump and fine iron ores by optical microscopy in a different way (Mali and Spuida 2013). They developed the prototype of VisuMet, an image processing software, to evaluate iron ores regarding their reduction behavior. A K1-Met project (2012-2015) was launched to continue the idea of evaluating iron carriers by image processing. This thesis describes the further development of the different algorithms and presents the results from the evaluation of different lumpy iron ores, pellets and sinters compared to the results of standard reduction tests. The standard reduction tests were carried out at the Chair of Ferrous Metallurgy (Montanuniversität Leoben, MUL). The preparation of the samples and the development of the software were made at the Chair of Geology and Economic Geology (MUL). The samples were supplied by the industrial partners voestalpine Linz GmbH and Primetals Technologies Austria GmbH.

After a short summary of the relevant metallurgical aspects, the mineralogy of the lumpy iron carriers is discussed in detail and the basics of optical image processing are given. The methodology chapter assembles the metallurgical, technical and mineralogical aspects. The procedure of algorithms and the comparison to the point-counting method is described, too. The results and the comparison to standard reduction tests are discussed at the end.

2. Ferrous metallurgical aspects

This research work focuses on lumpy iron carriers like lump ore, pellets, and sinter. This kind of raw material is commonly used in the blast furnace, by different direct reduction and smelting reduction techniques to produce crude iron. Further, a reducing agent and fossil energy are necessary. The following section gives an overview of the iron production loop, the requirements of the burden material and the lab testing methods.

2.1. Iron production loop

Iron (Fe) is a base metal with the atomic number 26. It exists in different oxidation states from Fe^{-2} to Fe^{+6}, while Fe^{+2} and Fe^{+3} are the most common ones. Iron has the tendency to oxidize in atmospheric conditions, so it is rarely found in its native form on the Earth's surface. It makes up about five mass-percent of the Earth's crust. The inner and outer cores are suspected to consist of an iron-nickel alloy. Elemental iron occurs in meteoroids and first manufactured finds were dated as 4000 before Christ (BC). The primitive production of iron by the Hittites began in Anatolia sometime after 1500 BC. The smelting of iron required a bloomer furnace with charcoal fire. This technique produced a spongy, porous mass of iron with slag and bits of charcoal. By the addition of flux (e.g. crushed limestone) a bloom of iron was formed and ready to be further processed with blacksmith methods.

Today iron making is a highly developed and complex process. It is estimated that 98 % of the iron ore shipped worldwide is consumed in iron and steel making routes. Although the demand for steel has declined since the economic crisis in 2008, the crude steel production rose 41 % in the last 10 years (www.worldsteel.org). In the last 20 years, the iron ore production has more than tripled from about 1 Billion tons (Bt) to 3.4 Bt until 2015. In 2016 has fallen to 2.2 Bt (USGS 1998, 2017). Iron carriers are used in three major process routes (Figure 1), whereas the blast furnace route produces 70 % of the crude steel worldwide (Geerdes et al. 2015):

- Blast furnace route (BF)

- Direct reduction process route (DR)

- Smelting reduction route (SR)
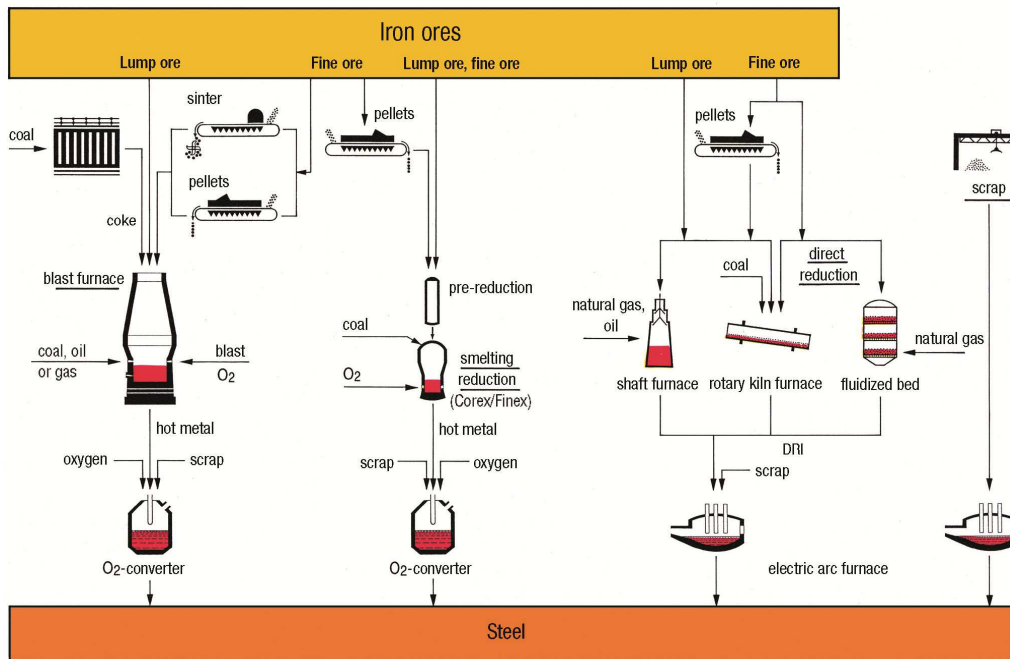
Figure 1: Overview of the different iron and steel making routes (BF, SR, DR, ER), after Stahl-Zentrum (2017).

Another possibility to produce crude steel is the electric arc furnace route (ER) (Figure 1, right). This process uses metallic scrap and few iron carriers as raw material, so it is not discussed in detail here. All processes lead to liquid hot metal or solid iron sponge and both products are further processed. The properties of this material highly influence the quality of the later produced steel.

The blast furnace route uses lump iron ore, ore agglomerates (pellets and sinter), coke and other reducing agents (such as coal, oil or gas) to produce liquid hot metal. The burden material is charged at the top of the blast furnace and moves downwards. There the material is warmed up to 600 °C. The reducing gas is generated through the tuyeres (nozzles) by the injection of the hot blast (Figure 2). The iron carriers are transformed in the upper parts by indirect reduction with gaseous CO and by direct reduction with solid carbon in the lower zones. The material starts to melt at 1000 to 1100 °C (Babich 2008). The liquid slag and molten iron droplets are generated and move downwards. Most of the other elements gather in the slag. The molten iron accumulates in the so-called hearth, where it is periodically tapped. The two liquid phases are separated due to their different density. Obviously, many different processes and chemical reactions take place in this counter-current operation and are directly and indirectly dependent on the behavior of the lump burden material.
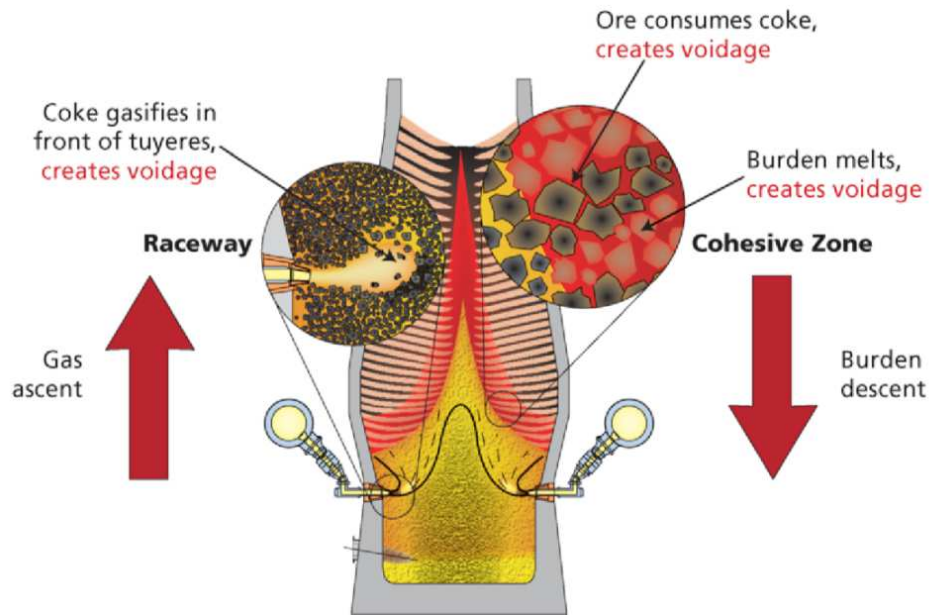
Figure 2: Cycle within the blast furnace after Geerdes et al. (2015).

The direct reduction route produces solid sponge iron directly from iron ores and pellets. The most applied process is the MIDREX®-process (Midrex Technologies Inc. 2014). More than half of the direct reduced iron (DRI) production worldwide comes from MIDREX® plants (World Steel Association, 2017). The product has a high metallization degree (over 85 %) and will be further processed to hot briquetted iron (HBI). In the electric arc furnaces, the material is mixed with scrap to produce crude steel. In addition, the DRI can be charged directly to the subsequent steelmaking facility in the hot condition. The reduction takes place at lower temperatures as in the blast furnace (800-1050 °C). Hydrogen and carbon monoxide are the reductants derived from natural gas or coal.

The smelting reduction processes, such as COREX® or FINEX®, produce molten iron by gasification of coal as an energy source and a reducing agent. The idea is to produce liquid iron economically at low capacity using coal directly. The COREX® process is the most advanced process. It separates the iron ore reduction and melting steps into two reactors: first the melter – gasifier, where the reducing gas is generated from coal and second the reduction of iron ore, which occurs in a shaft furnace. The reducing gas consists of carbon monoxide (65-70 %), hydrogen (20-25 %) and carbon dioxide (2-4 %) (Flickenschild et al. 2013). The hot gas is mixed with cooling gas to obtain a temperature of 850-900 °C. The hot metal and slag are discharged by conventional tapping procedures periodically. The FINEX® process, however, uses three fluidized bed reactors (R1-R3) for the reduction of fine iron ore, whereas the COREX® process charges lump ore and pellets in a shaft furnace (Figure 3). A standardized method by a lab-scale fluidized bed reactor was developed by Skorianz et al. (2016). This was followed by a research of the structural evolution of worldwide traded fine iron ores during under fluidized bed conditions (Pichler et al. 2016).
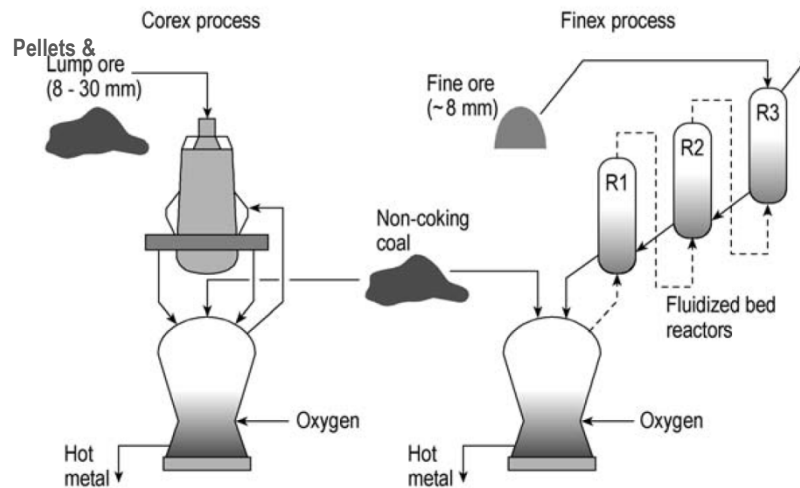
Figure 3: The schematic concept of the COREX® process compared to the FINEX® process, modified after Flickenschild et al. (2013).

The research group found out that the morphological structures of the iron-bearing minerals limonite, hematite and magnetite have a significant influence on the reducibility (Pichler et al. 2016). The transformation of the iron oxides to metallic iron at the reduction process will be discussed in detail in chapter 3.5.

2.2.   Requirements of ferrous burden material

A trouble-free production of metallic iron depends on specific requirements of the ferrous burden material. Parameters like chemical composition, grain size distribution, mechanical strength or reducibility properties have to be within certain ranges to ensure a constant quality of the crude steel. It begins at the mining site and continues to the agglomeration processes (pelletization and sintering) of the iron ore. The importance of the agglomerated iron material has been raised in the last decades due to the depletion of high-grade iron ore resources. In modern blast furnaces 10-20 % lump ore and 10-20 % pellets are used, the remaining percentage 60-80 % is sinter material (Lu 2015). This distribution varies from blast furnace to blast furnace. In Austria, the use of pellets is about 20 % and sinter produced from the local siderite ore of the Erzberg deposit makes up to 60 %.

Three major categories reflect the requirements for ferrous burden material:

- *Chemical requirements* are the iron content, gangue amount (SiO_2, CaO, MgO, and Al_2O_3) and the proportion of undesired elements (P, S etc.).

- *Physical and mechanical properties* referring to the strength and size of the material to be stable under certain conditions (temperature, transport or charging).

- *Metallurgical properties* refer to aspects concerning the reduction process, e.g. reduction speed, sticking, swelling, degradation and disintegration.

The iron content is the most important parameter for burden material. A reduction process has to be as economical and cost efficient as possible, so the iron content is required to be high (over 58 %, Geerdes et al. 2015). For direct reduction processes, the iron content has to exceed 67 % (Lu 2015). The higher the Fe content the less energy is needed. If the iron content is low, the amount of gangue material increases, as well as the ratio of undesired elements. The blast furnace process can handle a high amount of gangue better than direct reduction facilities. The parameters, which reflect the chemical properties beside the Fe content, are the total amount of gangue and the basicity. The most used value for basicity (B_4) is the ratio of basic oxides ($CaO + MgO$) to acidic oxides ($SiO_2 + Al_2O_3$). To counter-act acidic gangue material, more basic flux material is needed. Gangue contents lower than 7 % are acceptable regarding lump ore, whereas for pellets a silica content of 4-6 % is typical. Sinter is always produced nearby the blast furnace and is adjusted to the needs of every single blast furnace. Therefore general operational parameters cannot be given in detail, but are more or less the same as for lump ore. Free moisture and a high loss on ignition (LOI) during heating are undesirable in all charging materials.

The physical characteristics of the feed material depend on the grain size, its distribution, mechanical strength and degradation behavior. All these parameters influence the bed permeability for the reducing gasses. Mechanical strength is required to stabilize the column of charge material. The grain size and distribution are two of the most important parameters in a shaft furnace facility. A high amount of fines will limit the productivity and increases the demand of reducing agent. The grain size distribution has to be in a certain coarse range. For lumpy iron ore used in blast furnaces, the grain size should have a range of 6 to 25mm and the portion of fines should be less than 3 % below 5 mm (Geerdes et al. 2015).

Metallurgical properties concern effects that occur during the reduction process. The reducibility (ability to release oxygen) is one of them. In addition, swelling and sticking can occur. Swelling, defined as the volumetric expansion during heating, is linked particularly to pellets. Sticking can occur in the bed by agglomeration of reduced iron ore particles above 610 °C. A literature review of this phenomenon is given by Komatina and Gudenau (2004).

2.3. Fundamentals of reduction from iron oxide to metallic iron

Reduction is the release of oxygen from oxide with its transformation to the element or an oxide with less oxygen than before (Babich 2008). To remove the oxygen from the iron compound in an economic way a gaseous or solid reductant is needed. This reductant catches the oxygen and extracts it from the system. The reaction takes places in two steps: first decomposition of the metal oxide and second by fixing oxygen to the reductant. In formula: $MeO_2 + R = Me + RO_2$
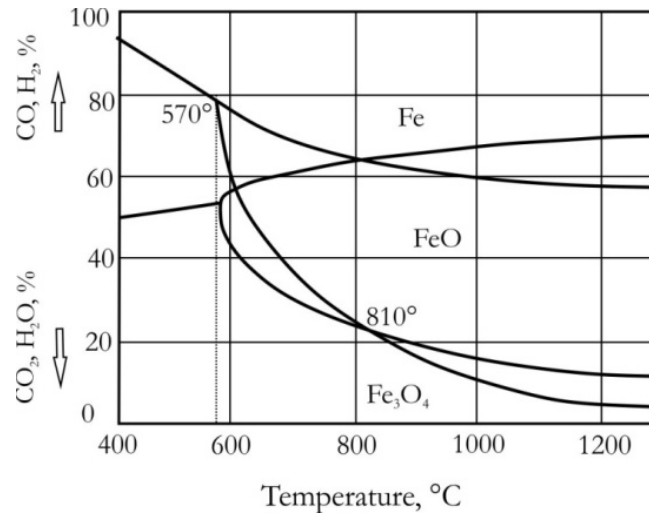
Figure 4: Baur-Glaessner diagram of CO-CO$_2$ and H$_2$-H$_2$O mixtures with magnetite, wuestite and iron, modified after Babich (2008).

The oxygen potential of MeO$_2$ must be higher than one for the reductant R (negative Gibbs Energy) to proceed the reduction. The reduction with the reductants CO and H$_2$ (with CO$_2$ and H$_2$O as products) is called indirect reduction, whereas the reduction by carbon with the formation of CO as final product is called direct reduction. The sum of direct and indirect reduction is equal to 100 %. A balance between indirect and direct reduction at the BF ensures a minimum of coke consumption (Babich 2008). This balance (and further improvements of the process) can be achieved by considering the thermodynamic and kinetic aspects of the reduction reaction by selecting an appropriate model. The Baur-Glaessner diagram (Figure 4) describes the different phases in the system Fe-C-O$_2$-H$_2$ and the stability fields of the iron oxides as well as metallic iron as a function of different mixtures of CO$_2$, H$_2$O and CO, H$_2$.

Microscopic investigations on partly reduced iron ores and pellets clearly demonstrate that the reaction zone moves as a sharp front from the outer surfaces into the particle. The shrinking-core model describes this reaction close to reality (Levenspiel 1999) (Figure 5). The reduction proceeds in a topochemical way (Szekely and Evans 1970; Habermann et al. 2000; Noguchi et al. 2013).
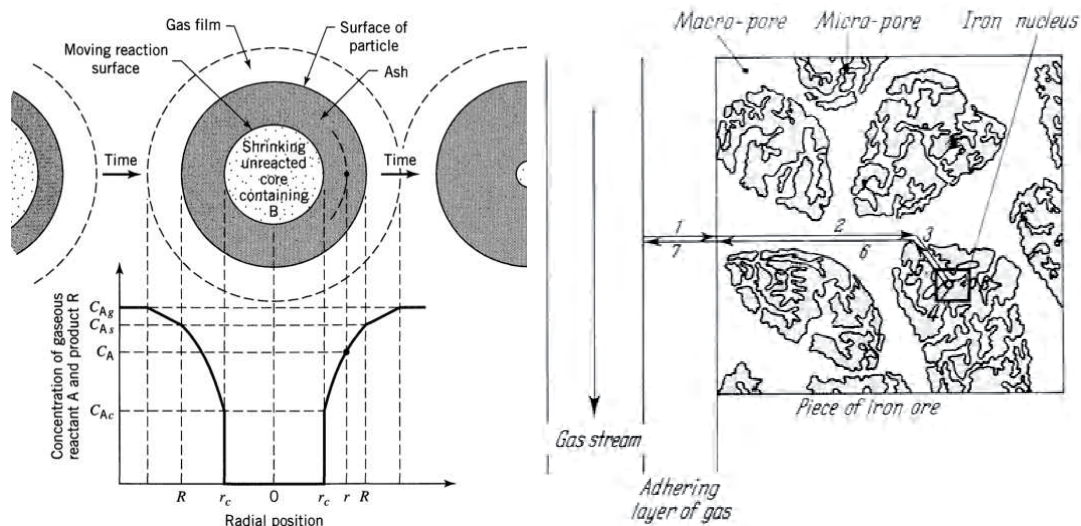
Figure 5: Shrinking-core model after Levenspiel (1999) and Bogdandy and Engell (1967).

This model describes an idealized way of the different stages in five individual steps. The heterogeneous reduction reaction in the solid state starts at the surface of the ore particles through a gas-phase flow. At the boundary layer, the reducing gas is consumed, and the oxidized gases are transported away from the reaction front (mass transfer via gas diffusion, step 1). The reducing gas diffuses through the pores (step 2 and 3) and the oxidized gas returns along the same way (step 5). The oxygen is separated from the oxide lattice and formation of new solid phases (lower iron oxides or metallic iron) starts (Bogdandy and Engell 1967). The reaction between a gaseous material and a solid particle is regarded for simplicity to be a reaction of unchanging size (Szekely and Evans 1970). The steps 2, 3 and, 5 can concise as pore diffusion. To sum up, the main rate controlling mechanisms are the mass transport (gas diffusion), the pore diffusion and the boundary layer reaction. In reality, the rate controlling factor of the reduction in industrial processes will always be a mixture of the three listed above and will change over time during the process.

The iron reduction in the BF is a complicated process with many influencing factors. The prediction of the ferrous burden behavior in the BF is a challenge and a lot of research has been carried out to develop lab scale testing methods and standardized tests (Hanel 2014; Skorianz et al. 2016). However, the prediction cannot be described with a single value. It is only one part of the puzzle. The main influencing factors, concerning the reducibility, are listed:

- *Temperature* influences the pore diffusion and the chemical reaction. A higher temperature leads to a better reduction procedure.

- *Grain size* determines the specific surface and determines the kinetic rate.

- *Gas composition and pressure* affects the reduction rate.

- *Chemistry and basicity* influence the reaction process.

- *Porosity and pore size distribution* influences the mechanical strength and the pore diffusion.

- *Mineralogy* (crystal size, type of mineral, texture) of the charging material influences the reduction rate and mechanical strength.

2.4. Lab testing methods of ferrous burden material

A wide range of physical tests was developed to characterize the ferrous burden material and predict its behavior during the reduction process. Most of them are ISO standardized. Every different zone of the furnace has different quality requirements and testing methods. The most important and widely used ones will be discussed here.

The *tumbler index* (TI, ISO-3271) reflects the resistance to degradation during handling, transportation and charging (cold strength). It gives weight percentage of the material > 6.3 mm after the tumbling treatment in which 15 kg of sized ferrous material is tumbled in a 1 m diameter drum for 200 turns at a speed of 25 rpm. The weight percentage of the material < 0.5 mm after tumbling is an indication of the degree to generate fines. The test is suitable for lump, pellets, and sinter. Furthermore, pellets are tested to determine the cold compression strength (ISO-4700) by compressing a single pellet between two plates until the pellet cracks (at least 60 pellets as a test sample). A crushing strength of 200 kg is desirable for pellets.

ISO 4696-1 was developed to evaluate the degree of fines generation from the ferrous material when reduced under similar conditions to those in the low-temperature zone of the blast furnace. It is called the low-temperature disintegration tendency (RDI – reduction disintegration index). A sized sample of 500 g is reduced isothermally at 550 °C for 30 min in a fixed bed with a gas mixture of 30 % CO +70 % N_2. After cooling in N_2 the partially reduced sample is tumbled for 30 min with 30 rpm and then sieved at 6.3 mm, 3.15 mm and 500 μm. RDI gives the proportion of the mass of the sieved fractions to the initial mass prior to tumbling. A high RDI value corresponds to greater generation of fines.

The *reducibility* (R, ISO-4695) describes the ability of a ferrous material to release oxygen and is designed for requirements of shaft furnaces. It is performed in a vertical reduction facility. A sample portion of 500 g is heated up to 900 °C and is reduced isothermally for 180 min in a fixed bed with a gas mixture (equal to RDI testing). R is determined by the ratio of the initial oxygen within the sample portion to the mass of removed oxygen in percentage by weighting the sample continuously during the test. The R_{80} value expresses the time needed to gain a reduction degree of 80 %. The reducibility index (RI) represents the reduction rate given in [%/min] calculated with the formula RI = $(dR/dt)_{40}$= $33.6/(t_{60}-t_{30})$. The t_{60} and t_{30} is the time needed to gain a reduction degree of 60 % and 30 %. RI should be high (over 0.8), whereas R_{80} should be low.

3.   Mineralogy of selected lumpy iron carriers

The following chapter deals with the investigated samples of lumpy iron ores, pellets and sinter. The main minerals and their characteristics will be described, as well as the microtexture. Finally, the reduction path of the different iron oxides and microtextures during the ISO-4695 test is outlined. The descriptions are based on the microscopical analyses of polished sections, made from the samples before and after the ISO-test. The ISO-tests were performed at the Chair of Ferrous Metallurgy (MUL).

3.1.   Iron oxides

The most common and mineable iron ore minerals are listed in Table 1. Iron ores often represent a mixture of these minerals, intergrown with gangue minerals like quartz or carbonates. However, the texture or microstructures are complex and vary within iron ore deposits and are related to the ore genesis.

The shape of crystals of the iron minerals is either described as idiomorphic, hypidiomorphic or xenomorphic. The crystal size distribution is defined as small (<10 μm), medium (10-20 μm) and coarsely (>20 μm) crystalline. Very fine/small crystals have a size smaller than 2 μm. The porosity, as well as the micro-pores inside the crystals, also has to be taken into account. These characteristics are important for the reduction behavior. The texture of the iron ore, including the morphology of the iron oxides, is responsible for structural evolution during the reduction process and influences the re-crystallization (transformation) process. This evolution will be discussed in detail in chapter 3.5.

Table 1: The main iron minerals (oxide and carbonate) with selected physical and chemical properties.

	formula	Fe_{tot} [%]	structure	melting point [C°]	trace elements
Hematite	$Fe^{3+}_2O_3$	70.0	trigonal	1565	Ti, Al, Mn, H_2O
Magnetite	$Fe^{2+}Fe^{3+}_2O_4$	72.4	isometric	1590	Mg, Zn, Mn, Ni, Cr, Ti, V, Al
Limonite*	$Fe^{3+}O(OH)\cdot nH_2O$	62.6	amorphous to cryptocrystalline	decompose	Mn, Al, Mg, Ca
Siderite	$Fe^{2+}CO_3$	48.2	trigonal	decompose	Mn, Mg, Ca, Zn, Co

mixture of goethite and lepidocrocite

Hematite is grey-white in reflected polarized light and is the brightest main mineral phase in iron ores and its products. It shows red internal reflections, which depends on the grain size. The color under reflected light can vary from white to steel-blue or gray-blue due to bireflectance. Hematite is divided into different subtypes depending on crystal size, porosity, and shape. The primary hematite characteristics based on the genesis of the crystal growth (i.e. chemical precipitation and later metamorphism), whereas the appearance of secondary hematite (dehydration of limonite or oxidation of magnetite) depends on the host mineral and the conditions at the transformation (Figure 6). Since hematite is formed under so many various conditions, the origin may be complicated to backtrace.
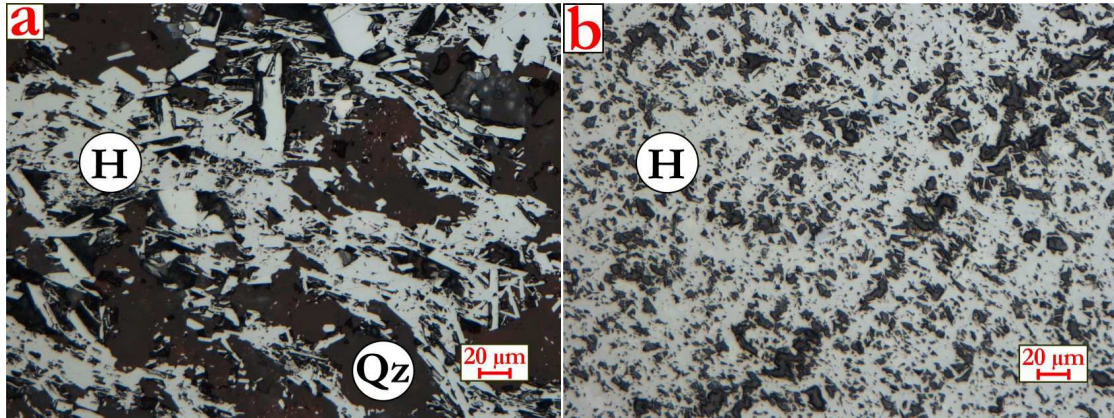
Figure 6: a) Medium sized hypidiomorphic to idiomorphic hematite (H) with quartz (Qz); b) very fine to small xenomorphic hematite (H); both from different BIF type deposits.

A common subtype of hematite is the so called microplaty hematite. In this thesis a microplaty hematite is defined as a secondary idiomorphic small (<10 μm) hematite, which is present in needle, rhombic or blocky shapes.

Martite is a variety of hematite, which pseudomorphs after magnetite and is commonly found in iron ores. This replacement proceeds in sectors from the octahedral faces or cleavage planes. The oxidation of magnetite to martite results in a characteristic trellis structure (Figure 7). A progressive recrystallization of the martite produces an interlobate to polygonal extinction pattern (Hagemann 2008) (Figure 8). Another type of martite is only recognizable under crossed nicols and has a lamellae structure (Figure 8).
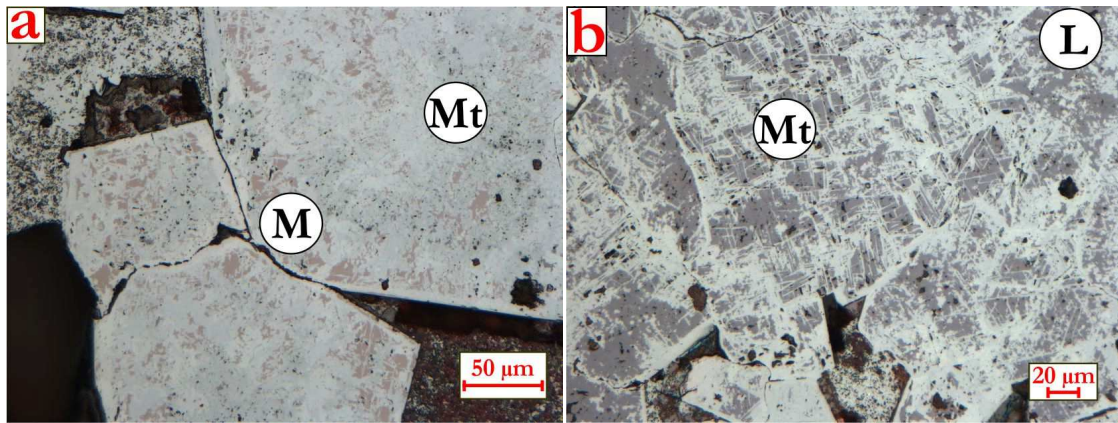
Figure 7: a) Coarse martite (Mt) with relics of magnetite (M, brown); b) Coarse martite (Mt), where the former magnetite is replaced by grey limonite (L).
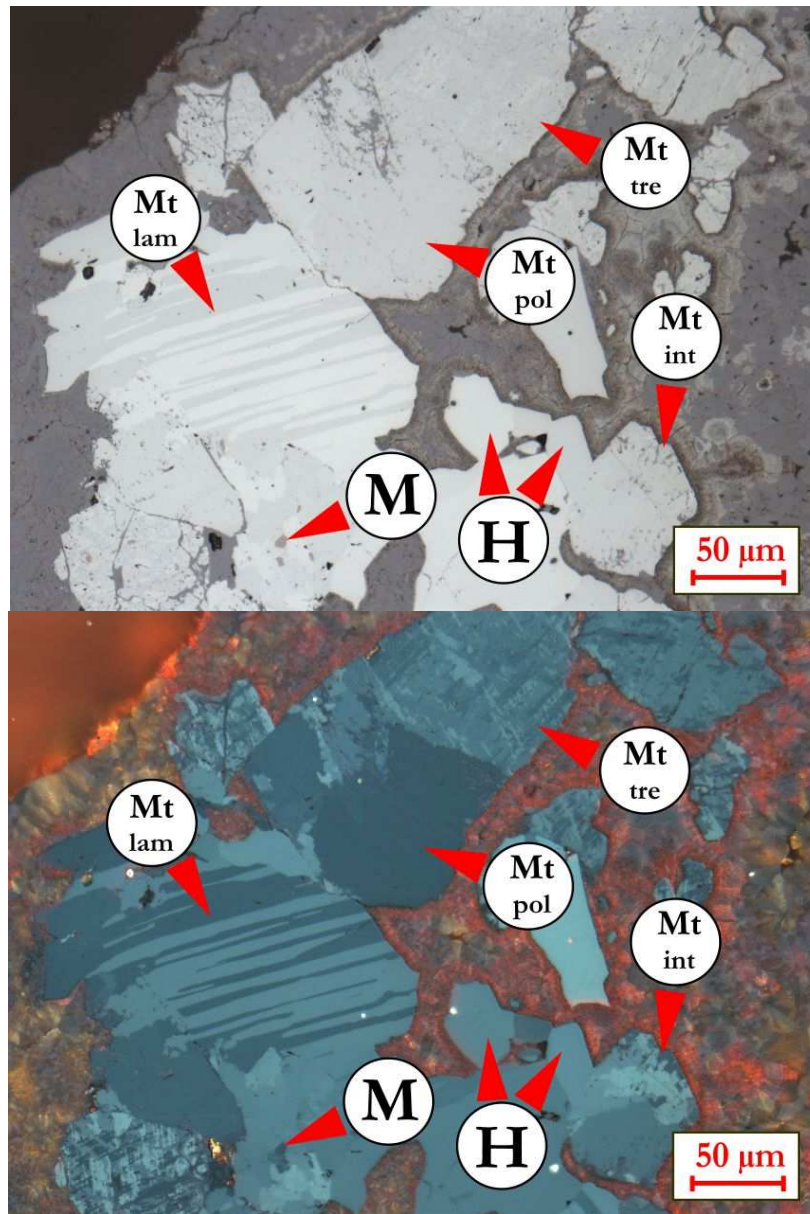
Figure 8: Various types of martite, lam = lamellae, pol = polygonal, int = interlobate, tre = trellis.

Magnetite is brown-grey in reflected light. The reflectance depends to a certain extent on the impurities and is lower than of for hematite. Mn, Mg, Ca, Ti and Al are the most common traces within the inverse spinel structure. Intracrystalline pores are rarely found. Magnetite is not stable under atmospheric condition, so it is oxidized to hematite.
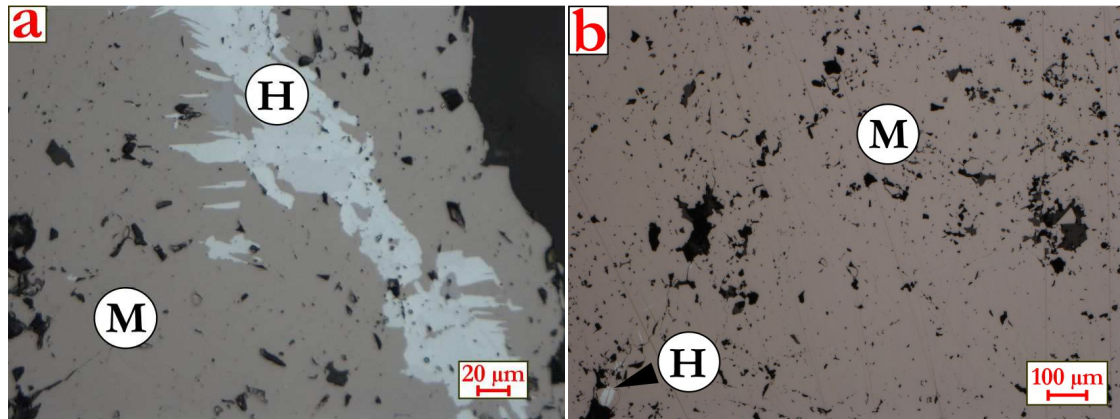
Figure 9: a) Magnetite (M) with hematite (H); b) magnetite ore; both from Kiruna-type deposit.

Limonite is a mixture of goethite and lepidocrocite (cryptocrystalline hydroxides of iron). In reflected light the color is dark grey with a bluish tint. The reflectance is lower than of hematite and magnetite. Internal red to brown reflections are common. It is a typical weathering product of iron-bearing minerals at the deposit surface outcrops and the quantity decreases with depth. Limonite is often intergrown with other iron oxides. Its shape varies from oolithic, crusty, shelly to earthy and porous masses. Pseudomorphs after hematite, magnetite, and siderite are possible.
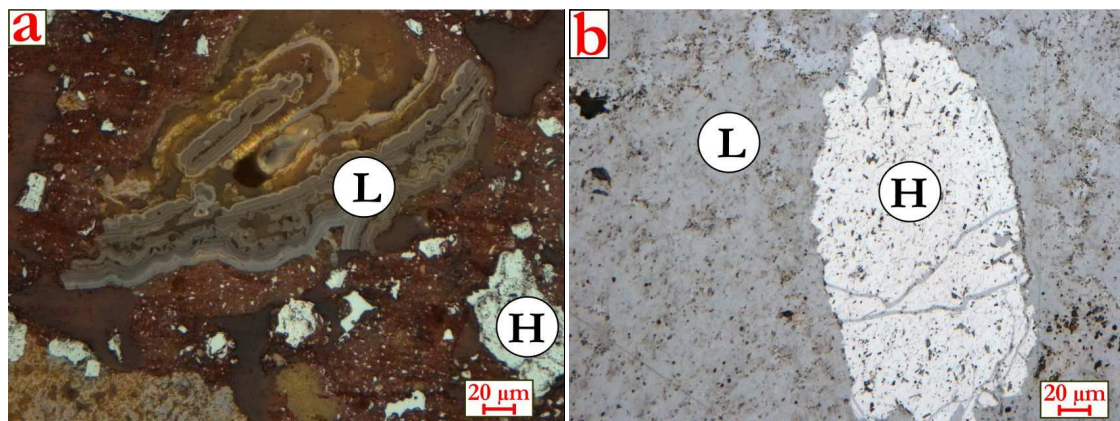
Figure 10: a) Shelled limonite (dark grey, centre); b) porous limonite (dark grey) and hematite (light grey).

3.2. Lump iron ore

Iron ore deposits

Iron is one of the driving forces in human culture development. Banded iron formation (BIF) hosted iron deposits are the most important source for iron worldwide, concerning reserves and production. Together with Kiruna-type and skarn deposits they are the main supplier for the iron and steel industry. BIF is a finely laminated to thinly bedded chert layers bearing chemical sedimentary rock, containing anomalous high iron content (James 1954, Beukes and Gutzmer, 2008).

It is widely accepted that BIF-hosted iron deposits are classified after the geotectonic settings and time of main depositing events:

- Archean and Paleoproterozoic *Algoma type* BIF hosted in granite-greenstone belts

- Proterozoic *Lake Superior type* BIF hosted in basins with passive margins

- Neoproterozoic *Rapitan type* BIF hosted mostly in glaciogenic marine sedimentary environment.

The detailed formation processes of the protolith of such huge accumulations of iron are still unknown. However, it is generally accepted that the origin of Fe is predominantly hydrothermal and the anoxic nature of the seawater before the Great Oxidation Event (around 2.4 Ga) is responsible for the higher content of dissolved Fe and Si in the water (Bekker et al 2010). This aspect is supported by the fact that the Rapitan BIF type is related to glaciogenic marine conditions, in which metals are dissolved in anoxic water zones during Snowball Earth events (Hoffman et al. 1998).

The genesis and upgrading processes of BIF hosted iron deposits are still under debate. Hagemann et al (2016) carried out a mineral system analyses on this iron ore deposit type. They focused on the geotectonic controls, the fluid pathways, depositional site including structural framework, mineralogy, fluid characteristics etc., as well as the upgrading processes and supergene modifications of the major BIF-hosted iron ore districts. Like in the petroleum system concept, various processes have to interact in a certain way to build up such dimensions. A mineral system approach includes 'all geological factors that control the generation and preservation of mineral deposit and stress the processes that are involved in mobilizing ore components from a source, transporting and accumulating them in a more concentrated form and then preserving them throughout the subsequent geological history' (Wyborn et al (1994).

The results of the Hagemann et al (2016) mineral system analysis are four end member models of hypogene and supergene BIF-hosted iron ore deposits:

- the granite-greenstone belt hosted, mainly strike-slip fault zone dominated *Carajàs-type*, where magmatic and/or metamorphic iron containing fluids interact with ancient warm meteoric water in the upgrading process.

- the sedimentary basin, mainly normal fault zone controlled *Hamersley-type*, where basinal and/or evaporitic Fe-brines struck on ancient warm meteoric water in the upgrading process. A subtype of this model is of a metamorphosed, deformed and upgraded basin during orogenic events.

- the sedimentary graben structure dominated basin of the *Urucum-type*, where glaciomarine BIF's are transformed during diageneses and/or low-grade metamorphosis by gangue leaching and hematite mineralization.

- the supergene *Capanema-type* is defined as a goethitic iron ore deposit with no relation to a hypogene source of the BIF.

These three hypogene dominated models do not exclude a supergene stage of enrichment during weathering. In fact, all BIF hosted iron ore deposits underwent supergene processes like oxidation, leaching and precipitation of iron oxides sometimes in past. Favorable climatic and geomorphological conditions support lateritic weathering, which reached depths of up to 200m (Ramanaidou and Morris 2013). This process formed friable to powdery ores, consisting mainly of goethite and hematite. Another supergene enrichment model is postulated by Ramanaidou and Morris (2013) based on the electrochemical model of Morris et al. (1980). In this model the upgrading of the BIF occurs in greater depths due to hydrodynamic groundwater flow systems, which can drive large electrochemical cells (Ramanaidou and Morris 2013). More detailed information and references are given in Hagemann et al. (2016).

Kiruna-type deposits are also described as iron oxide apatite ore deposits. The host rocks are metavolcanic rocks (lava and pyroclastic rocks), where magmatic-hydrothermal fluids intruded (Westhues et al. 2016). The detailed genesis of this type of deposit is still under debate. Magnetite is the dominant iron oxide mineral. The hematite and apatite content vary among the different deposits. The deposit of Kiruna in Sweden is the most important iron ore producer in Europe.

Skarn deposits are formed in the contact zone, where magmatic intrusions penetrate carbonates. The ore consists of massive magnetite layers or lenses. The can occur as irregular stockwork mineralization. One of the economically important skarn iron deposit is Gora Magnitnaja in the Ural Mountains. The ore grade varies from 35- 50 wt.% Fe and magnetite is the main ore mineral (Meinert 1992).

In Austria, the hydrothermal metasomatic massive siderite deposit Erzberg is of local importance. The iron grade (up to 40 wt.%) is low compared to supergene enriched BIF ores. The orebodies are irregular stocks or stratiform lenses. The genesis of the ore deposit is still under debate. A summary of the various genetic models is given in Prochaska (2016). The ore mineralization consists of siderite to sideroplesite and ankerite. The total production of the Erzberg deposit is used in sinter plants of Donawitz and Linz.

Iron ore textures

The textural classification of lump ore is used worldwide to categorize the genetic types and subtypes in an iron ore deposit. The Australian iron ore texture classification system for example is based on the dominant mineralogy, porosity and different replacement processes (Morris 1980, Clout 2003). It is adapted to the different Australian iron ore deposits. Clout (2003) linked some micro textural features to metallurgical lab testing indexes.

A more general classification describes the following characteristics and highlights the influence on the reducibility under standard reduction test conditions (Figure 11):

▪ type of iron oxide (limonite, hematite/ martite, magnetite)

▪ shape (xenomorphic, hypidiomorphic, idiomorphic, irregular)

▪ size (small, medium, coarse) of a grain or crystal

▪ inner structure (dense, porous)

▪ overall porosity

The reducibility of the minerals decreases from limonite to hematite and finally to magnetite. Xenomorphic crystals are better reducible than hypidiomorphic or idiomorphic ones. In addition, small crystals are transformed faster than coarse ones. The martitization forms trellis structures and these lamellae generate a better contact surface for the reduction progress.

Decreasing Reducibility

1. Limonite
2. Fine grained hematite
3. Trellis textured martite
4. Martite with irregular hematite crystal borders
5. Very fine grained (<2 µm) magnetite
6. Medium sized hematite with irregular crystal borders
7. Martite, and medium grained hematite with hypidiomorphic to idiomorphic crystals
8. Coarse grained hematite
9. Fine, medium sized, and coarse magnetite

Figure 11: Decreasing reducibility due the different mineral characteristics after Kain-Bückner and Mali (June 2015).

The lump ore samples were classified after this scheme under the microscope and the main ore types are ranked according to their reducibility. Nine different commercially available

lump ores were provided by the industrial partners voestalpine and primetals. Eight of them are from BIF's all over the world and one is from a Kiruna-type deposit. The size of the grains is between 10-12.5 mm, which is the same fraction as used for the ISO-4695 test. In addition, nine different pellet brand samples were provided and two different sinter samples.

The detailed genesis and classification of the deposit type is not essential for the determination of the reducibility properties. Nevertheless, a detailed petrographic analysis according the characteristics mentioned before can give more information regarding the reduction behavior than the results of a standard reduction test. The main criteria and key factors for the reducibility performance are the type of iron oxide (Figure 11), morphological characteristics (shape, size, etc.) and the intracrystalline and overall porosity. A certain amount of limonite or martite and a medium to high porosity (overall and intracrystalline) is considered to enhance the reducibility. However, magnetite and coarse dense hematite are going to have a negative impact on the reducibility. The type and size of the mineral are valued stronger than the overall porosity, beside very dense iron ores. The crystal sizes are defined as small (<10 μm), medium (10-20 μm) and coarse (>20 μm). Limonite and hematite are going to develop a secondary porosity during the reduction process. Limonite dewaters and at the reduction of hematite to magnetite a volume change occurs (Cornell and Schwertmann 2003).

Sample description

The industrial partners provided the samples, which are reference samples from different iron ore supplies within the last 20 years. The deposits are referenced in Table 2. The bulk samples were sieved and the grain size between 10 and 12.5 mm was used for the polished sections. The samples do not represent the entire ore deposit as systematically taken geological samples do, but they are suitable to evaluate the reducibility performance. This performance can be described and evaluated by a mineralogical and petrographical analysis of the ore types observed in the polished sections. The quantitative modal mineralogy of the ore types of the samples is determined by grain counting. Table 3 and Table 4 summarize the reducibility performance and the quantitative occurrence of the key factors. The link to the evaluation by the image processing software VisuMet is described in chapter 5.

Table 2: Overview of the samples, their origin and references to the geological description of the deposit or province.

Sample	Name	Country	Province	Deposit	Model	References
SA	San Isidro	Venezuela	Cuadrilatero Ferrifero de San Isidro	San Isidro	BIF Carajás-type	Ferenčić 1969
CL	Costra Limonitica	Venezuela	Cuadrilatero Ferrifero de San Isidro	San Isidro	BIF Carajás-type	Ferenčić 1969
MT	Mt Newman	Australia	Hamersley Province	Mount Whaleback	BIF Hamersley-type	Angerer et al. 2015, Hagemann et al. 2016
NA	Nagarjuna	**India	unknown	unknown	*BIF	
CI	China	China	unknown	unknown	*BIF	
HA	Hainan	China	Hainan Province	unknown	*BIF	Xu et al. 2013
AC	Acindar	Brazil	Urucum Basin	Corumba	BIF Urucum-type	Urban et al. 1992, Angerer et al. 2016
SI	Sishen	South Africa	Transvaal Supergroup	unknown	BIF Capanema-type	Carney and Mienie 2013, Beukes et al. 2013
KI	Kiruna	Sweden	Kiruna-Malmberget Province	Kiruna	Apatite-iron oxide "Kiruna"	Jonsson et al. 2013, Westhues et al. 2016

**suspected due to name

*based on mineralogy of the sample

San Isidro (SA)

The bulk sample SA is from a district of the iron metallogenetic province of "Cuadrilatero Ferrifero de San Isidro" in Venezuela. The iron ore deposit is called San Isidro. The deposit is enclosed by metamorphosed sedimentary and igneous rocks of Early Precambrian age in the Imataca greenstone belt (Ferenčić 1969). It is classified as BIF-hosted iron mineral system of the Carajas-type after Hagemann et al. (2016). The supergene enrichment is controlled by strike-slip faults and leaching of quartz (Ferenčić 1969).

The sample material consists of various grains from three different ore types. The main ore type 1 (50 vol.%) consists of hypidiomorphic coarse martite and limonite (Figure 12). Relictic magnetite occurs subordinate in these martites. The former magnetite is often leached (voids, Figure 12) and partly replaced by limonite. This leaves behind a porous inner structure.
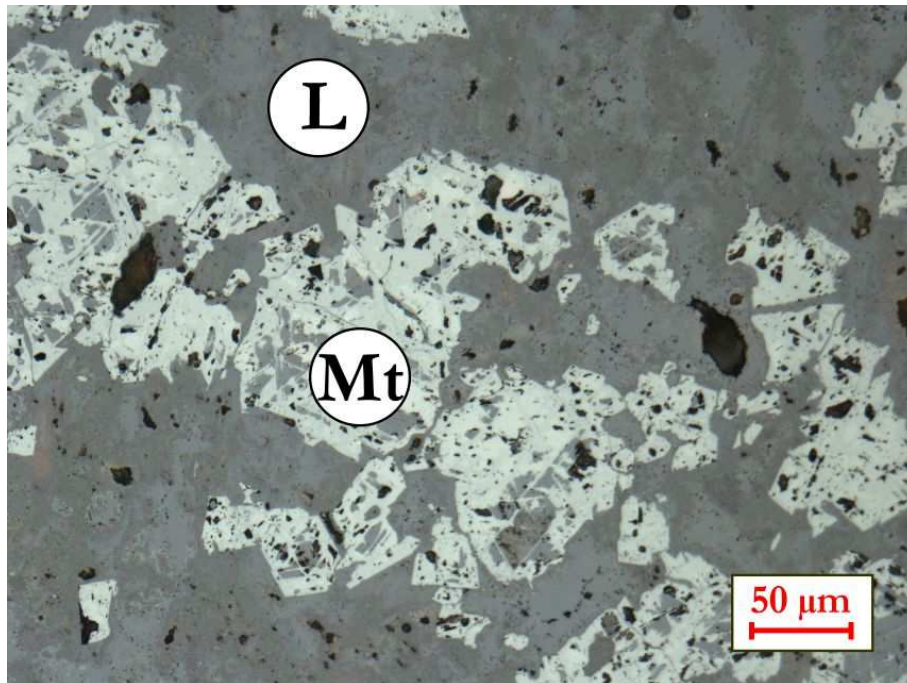
Figure 12: Coarse martite with limonite cores in a porous and in parts dense limonite matrix.

Ore type 2 (35 vol.%) forms xenomorphic to hypidiomorphic coarse hematite crystals enclosed in limonitic finely crystallized mass and seams (Figure 13). The crystals are dense. In addition, secondary microplaty hematite is found in the leached parts as filling beside the limonitic seam. The limonite occurs either as spongy mass, alteration seam, and idiomorphic coarse crystals. Coarse quartz grains are present in one sample grain, but most of gangue material is leached or replaced.
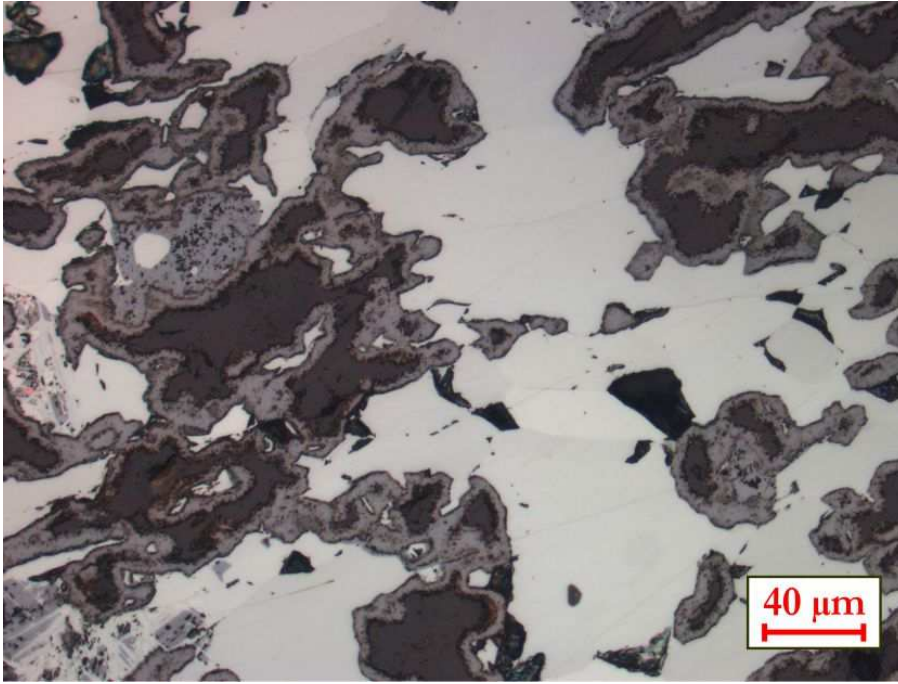
Figure 13: Dense coarse xenomorphic hematite surrounded by two generations of limonite.

Ore type 3 (15 vol.%) consists of coarse martites. The former magnetite cores are transformed to limonite (Figure 14). Xenomorphic coarse hematite occurs subordinately. The matrix is an assemblage of finely crystallized limonite and lepidocrocite. A secondary microplaty hematite generation was observed.
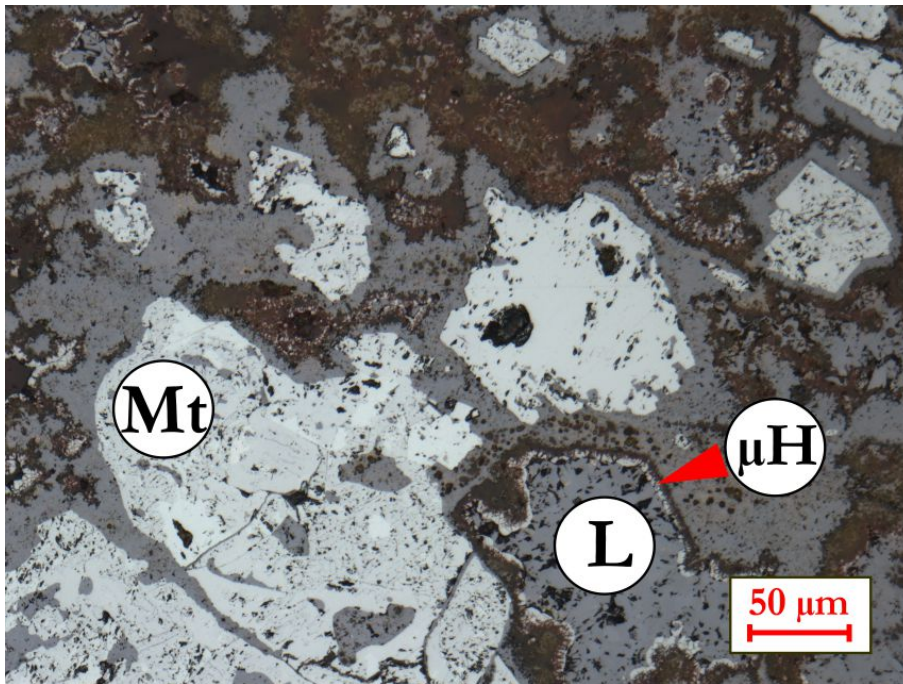
Figure 14: Coarse martite and hematite in limonite matrix. Microplaty hematite occurs as rims around lepidocrocite.

Costra Limonitica (CL)

The term "costra limonitica" is used for a particular ore formation within the San Isidro deposit. The sample is characterized by three ore types. Type 1 consists of coarse dense hypidiomorphic to xenomorphic hematite/martite (Figure 15). The hematite is surrounded by a limonitic seam. A secondary microplaty hematite grew on the limonite seam. Ore type 1 makes up to thirty percent of the sample.
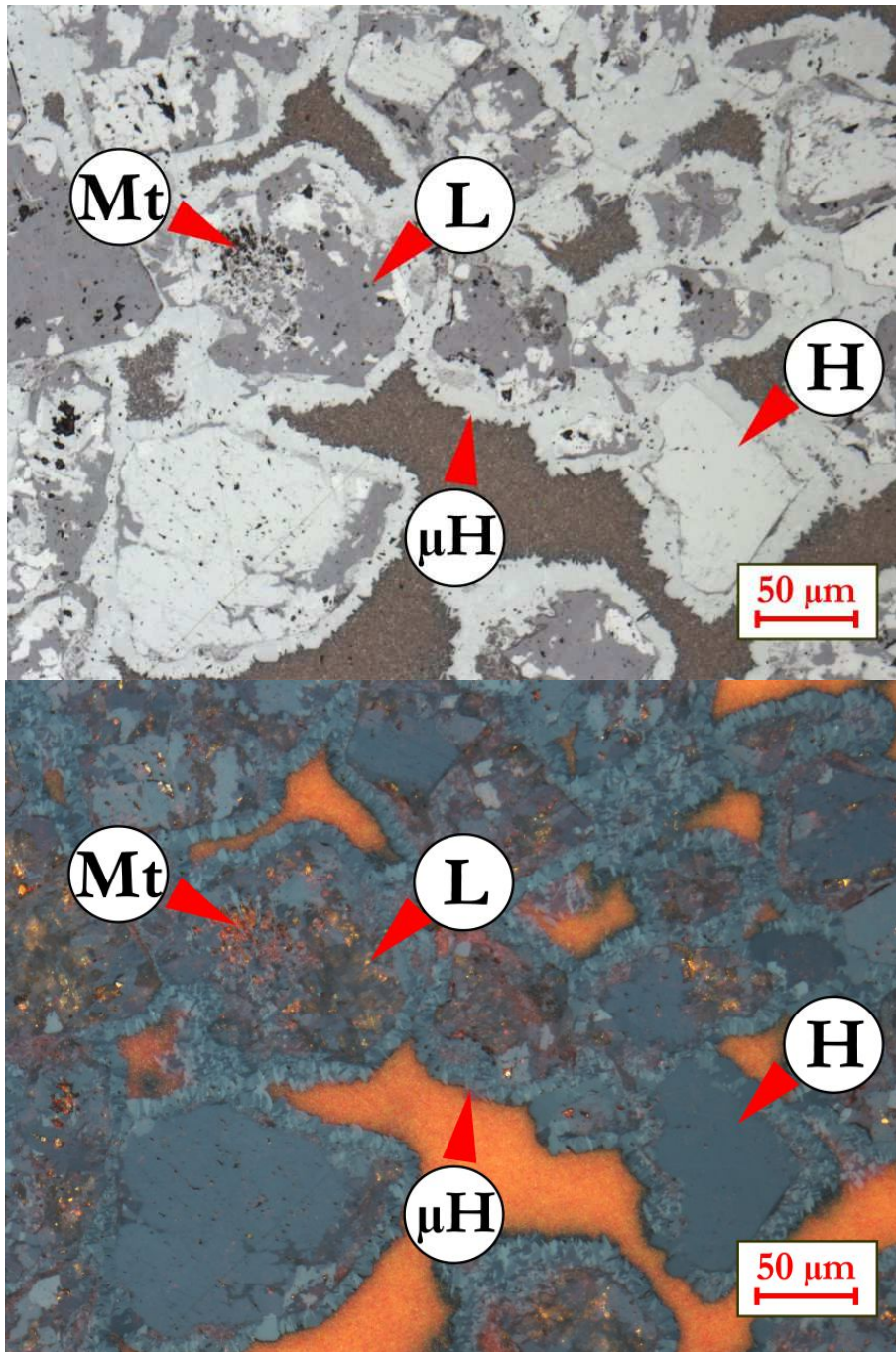
Figure 15: Hypidiomorphic coarse hematite surrounded by limonite and secondary microplaty hematite.

Ore type 2 is mainly hypidiomorphic to xenomorphic, coarse, porous martite/hematite in a limonite matrix (Figure 16). The former magnetite cores are transformed to limonite, too. The limonite matrix is finely crystalline, partly a dark and dense lepidocrocite occurs within the matrix. Subordinated, round quartz grains are still present, but most of them are leached, leaving voids. About 60 % of the sample is ore type 2.
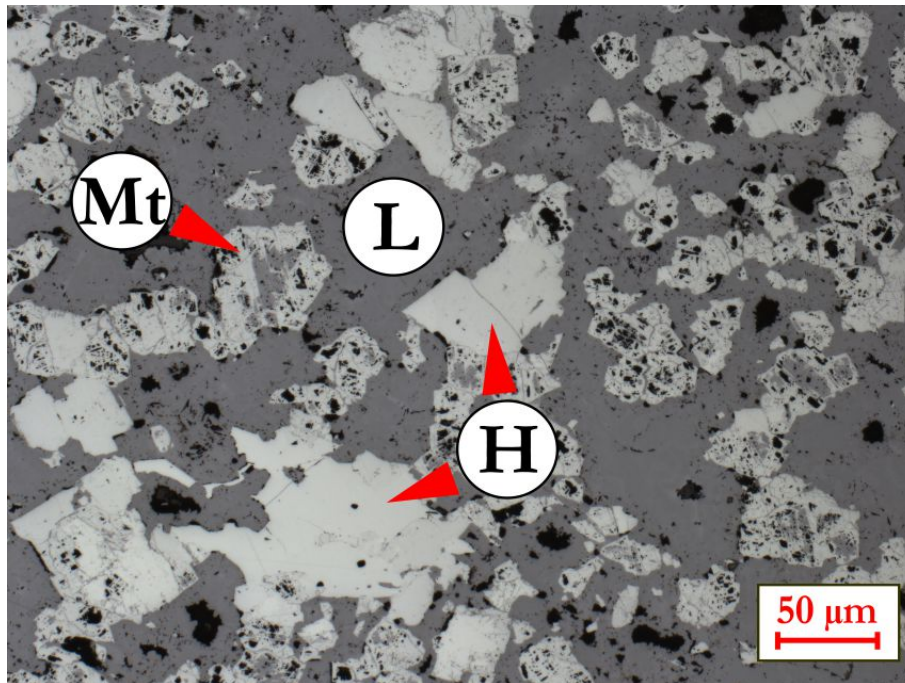
Figure 16: Coarse martite and hematite crystals in limonite matrix.

Ore type 3 (10 %) has coarse xenomorphic dense hematite surrounded by a slightly darker secondary hematite matrix (Figure 17). Limonite as void filling occurs here and there.
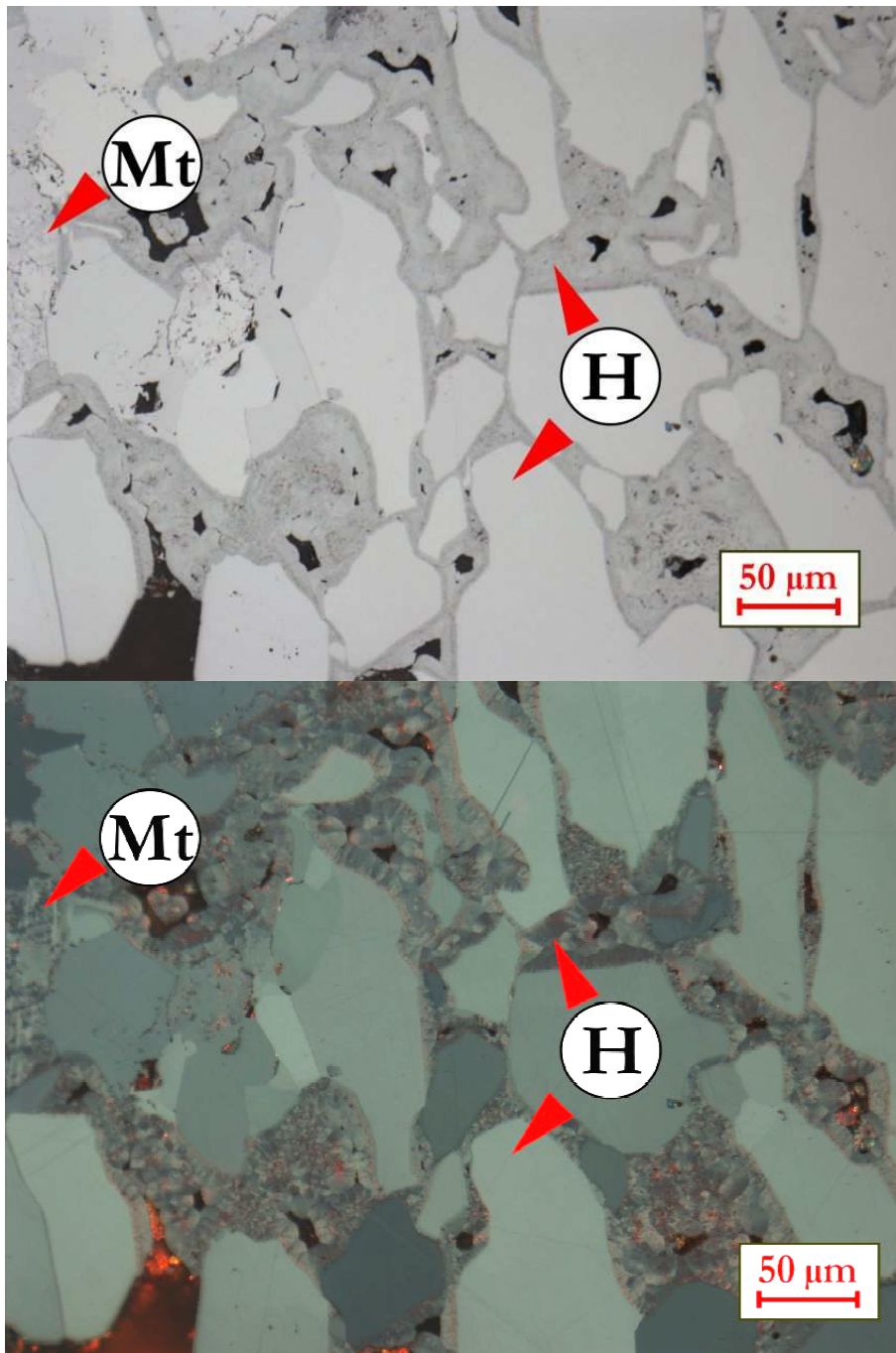
Figure 17: Coarse, xenomorphic, dense hematite and martite in a secondary hematite matrix.

Nagarjuna (NA)

The location of the iron ore deposit of the sample 'Nagarjuna' is unknown. The name suggests an Indian origin.

Ore type 1 (60 vol.%) is characterized by hypidiomorphic to xenomorphic trellis martite (Figure 18). The former magnetite cores are leached. A second generation of hematite grew around the coarse martites. Subordinately, magnetite cores are still visible. In addition, coarse dense medium to coarse xenomorphic hematite is present. The inner and overall porosity is high.
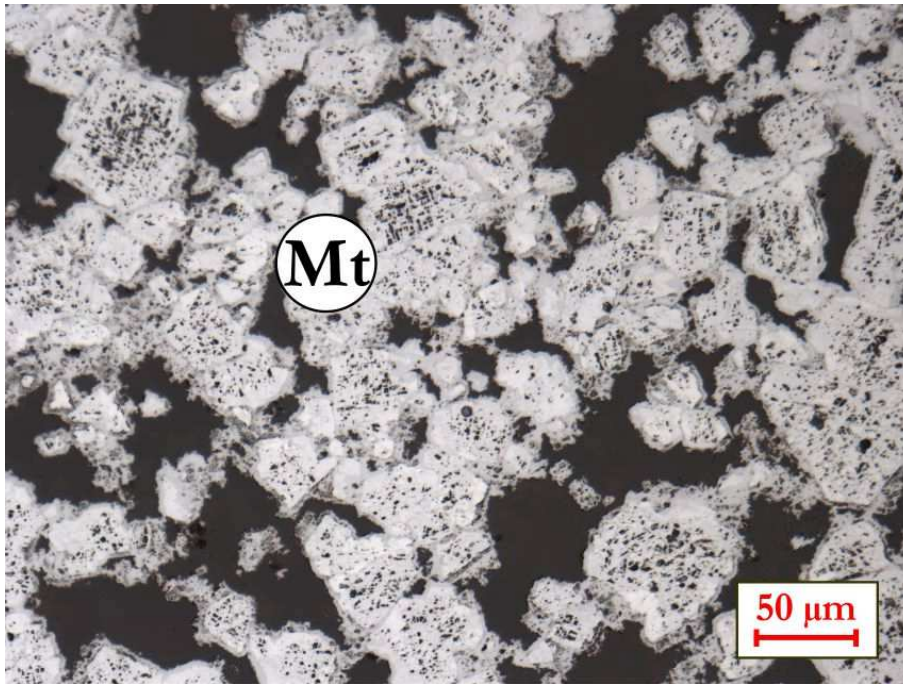
Figure 18: Hypidiomorphic to xenomorphic trellis martite.

Type 2 (27 vol.%) consists of coarse idiomorphic to hypidiomorphic martite (Figure 19). The former magnetite cores are partly leached. Parts of the martites are surrounded by a limonite matrix. The porosity is high, too.
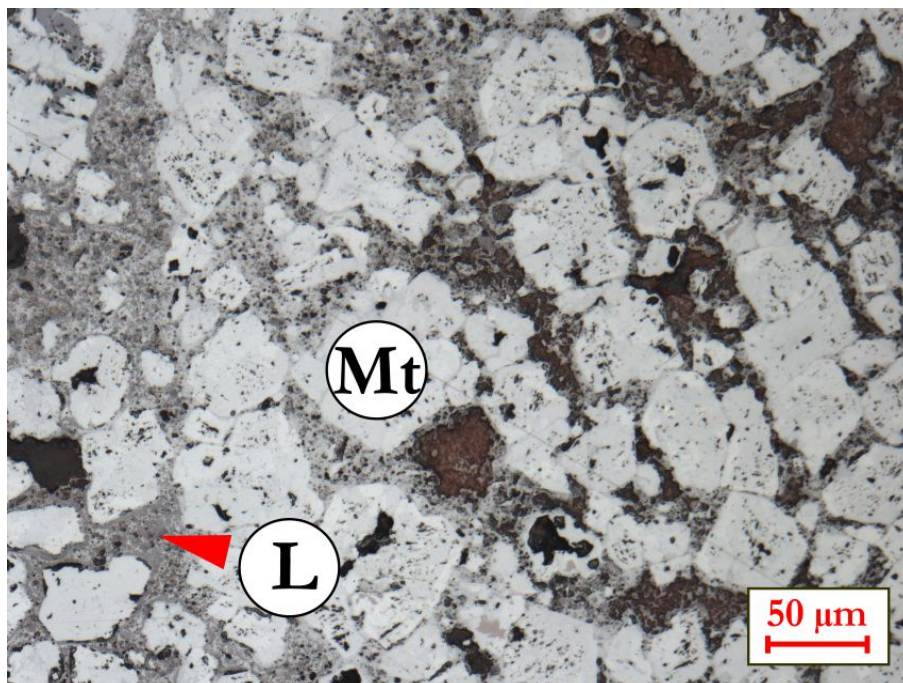
Figure 19: Coarse idiomorphic to hypidiomorphic martite surrounded by limonite matrix.

Ore type 3 (13 vol.%) is influenced by weathering. Former magnetite is leached, leaving only secondary rims of dense hematite (Figure 20). Porous coarse trellis martite is ob-

served. Partly, the former magnetite cores are transformed to limonite. Beside a cherty matrix, a finely crystalline mass of limonite is between the martite and hematite grains.
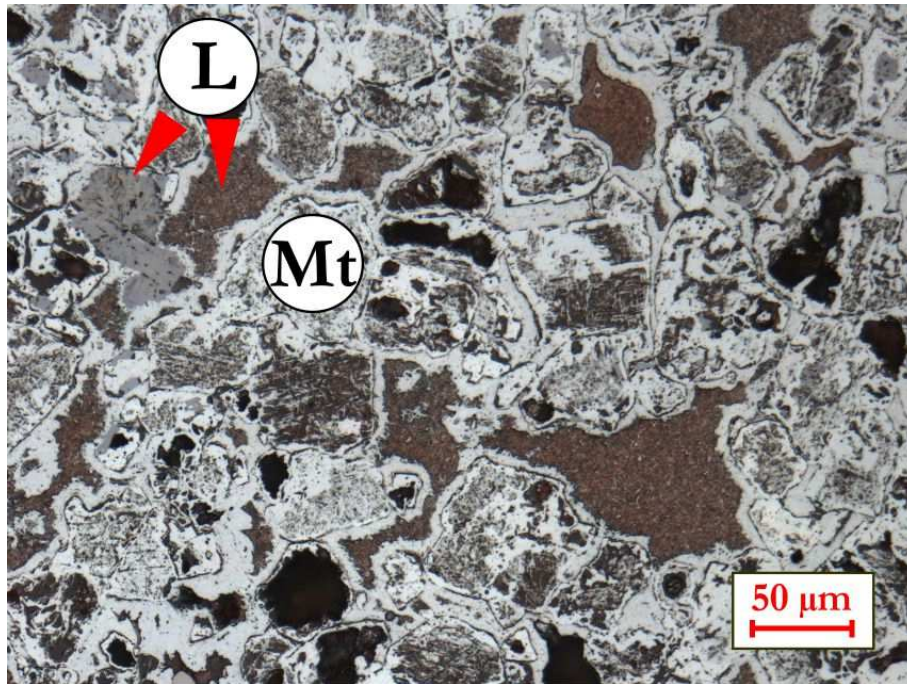
Figure 20: Xenomorphic trellis martite in a finely crystalline limonite.

Mount Newman (MT)

The sample 'Mount Newman' is from the Mount Whaleback orebody of the Hamersley Province in Western Australia. Stratigraphically, the sample is from the basal Marra Mamba iron formation of the Hamersley Group (Angerer et al. 2015). The structure of the deposit is dominated by several normal faults (Hagemann et al. 2016). Ore type 1 (50 vol.%) consists of dense xenomorphic coarse martite. Xenomorphic secondary hematite in various sizes occurs as younger generation in the gangue phase (quartz). Limonite is present as fracture filling (Figure 21).
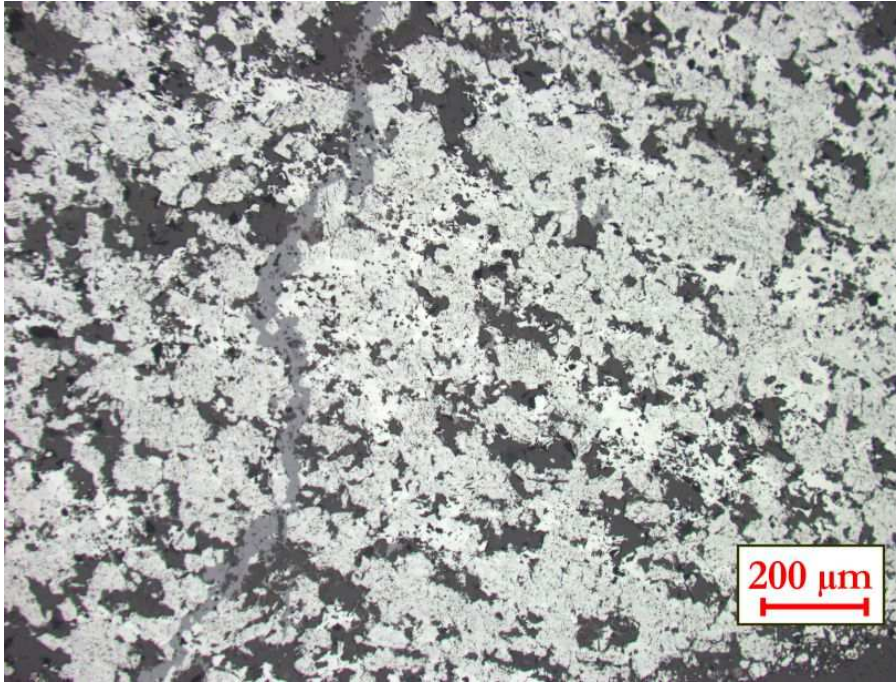
Figure 21: Xenomorphic coarse martite and limonite as void filling.

Ore type 2 (25 vol.%) are very coarse martite crystals surrounded by limonite and microplaty hematite (Figure 22). The matrix is formed by another younger limonite generation. The texture is breccia like. The former magnetite cores are leaching, leaving voids. Subordinately the voids are filled with limonite. The limonite occurs spongy and shelled. Coarse dense radial limonite crystals occur too.
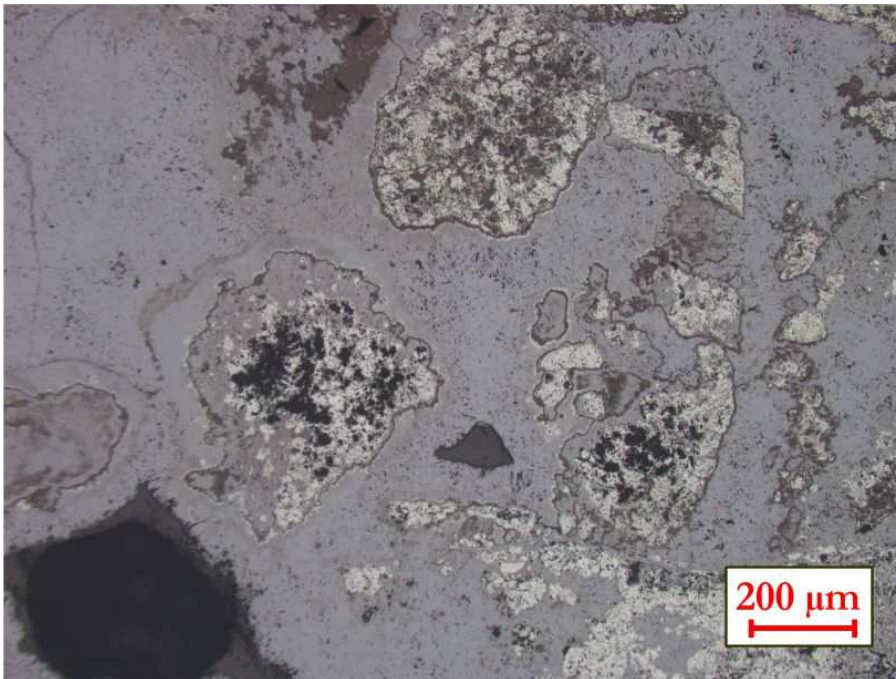
Figure 22: Coarse partly leached martite crystals in limonite matrix.

Ore type 3 (25 vol.%) are single hematite and martite crystals of various size in a chert matrix (Figure 23). Subordinately, fine crystalline limonite is present in the matrix.
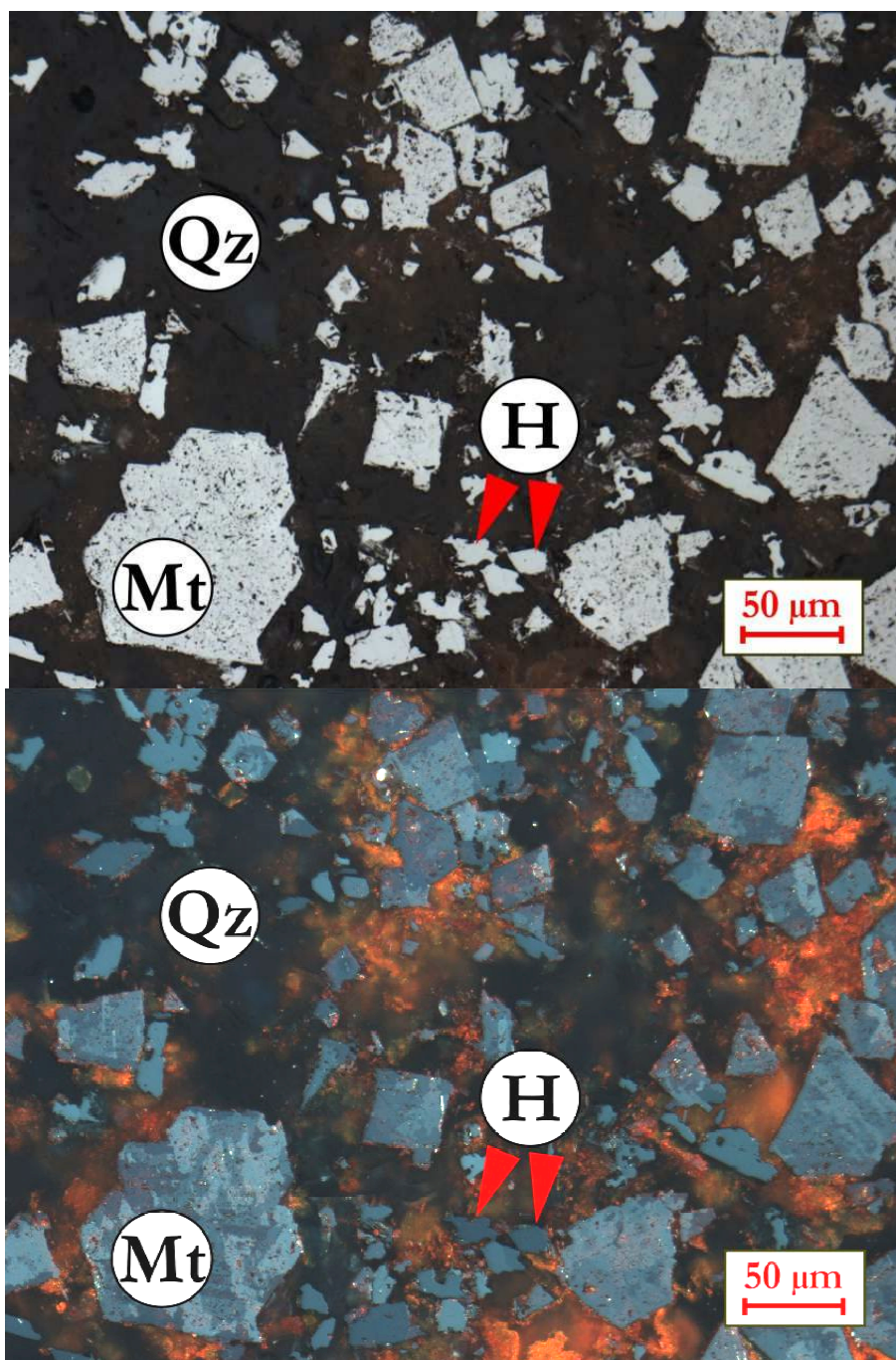
Figure 23: Single crystals of hematite and martite in a chert matrix.

Table 3: Ore type classification of the samples SA, CL, NA and MT according the reducibility potential in the grain fraction 10-12.5 mm.

Ore type	Hematite hypidiomorphic idiomorphic			Hematite xenomorphic			Martite dense porous			Magnetite dense		Hematite Martite	Limonite	Reducibility
	s	m	c	s	m	c	s	m	c	crys.	relict	tr, vf		
SA1						■ major			■ major				major	excellent
SA2						■ major						minor	minor	good
SA3			minor			minor			■ major			minor	major	excellent
CL1		minor				■ major							rare	good
CL2		minor	minor						■ major				major	excellent
CL3			sole		rare								rare	intermediate
NA1	minor					minor			■ major					good
NA2									■ major		rare		major	excellent
NA3					major				■ major		rare		minor	good
MT1		minor							■ major				minor	good
MT2				minor					■ major				major	excellent
MT3		major						major					minor	intermediate

Content (vol.%)		Reducibility	
sole >95%	■ (black)	excellent	■ (black)
major 20-95%	■ (dark gray)	good	■ (dark gray)
minor 19-1%	■ (gray)	intermediate	■ (gray)
rare <1%	■ (light gray)	bad	■ (light gray)

China (CI)

Sample CI is termed "China". The name of the deposit is unknown. Three ore types are identified. Ore type 1 is characterized by idiomorphic to hypidiomorphic medium to coarse hematite with intercalated quartz grains (up to 25 vol.%) (Figure 24). Coarse porous martite crystals, sometimes with relict small magnetite cores, are subordinately present. Secondary microplaty hematite is grown around the quartz grains.
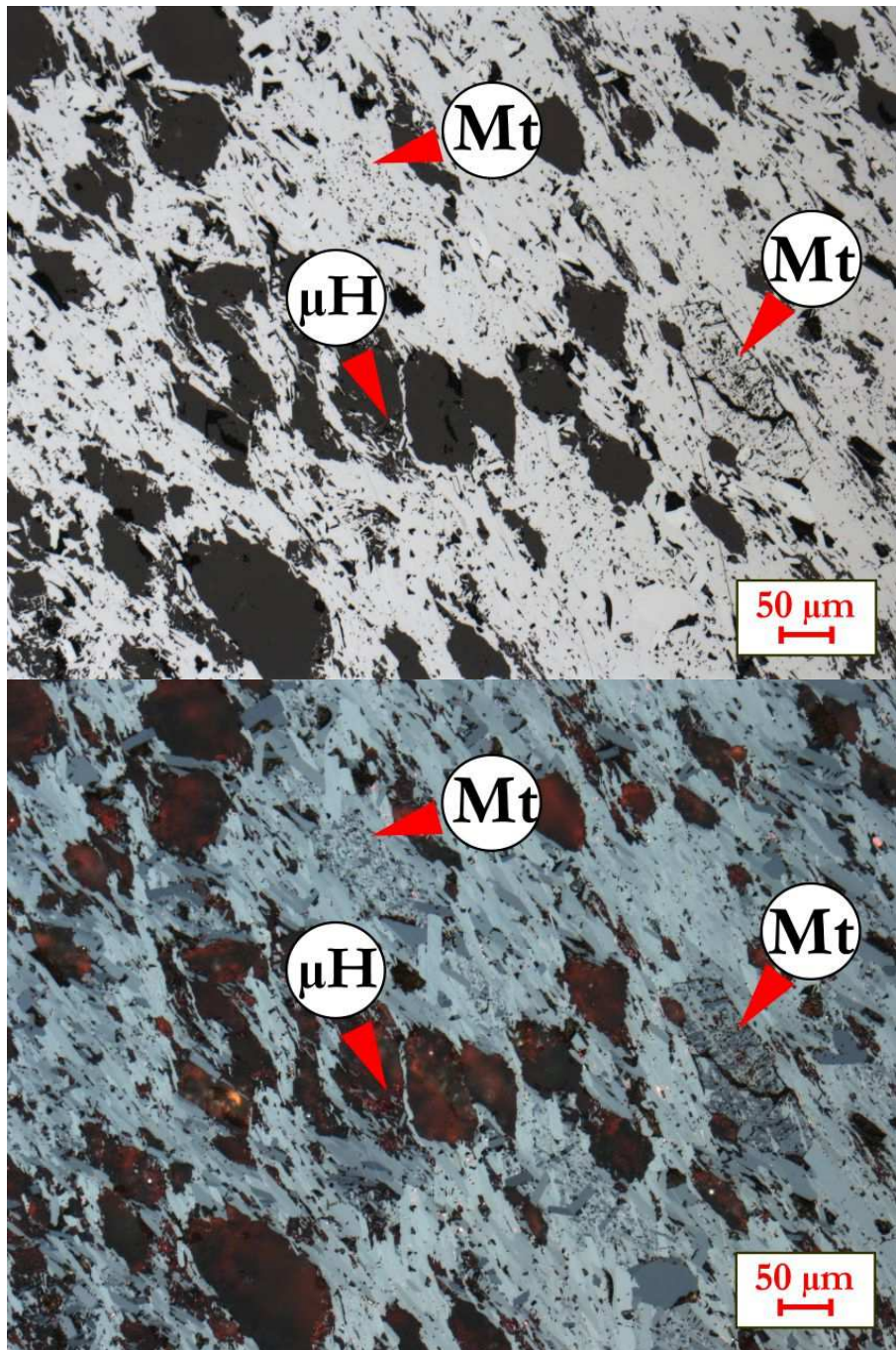
Figure 24: Ore type 1, martite crystal (Mt) with typical trellis structure; microplaty hematite occurs near to the rounded quartz grains (black).

Ore type 2 consists of hypidiomorphic coarse martite in quartz matrix (Figure 25). The inner structure of the martites is porous due to partial leaching. Individual secondary xenomorphic coarse hematite crystals are present subordinately, as well as secondary microplaty hematite.
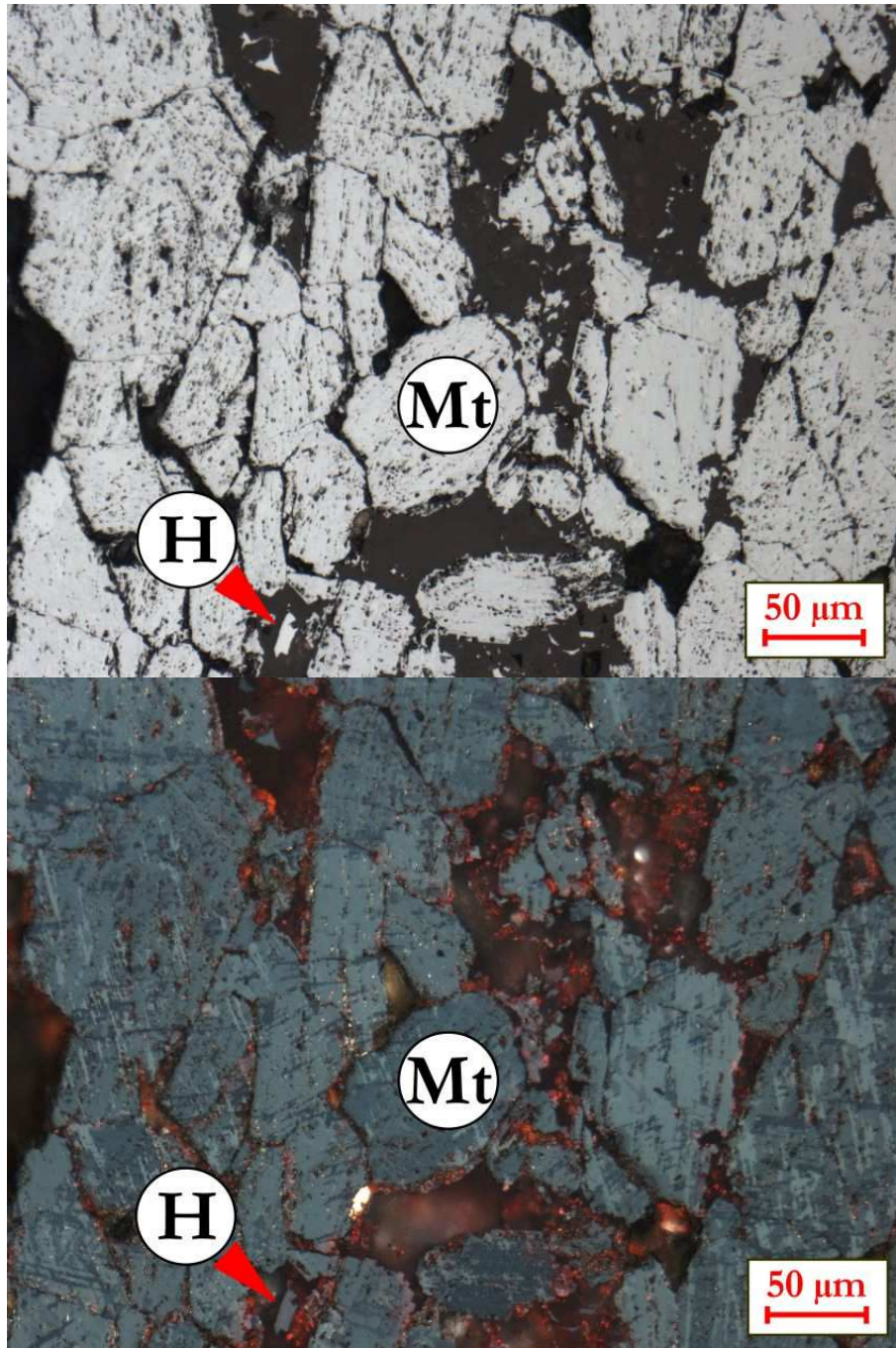
Figure 25: Ore type 2, trellis martite crystals in quartz matrix with secondary dense hematite.

Ore type 3 is dominated by xenomorphic to idiomorphic coarse hematite, which encloses coarse quartz grains (Figure 26). Voids are more abundant and larger than in ore type 1. Dense coarse martite crystals are part of the type, too (up to 25 vol.%). Subordinately porous martite, with relict magnetite cores, is partially distributed (less than 10 vol.%).
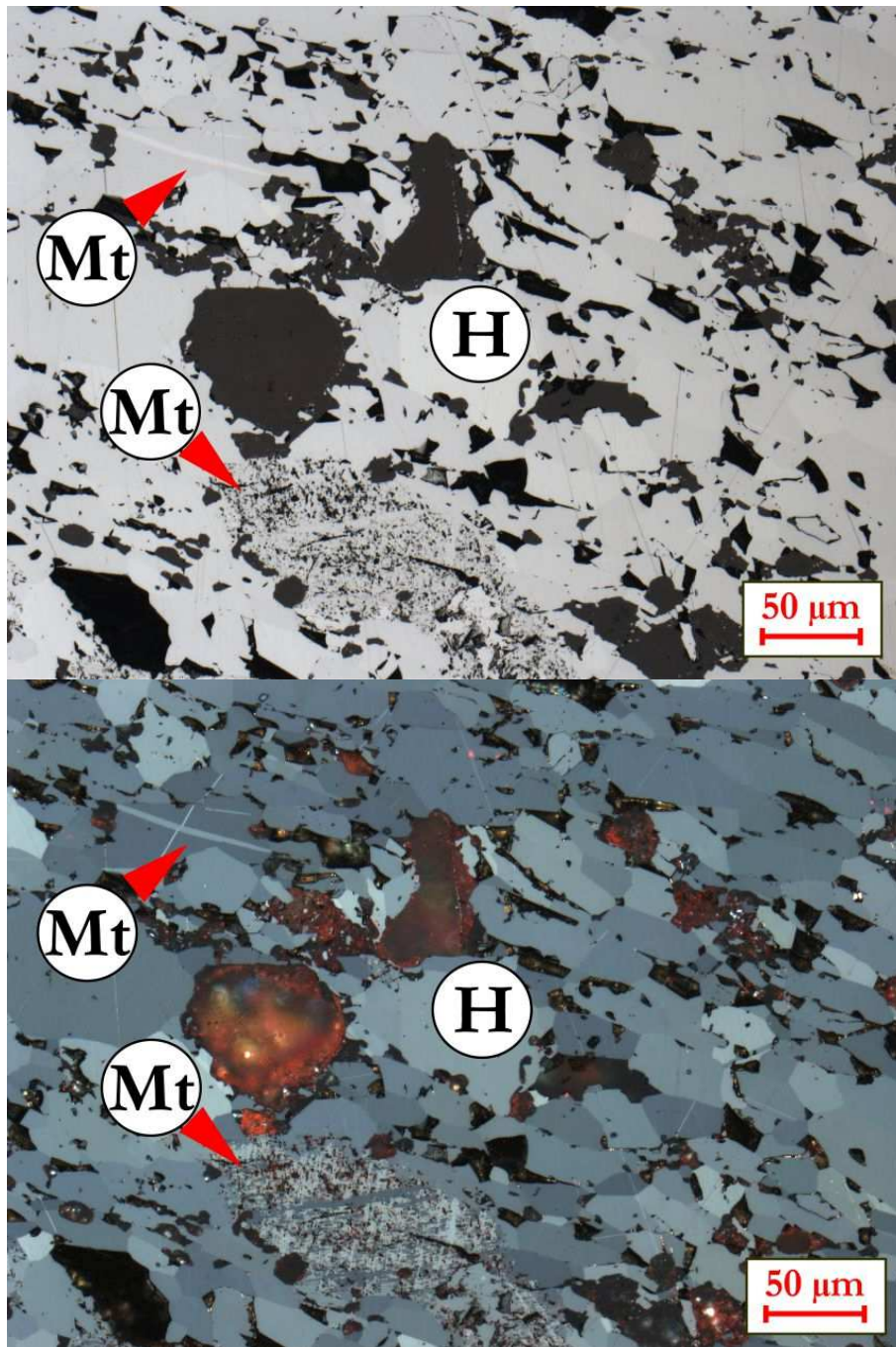
Figure 26: Ore type 3, dense coarse hematite and martite.

In the sample the content of ore type 1 is 44 vol.%, whereas ore type 2 makes up 38 vol.%. The amount of ore type 3 is 18 vol.%.

Hainan (HA)

The sample HA comprises four different ore types. The exact provenance is unknown. Due to the name it is supposed, that the sample came from an iron ore deposit from Hainan Island, in the South China Sea. Most of the ore grains are aligned parallel to foliation. The gangue content of to 50 vol.% is the highest of all investigated hematitic ores. The

gangue consists mainly of quartz crystals with a diameter of up to 0.5 mm. The quartz is partly elongated in foliation direction.

Ore type 1 (32 vol.%) consists mainly of xenomorphic, medium to coarse hematite. A second generation of hematite is present as idiomorphic, small to medium crystals. Subordinately, coarse magnetite crystals with beginning martitization are visible. The gangue consists of rounded quartz grains (Figure 27).
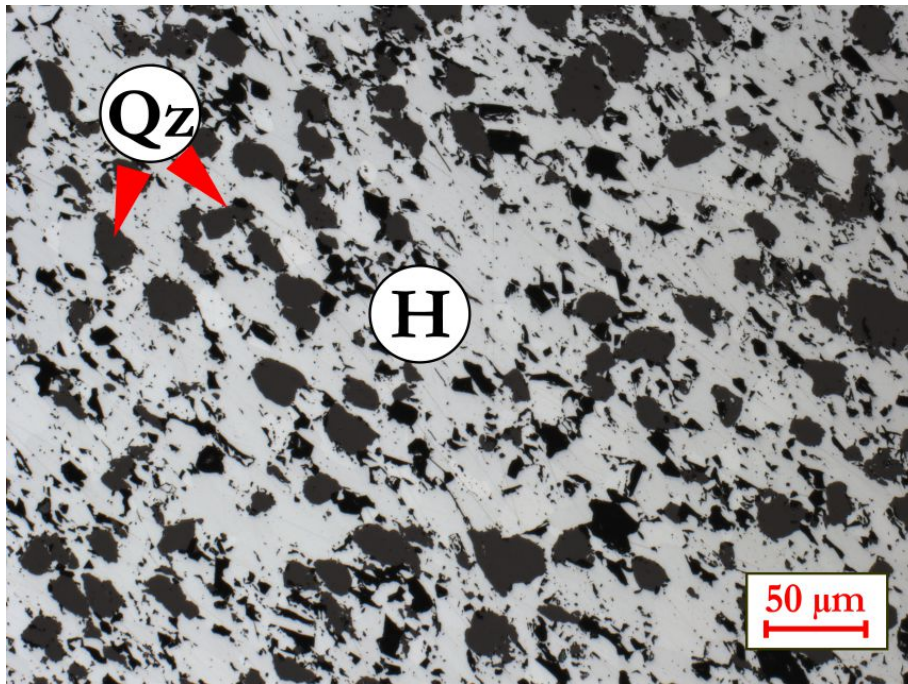
Figure 27: HA ore type 1 with xenomorphic hematite and rounded quartz grains.

Ore type 2 (14 vol.%) is characterized by idiomorphic to hypidiomorphic, medium to coarse hematite and secondary microplaty hematite (Figure 28). Quartz grains are the main gangue phase, subordinately pyrite and pyrrhotine occur.

The main ore phase in ore type 3 (36 vol.%) is idiomorphic, coarse to medium hematite and dense coarse martite (Figure 29). Rounded quartz grains are the main gangue phase. The hematite is foliated. Ore type 4 (18 vol.%) is denser and has less gangue and secondary microplaty hematite than the other types (Figure 30). It consists mainly of xenomorphic medium to small hematite.
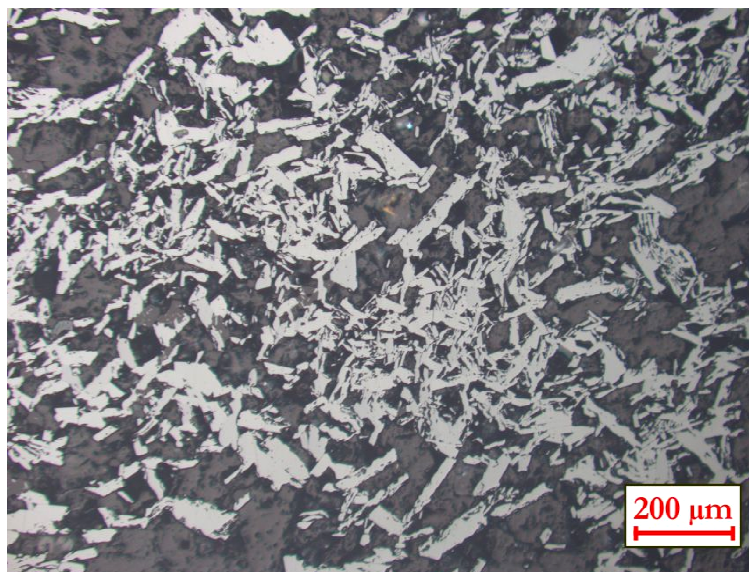
Figure 28: Idiomorphic coarse hematit (grey) and quartz (dark grey).
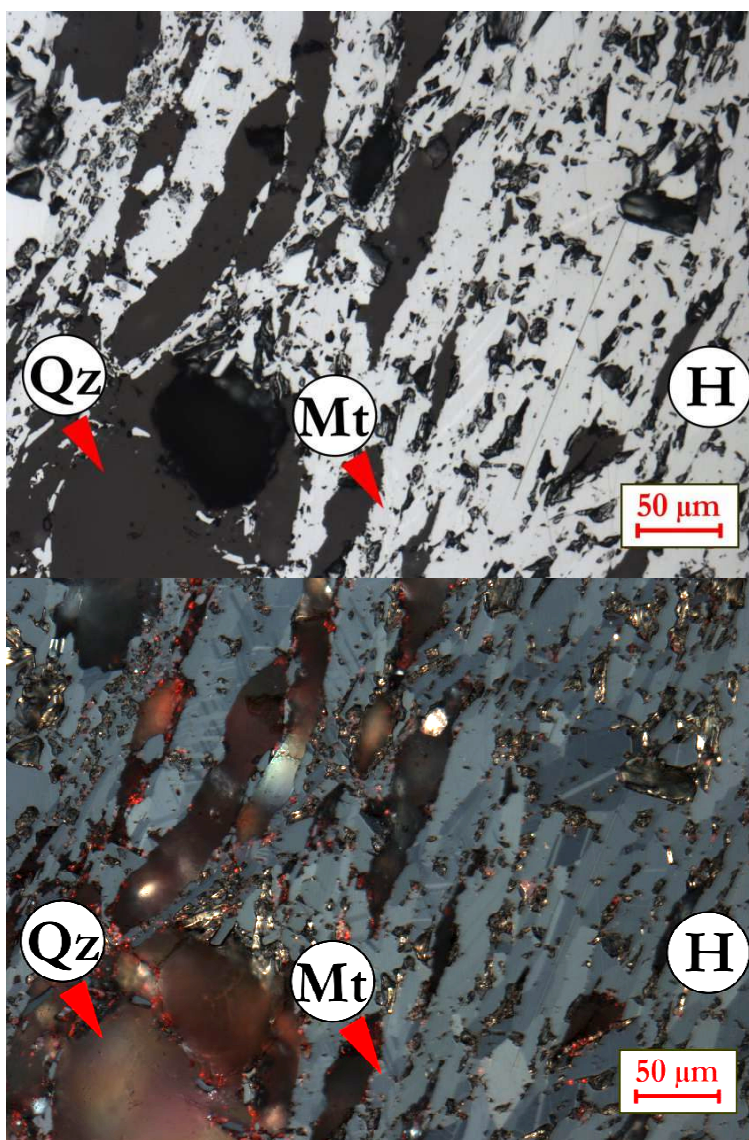
Figure 29: Foliated hematite and martite with round quartz grains.
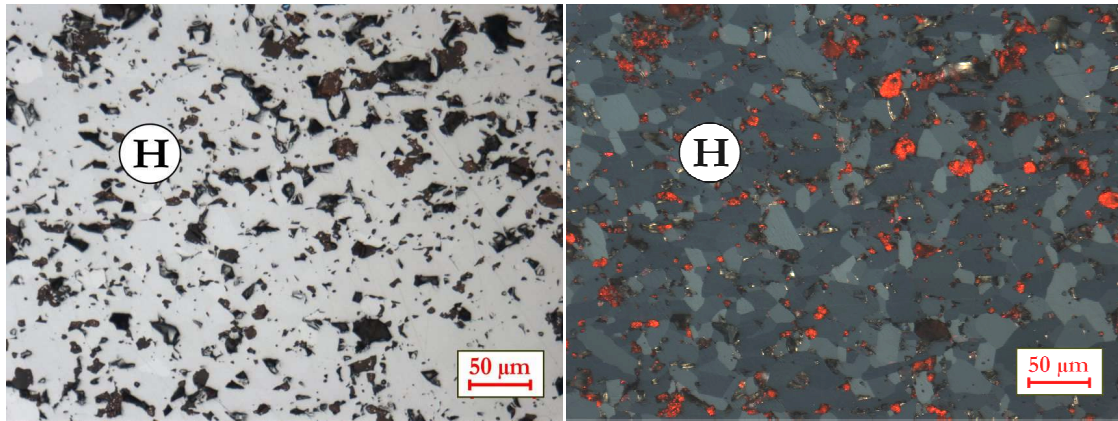
Figure 30: Xenomorphic medium to small hematite.

Sishen (SI)

The sample SI came from the mining area of Sishen in South Africa. The exact location of the deposit is unknown. Some ore grains are finely laminated. Two different ore types are found in the sample SI. Ore type 1 (75 vol.%) is characterized by xenomorphic, small to medium, dense hematite crystals (Figure 31). A second younger generation of hematite crystals (>100 μm) is present as fracture and voids filling.
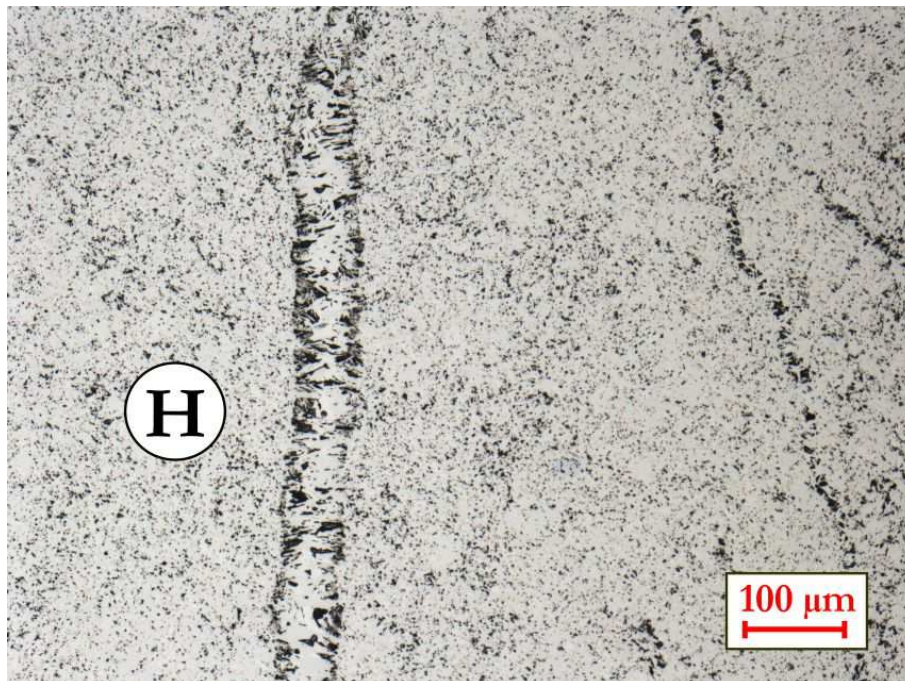
Figure 31: Xenomorphic small hematite. The void fillings consist of secondary medium sized hematite.

Ore type 2 (25 vol. %) consists of bands of xenomorphic, coarse hematite and small secondary idiomorphic hematite (Figure 32). The porosity is higher than in ore type 1.
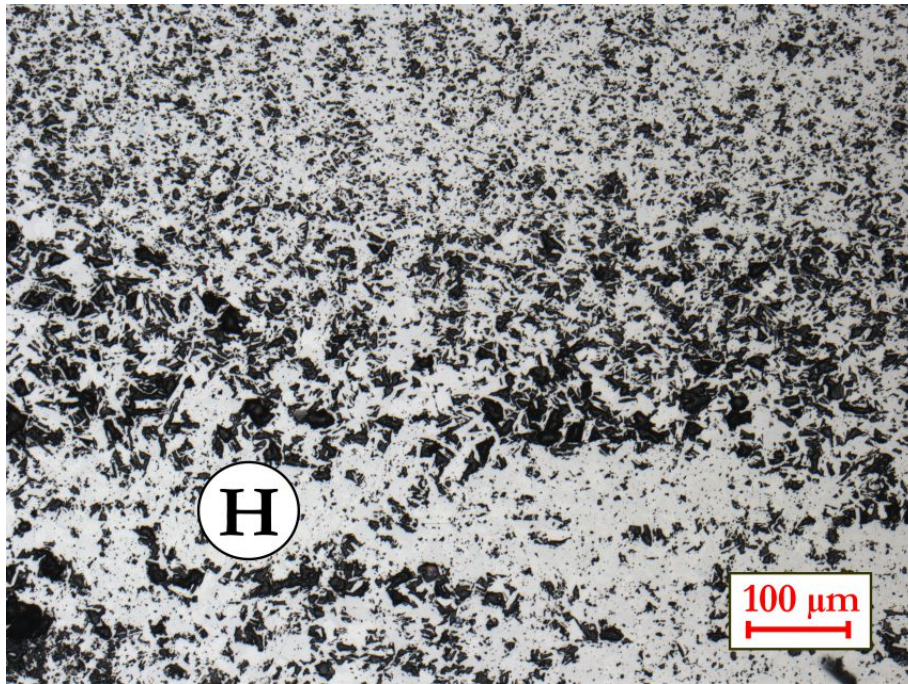
Figure 32: Xenomorphic coarse, laminated hematite and secondary small hematite.

Acindar (AC)

Two ore types are identified in sample AC, termed "Acindar". The deposit is called Corumba and is located in the Urucum Basin in Brazil. For detailed geological description see references in Table 2. It is classified as BIF-hosted iron mineral system of the Urucum-type after Hagemann et al. (2016). Ore type 1 (53 vol.%) consists mainly of xenomorphic, dense small to medium hematite (Figure 33). The texture is fine to medium laminated. A second generation of microplaty hematite is grown in the voids. The porosity is the highest compared to the other hematitic ores (HA, SI, CI).
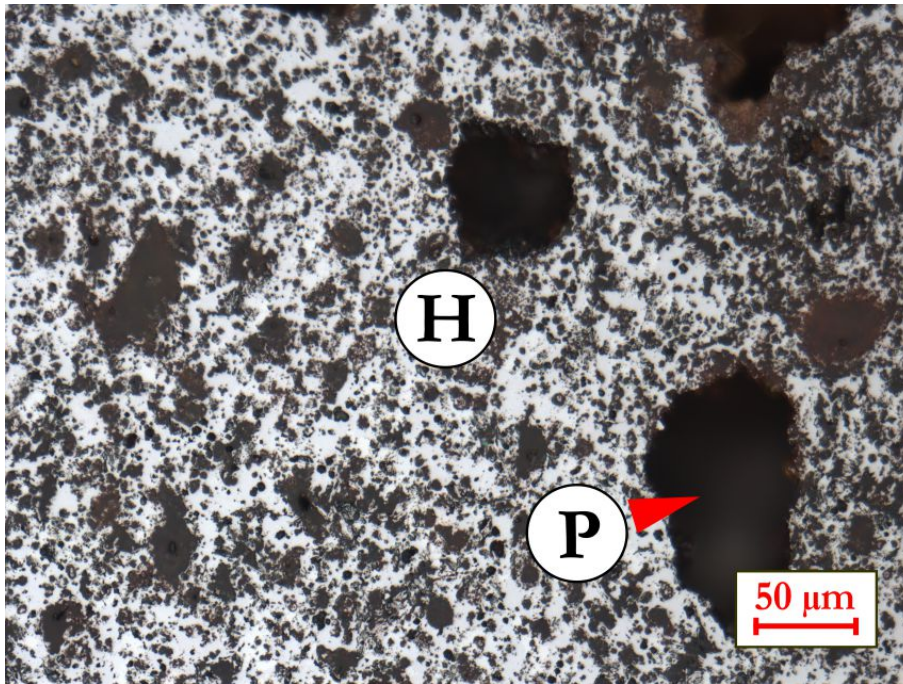
Figure 33: Xenomorphic small to medium hematite and quartz grains. The pores have a diameter up to 1mm.

Xenomorphic to idiomorphic small to very small hematite is the main ore phase in ore type 2 (47 vol.%) (Figure 34). A secondary coarse hematite generation is present in this type, too.
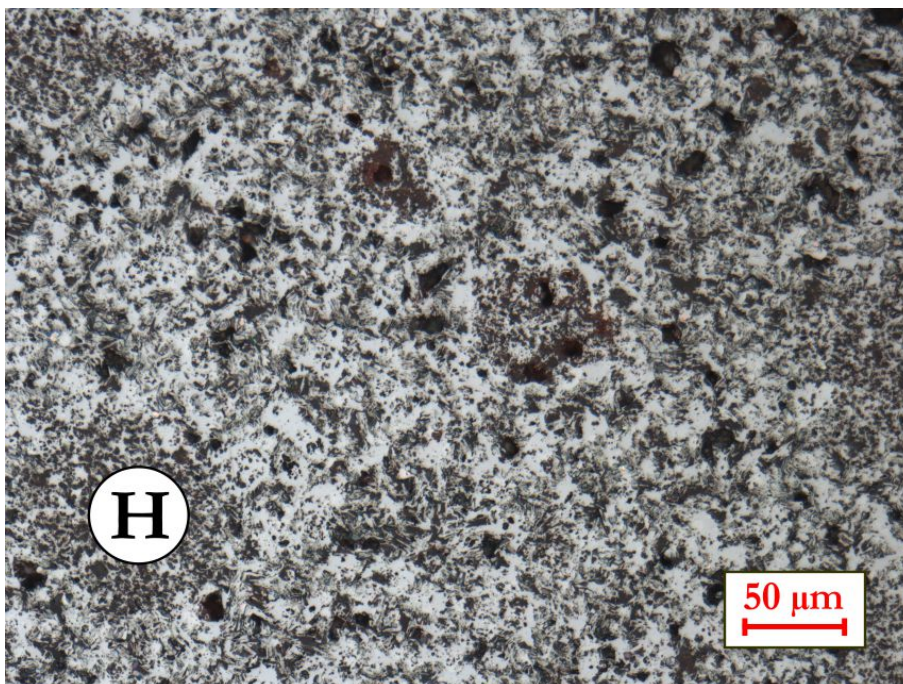
Figure 34: Xenomorphic small to very small hematite and quartz as gangue phase.

Kiruna (KI)

The sample KI is from the Kiruna iron ore deposit in Sweden. It is the only non- BIF deposit sample. Kiruna is the type area for iron oxide-apatite deposits. For more information see Table 2.

The main ore mineral is magnetite in various sizes and shapes (Figure 35). The crystal size (if visible) varies between 50 and > 100 µm. Ten to fifteen percent of gangue minerals are present in the ore grains. The gangue consists of quartz, titanite, apatite and sulfides. The hematite content is less than 5 vol. %.
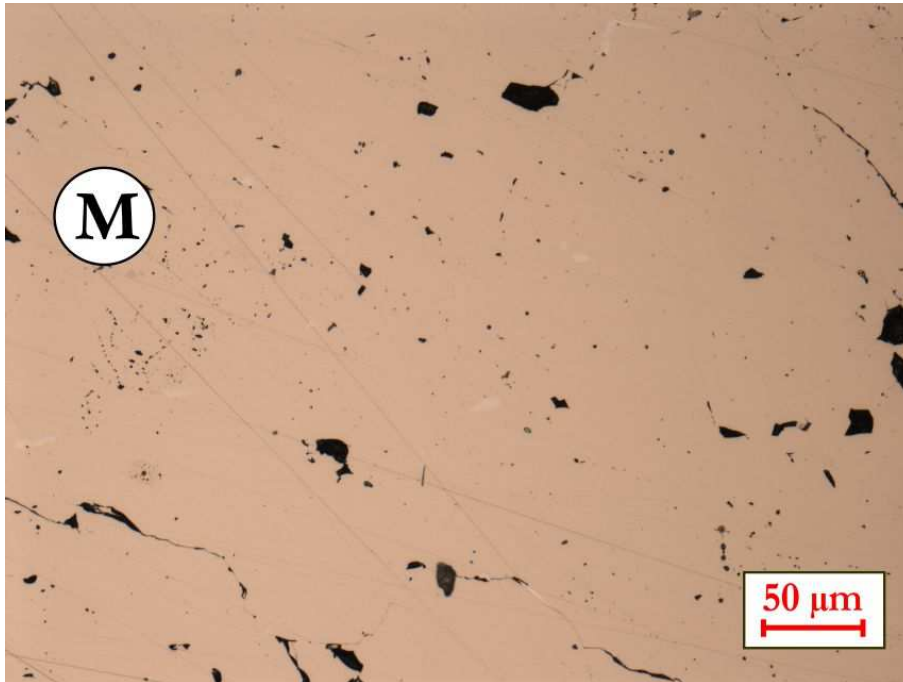
Figure 35: Dense magnetite with gangue material and some pores.

Table 4: Summary of the ore type classification according the reducibility of the samples CI, HA, SI, AC and KI.

Ore type	Hematite hypidiomorphic idiomorphic			Hematite xenomorphic			Martite dense porous			Magnetite dense		Hematite Martite	Limonite	Reducibility
	s	m	c	s	m	c	s	m	c	crys.	relict	tr, vf		
CI1			major					rare			rare	minor		excellent
CI2	rare					sole								bad
CI3			major			major			major					intermediate
HA1			major			major				rare				bad
HA2			sole											good
HA3						major			minor					good
HA4				sole										good
SI1	rare				sole									bad
SI2	minor				major									intermediate
AC1	major											major		excellent
AC2	major		minor									major		excellent
KI1										sole				bad

Content (vol.%)

sole >95%	(black)
major 20-95%	(dark grey)
minor 19-1%	(medium grey)
rare <1%	(light grey)

Reducibility

excellent	(black)
good	(dark grey)
intermediate	(medium grey)
bad	(light grey)

3.3. Pellets

Figure 36: A pellet sample.

Pellets are produced by agglomeration of very fine iron ores or concentrates to enlarge the grain size and to make a shippable burden material. Thus, pellets must satisfy chemical and mechanical strength requirements. The pelletization takes place in two steps: firstly, forming green pellets of appropriate size (9- 16 mm in diameter) by moistening with water and adding binder in a pelletizer (drum or disk), and second by firing the green pellets at 1200 – 1300 °C to build bridges between ore particles. The temperature is slightly below the melting point. The pellets (Figure 36) are strengthened by recrystallization across the ore particles during firing. The binder is required to stick the pellet feed together until the final firing takes place. Binders can be divided into two main types: mineral binders and organic binders. Bentonite is commonly used as a binder and contains mainly Al and Si, that work as slag former in the reduction process. Therefore the development of organic binders, as well as a combination of organic/bentonite composite binders started in the 1990's (Lu 2015; Eisele and Kawatra 2003).

The quality of the fired pellets, regarding mechanical strength and metallurgical properties, depends on their mineralogy and structure. The mineralogy of the product is determined by the size, chemistry, and mineralogy of the pellet feed as well as other additives and the firing conditions. In general, the pellet feed consists of different iron ore types (magnetitic or hematitic fines). Magnetite concentrates are more suitable because magnetite is oxidized to secondary hematite (change of lattice structure) in the preheating stage, which will build bridges between the particles at during faster. In addition, a hematite pellet feed often needs flux and a higher temperature to achieve appropriate quality. The crystal lattice structure does not change, and additional slag bridges are generated. Fluxes can be added to optimize basicity and MgO for increasing metallurgical performance like reducibility, degradation and prevention of strong swelling (Dwarapudi et al. 2011). The reducibility depends mainly on the mineralogy and texture of the fired pellets (Lu 2015).

To sum up, the mineralogy is one of the key factors for the quality of pellets (Umadevi et al. 2011). After firing the pellets consist mainly of hematite, glass, and pores. Magnetite can occur if the pellet is insufficiently fired. Accessory Ca-(Mg) - ferrites and fayalite can occur. The shape of the mineral grains and the bridges are indicators for good recrystallization of the particles during pelletization. The porosity is generally higher in iron ores. The burning process of the pellets has an influence on the microtexture of the pellets. Well burned pellets show partly melting textures along the margin, with a higher amount of glass. Badly burned pellets have a high amount of magnetite in the cores and the bridges between the iron oxides are less developed. The key factors for the reducibility are the crystal size or cluster size of the iron oxides, the position of the glass (within, around iron oxides or around the pores) and the pore size and distribution.

Sample description

Nine different commercially available pellet brands were investigated in this thesis. Six of them are from mainly hematitic ore mixtures, two from mainly magnetitic ore mixtures and one from a limonitic ore. The samples were provided by the industrial partners and the countries of origin are given in Table 5.

Table 5: Countries of origin of the investigated pellet samples.

	BR1	AL02	MP03	TA04	TU05	KP06	CV07	PO08	RR09
Country	Brazil	Chile	Sweden	Australia	Brazil	Sweden	Brazil	Europe	Australia

BR01

BR01 pellets consist of hematite, glass, and pores. The pores are homogenously distributed, and their sizes vary. Glass occurs as drops and between the hematite crystals. The pellets are well burnt. Bridges between the hematite fines are visible. The hematite crystals are rounded (Figure 37). Subordinately, magnetite cores occur in coarse hematite (>130 μm).
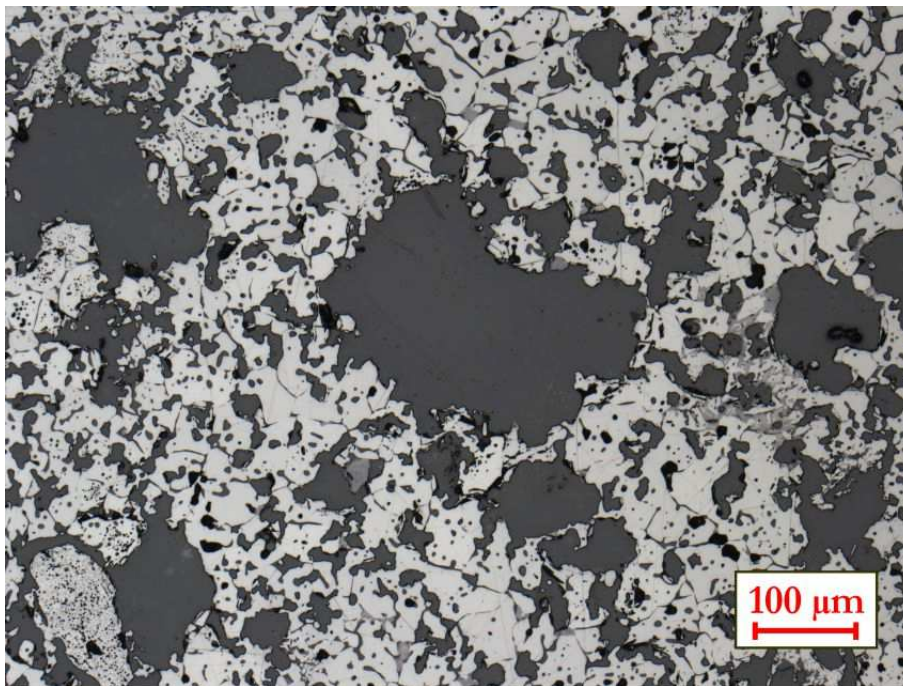
Figure 37: Rounded hematite crystals with glass droplets and as interstices.

AL02

Most of the pellet cores consist of magnetite or martite. The amount of secondary magnetite is relatively high. The crystal size of the hematite varies from core to margin. The glass phase occurs in interstices between the minerals. The high magnetite content in the pellet cores is an indicator of a poor burning process (Figure 39). Bridges between the grains are visible, but the hematite is partly angular. The pores are evenly distributed. In some cores

the porosity is higher than at the margin. In addition, the pores are partly larger than 250 µm in diameter.
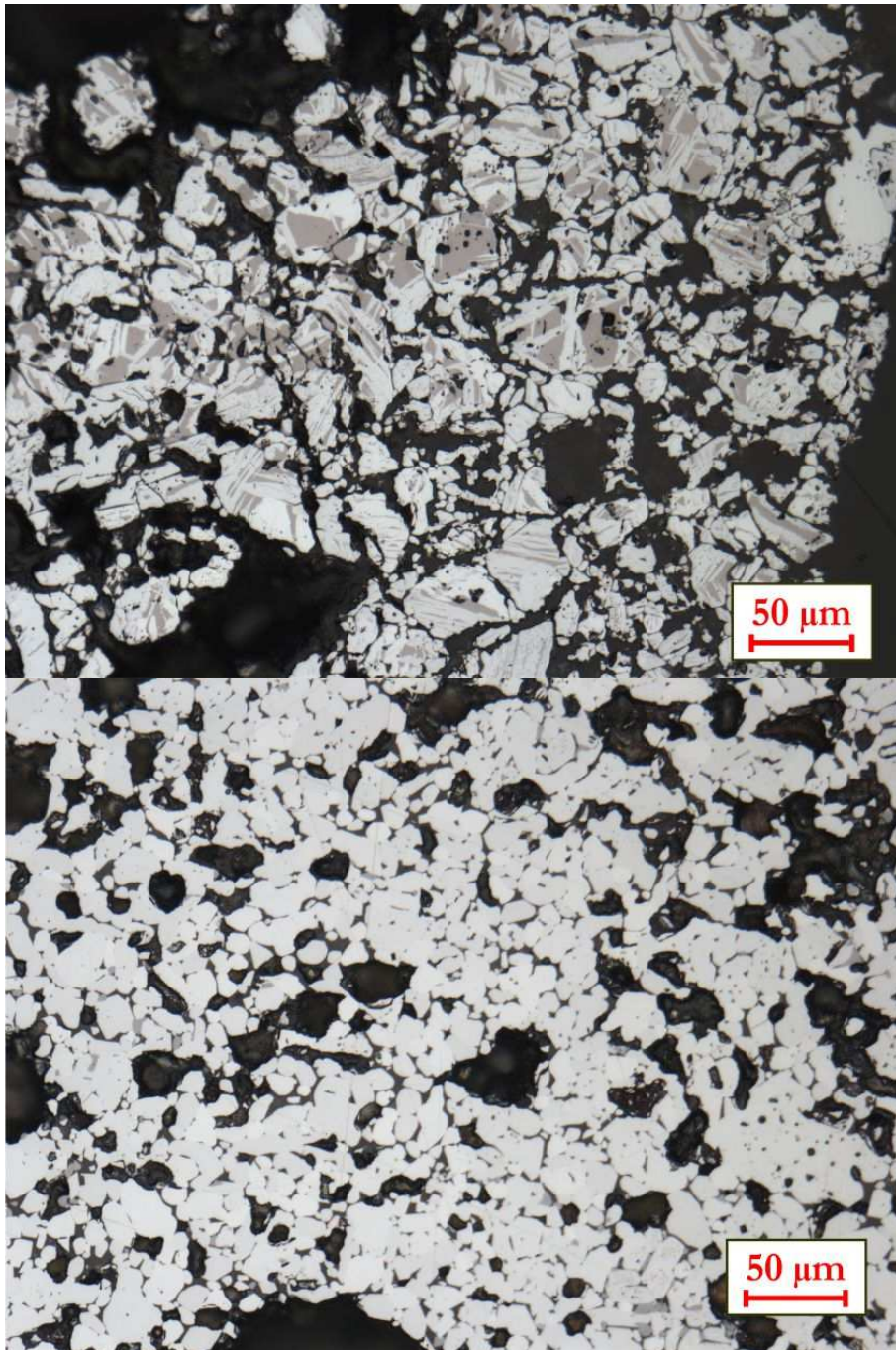
Figure 38: First - magnetite partly oxidized to martite; second - hematite with glass and pores.

MP03

The pellets are well burnt. The glass content is the lowest among the sample suite. The porosity varies between core and margin. The hematite crystals are hypidiomorphic to xenomorphic. Martite occurs mainly in the core of the pellets (Figure 39). The pores are evenly distributed and connected.
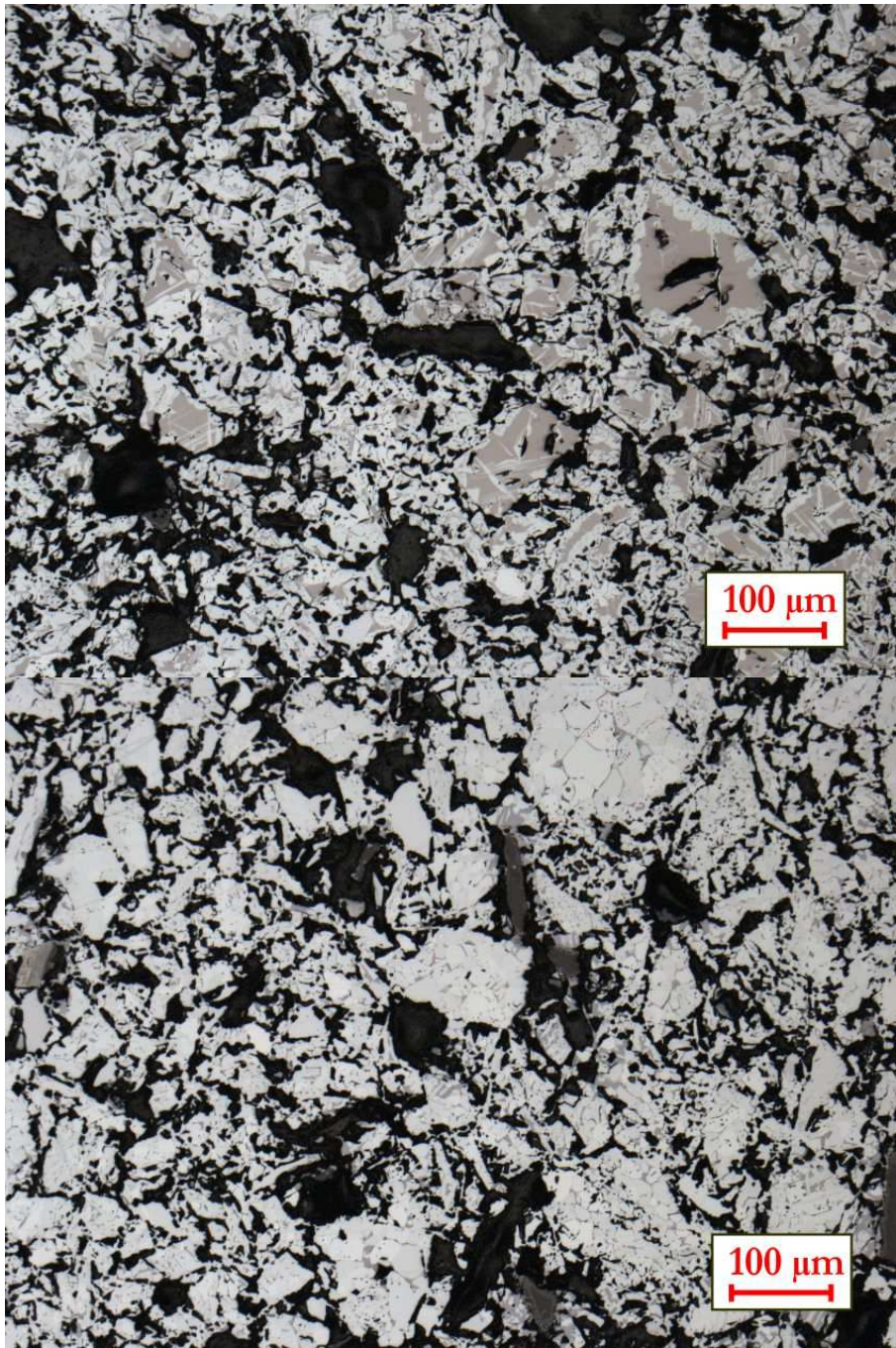
Figure 39: First - martite and hematite, second - hematite with glass at the margin of the pellet.

TA04

The pellets have a dense texture and are well burned (Figure 40). The pores are well distributed and more or less rounded. They are less interconnected than in BR01 or AL02. The glass content is low and occurs mainly between the hematite crystals or as drops in hematite. The content of magnetite varies between 5 and 10 vol.%.
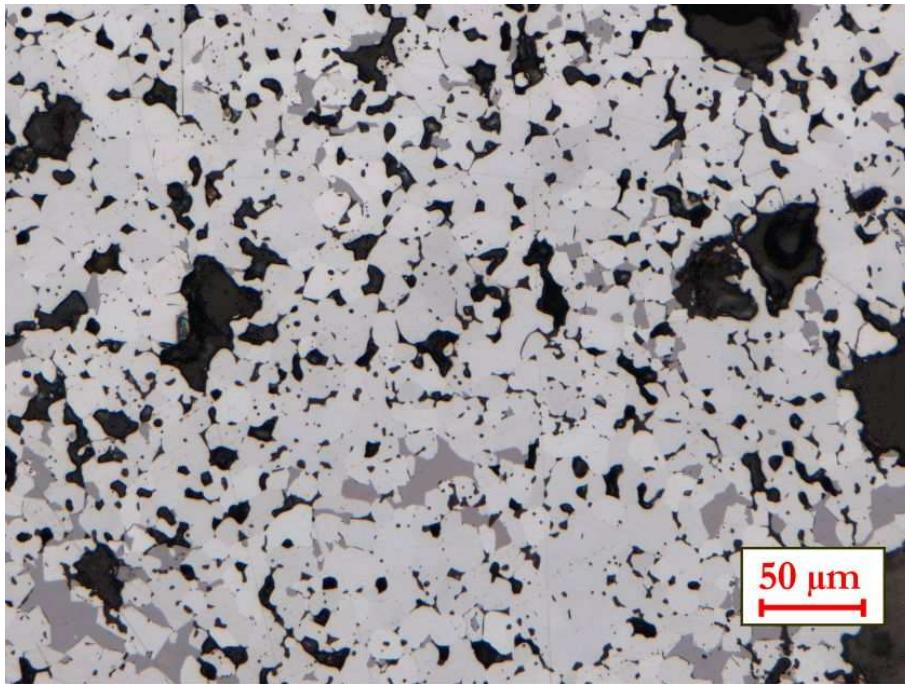
Figure 40: Hematite and Ca-ferrites (grey).

TU05

The size of the hematite crystals varies between 5 and 25 μm. The crystals are xenomorph and are more rounded in the core than at the margin (Figure 41). The glass occurs mainly in interstices between the hematite crystals. The glass content is low. The pellets are well burned, but bridges are not well developed. The pore size varies between core and margin. Subordinately, magnetite occurs in the cores.
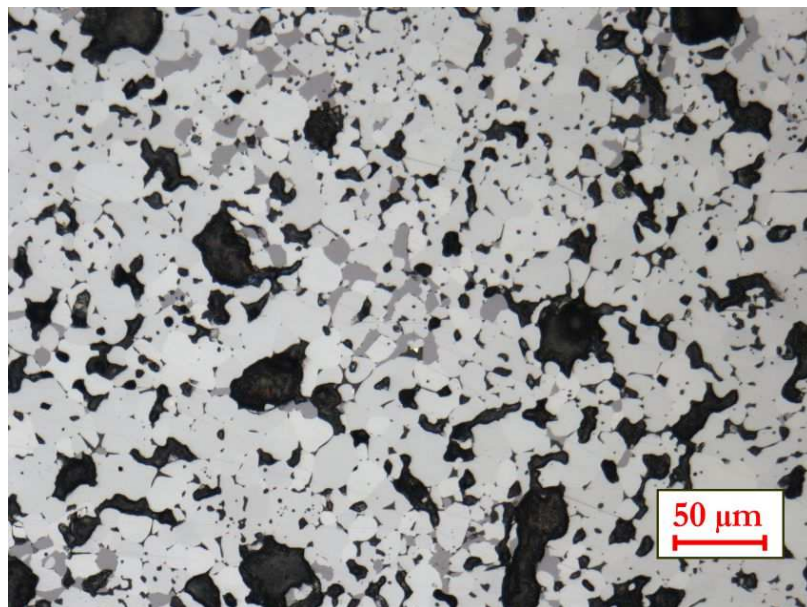
Figure 41: Coarse rounded hematite crystals with glass gaps and pores. The grey mineral is Ca-ferrite.

KP06

Most of the pellets show different grades of melting between core and margin. The hematite is more rounded in the core, whereas at the margin the crystals are hypidiomorphic. The glass phase occurs in a higher amount in the core as gap fillings and drops (Figure 42). The bridges are better developed in the core. The pores are evenly distributed, but less connected in the core.
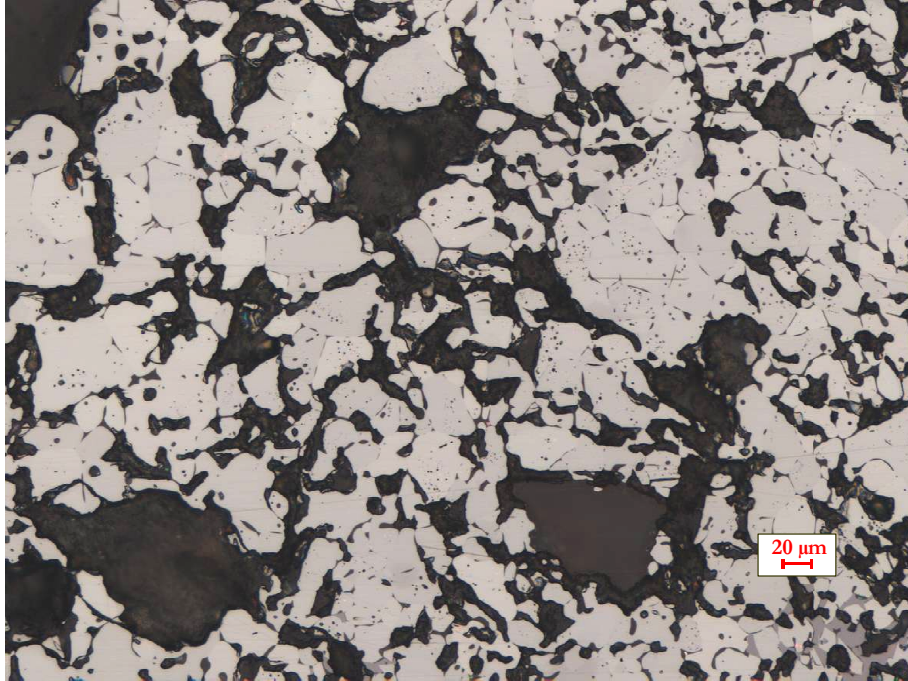
Figure 42: Hematite with glass drops and gaps.

CV07

The pellets are relatively homogenous and well burned. Magnetite cores and very dense cores with large hematite crystals are found in minor amounts. The main mineral is hematite. The appearance of hematite varies from idiomorphic to xenomorphic. The glass content is higher compared to the other samples. The glass is found as seams or interstices between the Fe-oxides (Figure 43). The bridges between the hematite crystals are less developed than in other pellet brands. The texture is medium porous with fine pores. Coarse pores are subordinated.
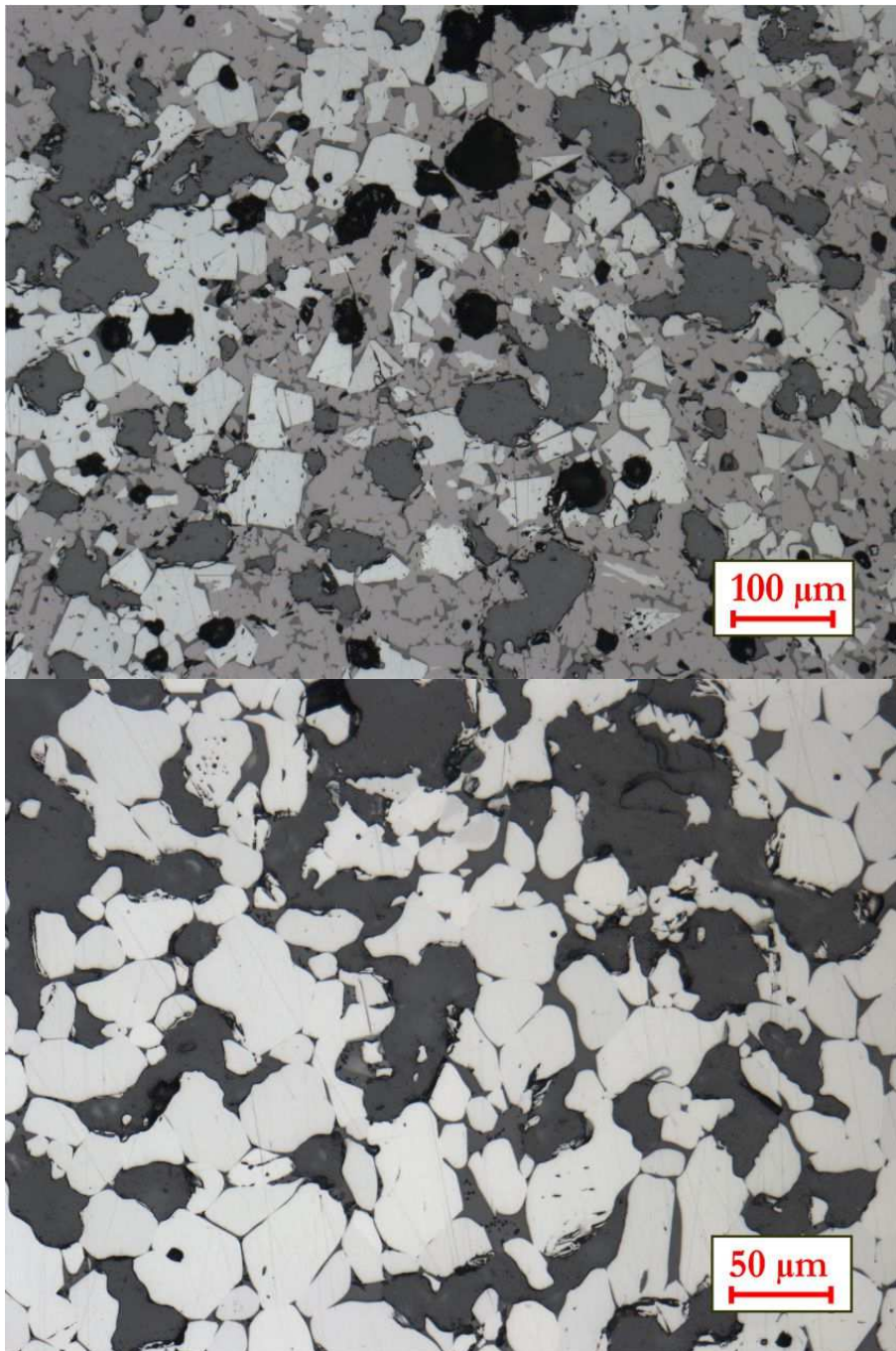
Figure 43: First - magnetite and hematite; second - well-rounded hematite with glass filled interstices in between.

PO08

The size of the hematite crystals varies between core and margin. The crystals are less rounded than in other pellet brands. The pore size differs between 2 μm and >10 μm. The glass occurs more as drops than as interstices. The amount of glass is higher in the cores of the pellets. The bridges between the crystals are less developed. Gangue from the primary raw material occurs subordinately.
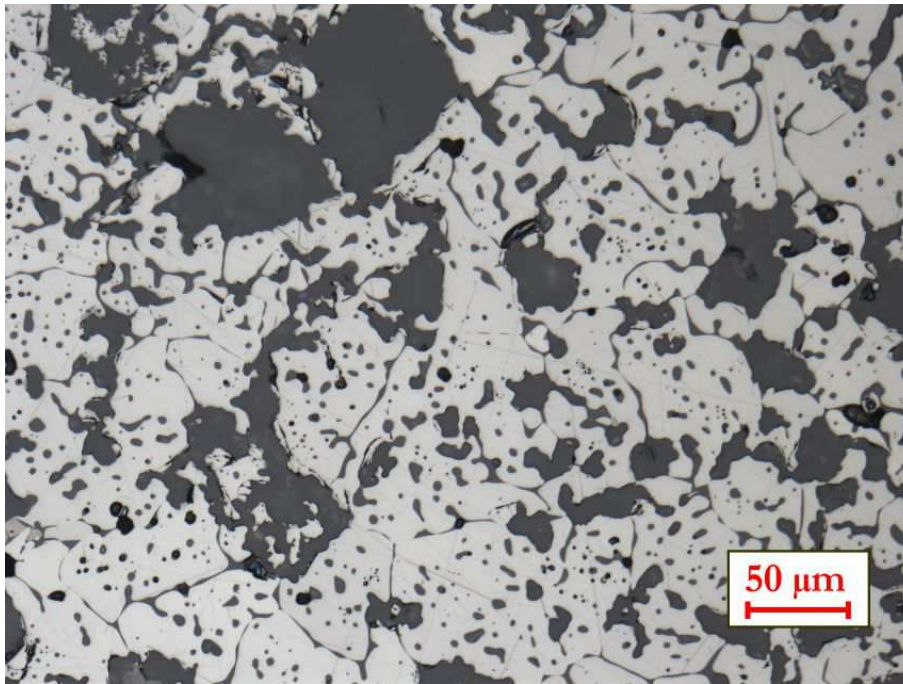
Figure 44: Well- burnt pellet with hematite and glass.

RR09

RR09 pellets are characterized by their high porosity and low Fe-oxide content. The glass phase surrounds the dominant hematite (Figure 45). The pores are finely reticulated. The texture is porous, and the size of the xenomorphic hematite crystals is small, but they are agglomerated partly to larger clusters.
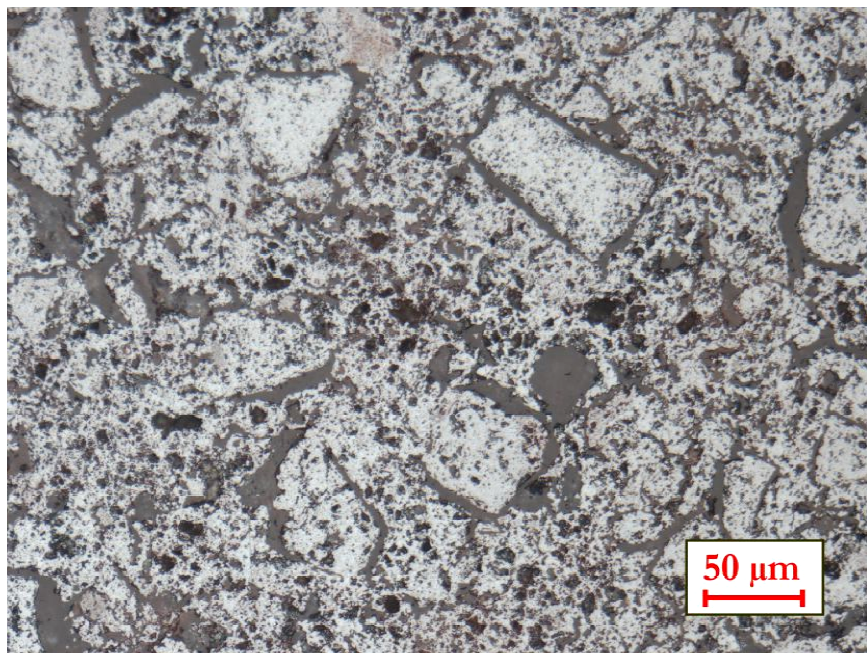
Figure 45: Highly porous, the main minera is hematite surrounded by gangue.

The pellet samples have in average over 50 vol.% of iron-oxide content. In one sample (RR9), the iron oxide content is 40 %. The crystal size of the iron oxides varies between the samples and within core and margin widely. The porosity diverges between 30 % and 50 %. The pore distribution and size vary between core and margin in all samples, too.

Due to the microscopical investigations the samples are divided into three groups. Group one consists of RR9, PO8 and CV7. These samples have a high porosity and small crystal sizes of the iron oxides. The iron oxide content is medium (56 vol.%, CV7) to low (<40 vol.% RR9). The glass content is medium (9 vol.%, PO8) to high (14 vol.%, RR9, CV7). The pores are evenly distributed, but small in average and the glass is concentrated around the pores. Group two consists of MP3, TA4, TU5 and KP6. The group is characterized by high iron oxide content (>57 vol.%) and low glass content (<6 vol.%). The pores are in average larger than in group one. Group three (BR1, AL2) is characterized by medium (56 vol.%) iron oxide content and high glass content (>10 vol.%). The glass occurs mainly as interstices to the iron oxides. The pores are well distributed and on average larger than in group one and two. The overall porosity is medium (31-34 vol.%).

To sum up, the reducibility performance is rated from good to bad:

- Group 3 (medium iron oxide content, medium porosity, larger pores)

- Group 2 (high iron oxide content, medium-low porosity, medium pores)

- Group 1 (low oxide iron content, high glass amount around the pores, small pores)

The glass phase and the epoxy resin are often difficult to distinguish and are illustrated by a false colour image in Figure 46. The glass phase is slightly brighter than the epoxy resin.
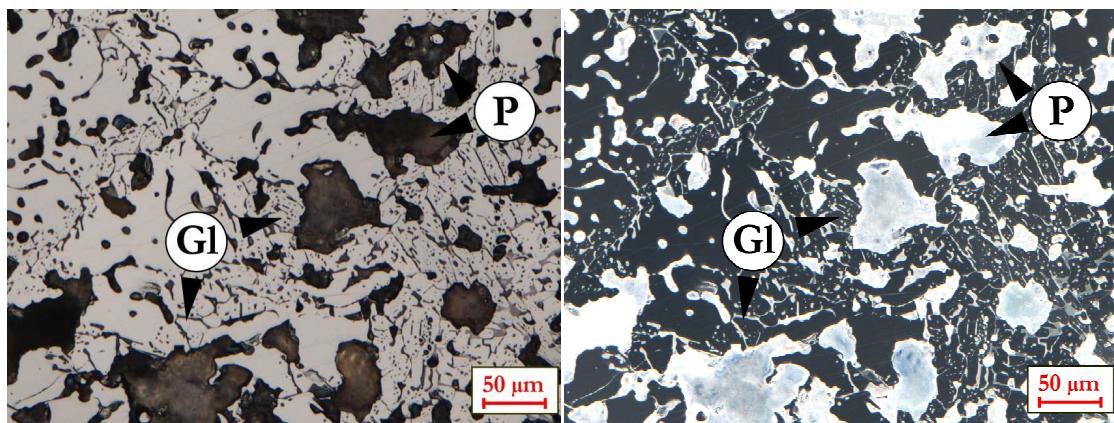
Figure 46: The original images of a pellet and the false colour image.

More detailed results were achieved by image processing analyses, see chapter 5.3.

3.4. Sinter

Figure 47: Sinter sample 10-12 mm

In general, sinter (Figure 47) is produced on site at the iron making facilities. The raw mixture consists of several fine ores, returned sinter material (< 5 mm), fuel (e.g. coke breeze or anthracite), flux (e.g. limestone, burnt lime or dolomite), moisture and recycling material.

At sintering, the raw mixture is loaded as a bed on a strand traveling-grate. The top bed is ignited under the hood and air is drawn through the grate. The flame front moves downwards and heats the mix over 1300 °C. Partial melting and softening occur at the surface of the particles. Water evaporates and gas, from burnt coke, is driven off. This hot waste gas dries and preheats the lower layers of the bed. Crystallization into several mineral phases takes place during subsequent cooling. After that, the sinter is hot screened and the fines (< 5 mm) are returned to the mixing drum. The sinter then is composed mainly of magnetite, Mg-Ca-ferrites, gangue (glass), hematite and pores (Figure 48). Ore relicts can occur. They consist mostly of large dense iron ore particles.

Depending on the blast furnace the sinter is produced as three different types, in respective basicity:

- Acidic: CaO/SiO_2 ratio < 1.0

- Fluxed: CaO/SiO_2 ratio 1.0-2.5 (most common type)

- Super-fluxed: CaO/SiO_2 ratio > 2.5

The quality of sinter is influenced by granulation, flame front properties, mineralogy of the used ores, the basicity and the mineralogy of the sinter itself (Chaigneau 1994; Hsieh 2005; Higuchi et al. 2006; Kalenga and Garbers-Craig 2010; Paananen 2013; Mochón et al. 2014). Some of the properties are represented by the TI, RDI and R values, but the mineral abundance is not determined in the daily routine of the sinter analyses.

A wide range of phase reactions, transformations and crystallization take place during the sinter process. During the preheating magnetite (if present) is oxidized. At 400 °C the calcination of carbonates starts. The mineral composition of the final sinter depends mostly on the basicity. Higher basicity means an increasing amount of Ca, and the amount of Ca-ferrite increases. Depending on the oxidation and reduction conditions and the availability of elements like Mg, Al, magnetite, hematite and SFCA (Si-ferrites of Ca and Al) are formed during cooling. Due to the rapid heating and cooling, no equilibrium between the mineral phases and the melt takes place.

Sample description

Two different fresh sinter samples were investigated. Both were provided from industrial partners. The samples SIN01 and SIN02 were used to develop the VisuMet sinter phase quantification. In addition, the validation by point counting was made with these two samples.

SIN01

Up to 50 vol.% of the sample SIN01 is hypidiomorphic to xenomorphic magnetite (Figure 48). Secondary coarse idiomorphic hematite crystals are subordinately present (4 vol.%). Most of them are located near to pores. The glass content does not exceed 26 vol.%. The Ca-ferrites are blocky, acicular SFCA are rare.

According to the VisuMet analyses and the point counting of the sections the porosity does not exceed 10 vol.%. This is due to the magnification effect. The pores are larger than the image width, and black images are sorted out (chapter 4.3). The overall porosity of the sinter is higher compared to SIN2.
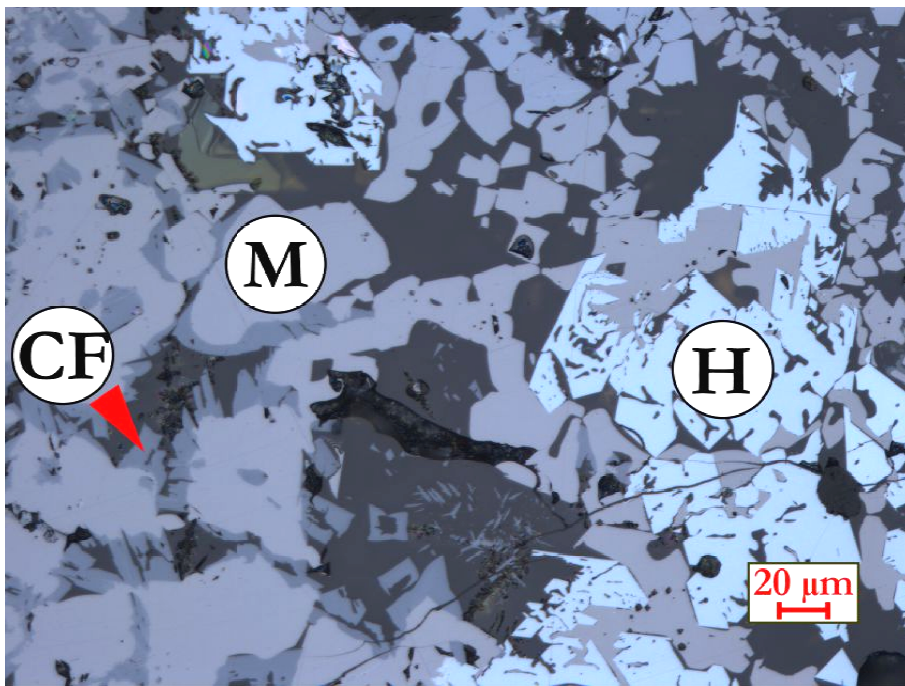
Figure 48: Sinter with magnetite (M), Ca-ferrites (CF), hematite (H) and glass (dark grey).

SIN02

SIN02 consists mainly of hypidiomorphic to xenomorphic magnetite (43 vol.%) (Figure 49). The blocky CFs are subordinate, whereas the acicular SFCA's content is higher than in SIN01 (24 vol.%). Hematite is present as relicts of not sintered fine iron ores (3 vol.%). The content of smaller pores (smaller than the image width in diameter) is higher than in SIN01 (15 vol.%). The overall porosity is approximately 30 vol. %.
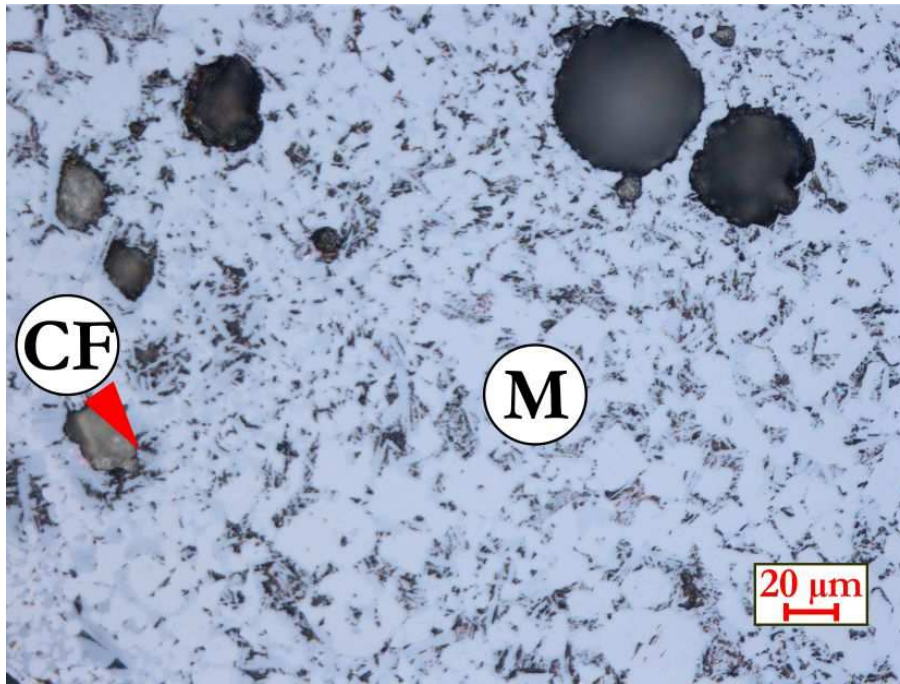
Figure 49: Image of SIN02, hypidiomorphic magnetite (M) surrounded by blocky-acicular Ca- ferrites (CF).

3.5. Evolution during the reduction process

Iron ore is a mixture of iron minerals. In the blast furnace iron ores, pellets and sinter, beside coke, flux etc., interact with the reducing gases. This produces metallic iron over a series of stages via intermediate oxides. The simplified pathway is: Limonite-> hematite-> magnetite-> wuestite and finally metallic iron. Hematite is the most thermodynamically stable iron oxide in this sequence (Cornell and Schwertmann 2003).

During the reduction in the blast furnace several chemical reactions take place. The main reactions are shown in Figure 50. Theoretically, the transformation of 6 mol hematite to 12 mol metallic iron needs an elimination of 9 mol O_2 in total. One third of the oxygen is separated during the reduction of hematite to magnetite and to wuestite. The final transformation step from wuestite to metallic iron must eliminated two third of the oxygen and takes more time.

$3Fe_2O_3 + CO \rightarrow 2Fe_3O_4 + CO_2$
$Fe_3O_4 + CO \rightarrow 3FeO + CO_2$

$FeO + C \rightarrow Fe + CO$
$MnO + C \rightarrow Mn + CO$
$P_2O_5 + 5C \rightarrow P_2 + 5CO$
$SiO_2 + 2C \rightarrow Si + 2CO$

$C + O_2 \rightarrow CO_2 \rightarrow CO_2 + C \rightarrow 2C$

$SiO_2, CaO, Al_2O_3, MgO, MnO$
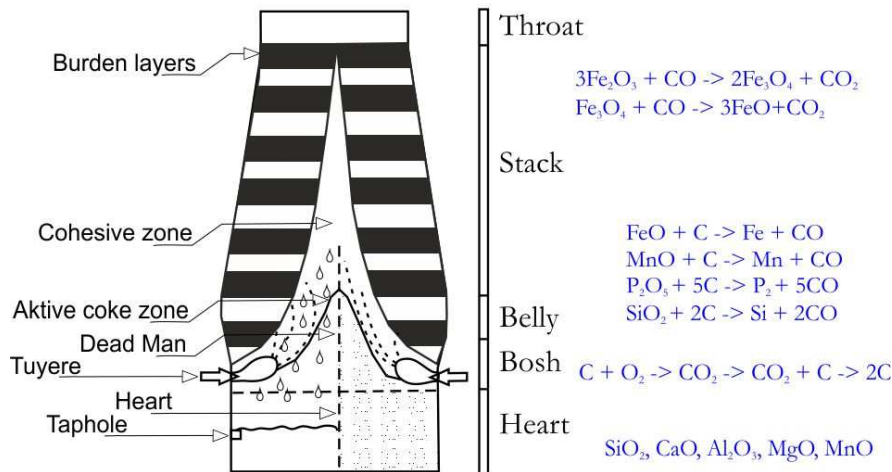
Figure 50: Schematic profile of a blast furnace with the predicted chemical reactions.

Hematite, magnetite and wuestite have a closed-packed structure of oxygen ions. In the transforming step from hematite to magnetite the lattice changes from hexagonal to cubic. In the magnetite to wuestite step only the iron oxygen ratio changes. In-situ XRD analyses of hematite reduction demonstrate that there is a transition zone, where the phases coexist (Jozwiak et al. 2007).
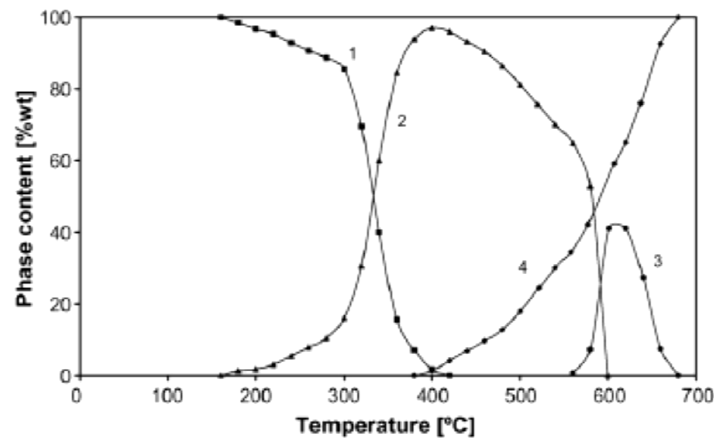
Figure 51: Phase composition during "in-situ" XRD temperature programmed reduction of hematite in 5% H_2-95 % Ar atmosphere. (1) Hematite, (2) Magnetite, (3) Wuestite, (4) Metallic iron, after Jozwiak et al. (2007).

The value of the oxygen potential of the iron minerals increases in the following order: hematite > magnetite > wuestite. So, the ratio of CO/CO_2 has to get higher for the complete reduction reaction from magnetite to metallic iron. Indirect reduction of all iron minerals takes place below 1000 °C. However, direct reduction of iron minerals besides wuestite is negligible. Wuestite is directly reduced by carbon and hydrogen over 1000 °C. The reduction rate is determined by the last step of the reduction sequence from wuestite to metallic iron (Bogdandy and Engell 1967).

Wuestite (FeO) is not stable below 570 °C. It disintegrates into iron and magnetite. The colour is dark grey in reflected light similar to limonite. In general two different types of wuestite can be investigated in reduced samples: porous wuestite (Figure 52, a) and a dense wuestite without or containing minor inner pores (Figure 52, b).
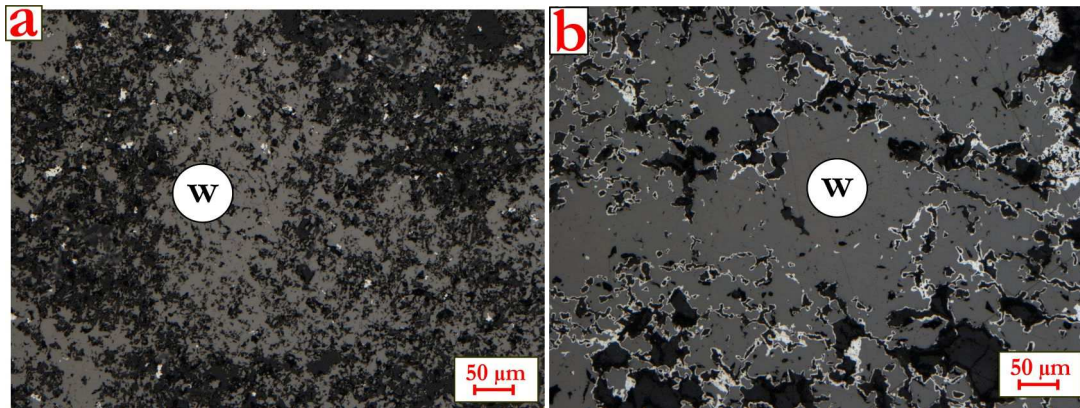
Figure 52: a) Wuestite (w) with metallic iron specks (white); b) Wuestite (w) with metallic iron shell (white).

The metallic iron forms different structure types depending on the reduction conditions (temperature, gas mixture, time) and on the primary morphology of the iron oxides.
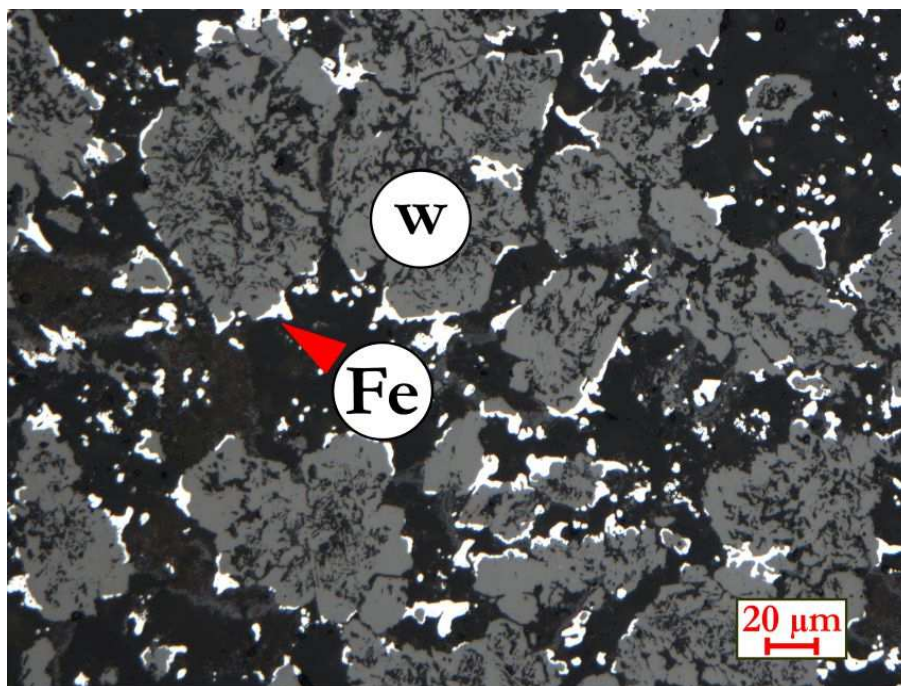
Figure 53: Iron sparks (whisker) grown at the edges of wuestite (dark grey).

The main forms of metallic iron occurring in the ISO-4695 tests are:

- Iron specks (Figure 52a)

- Iron sparks (Figure 53, Figure 57)

- Porous iron (Figure 55, b)

- Iron layers (Figure 63)

Nevertheless, the shape, the crystal size, the texture as well as the genesis of the iron oxides affect the reduction process to metallic iron. To determine the different influences on the reduction process, it was necessary to follow the mineral transformation and structural evolution. Twenty samples of lump ore, pellets and sinter were tested according to ISO-4695 conditions at the Chair of Ferrous Metallurgy (MUL). The tests were interrupted to follow the morphological evolution in detail. The partly reduced samples were compared to the raw material under the microscope.

The structural evolution of the iron oxides can be summarized and simplified in five main reduction paths (Figure 54).

l.........limonite	s	small (2-10 μm)
h1......hematite	m	medium (10-20 μm)
h2......secondary hematite	c	coarse (>20 μm)
mr.....martite	x	xenomorph
m1.....magnetite	h	hypidiomorph
m2.....secondary magnetite	i	idiomorph
w........wuestite	tr	trellis
	vf	very fine (<2 μm)
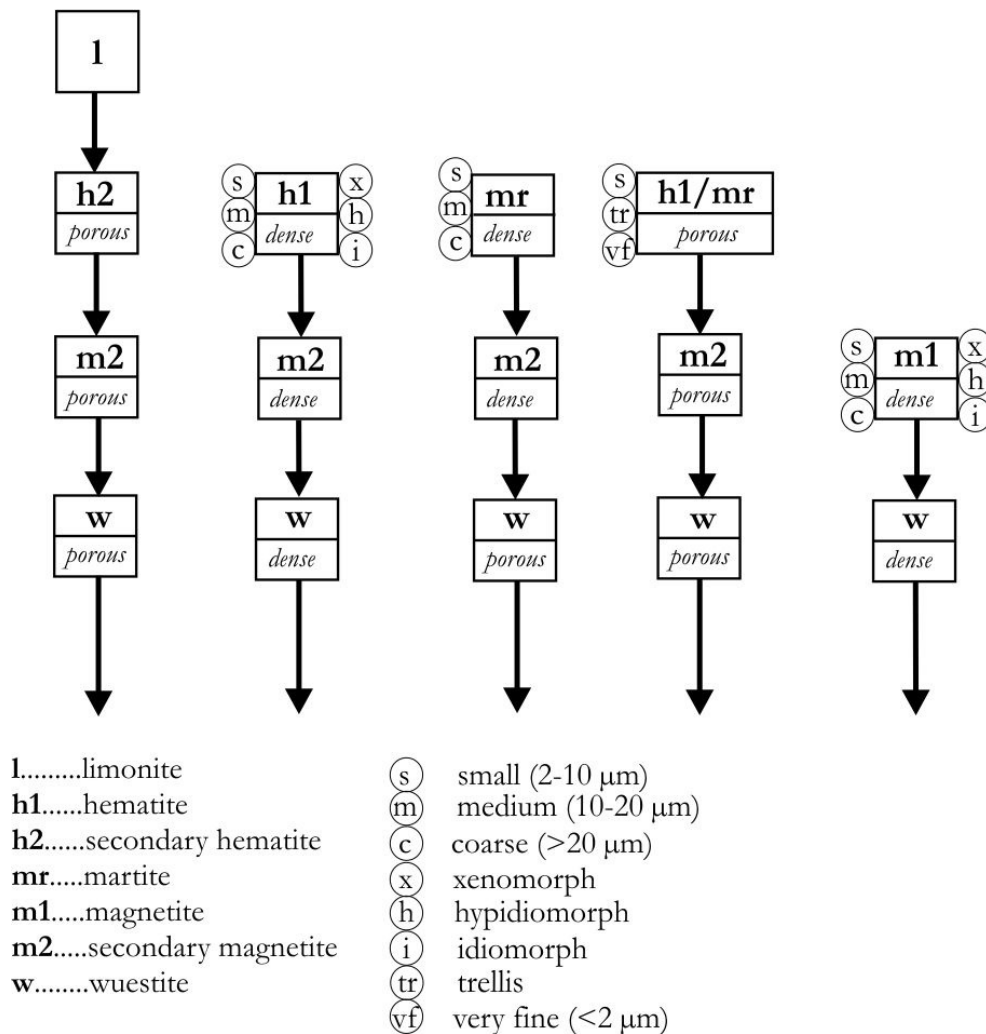
Figure 54: Summary of the structural evolution of the iron (hydro-) oxides during the ISO-4695 test.

They are described as follows:

Limonite path

In the first step limonite (l) is reduced to hematite (h2, porous) (Figure 55). A finely porous hematitic mass is formed. This hematite sponge is rapidly transformed to porous magnetite and further to porous wuestite (Figure 55). Due to the high specific surface, the intermediate steps (h2p and m2p) were not observed in the reduced samples under ISO-conditions. Only the porous wuestite and spongy iron is visible.
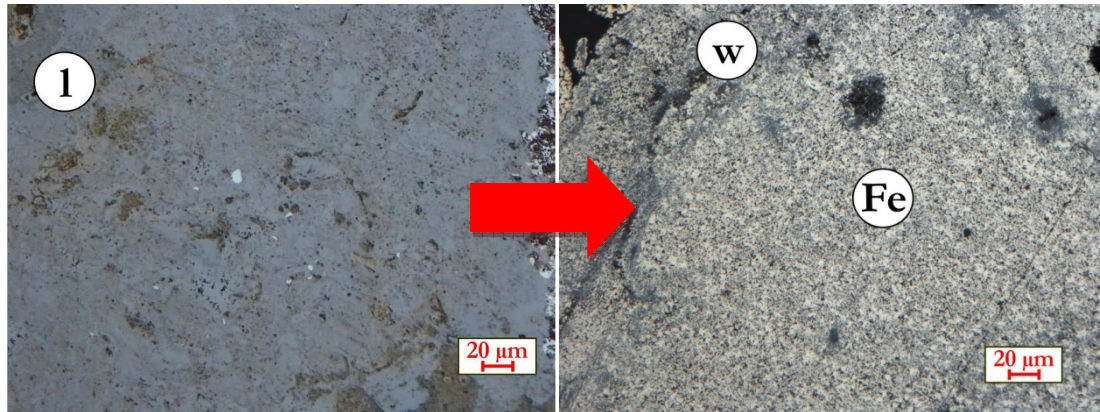
Figure 55: Limonite (l) will be reduced to spongy iron (Fe).

Hematite path

Hematite (h1) occurs in many morphological types, but the main difference in the reduction behavior is the inner porosity of the hematite grains. A dense hematite grain or crystal, wherever it is small or coarse, xenomorphic or idiomorphic will transform to dense magnetite (m2, dense) (Figure 56). The dense magnetite (m2, dense) type is reduced to dense wuestite (w, dense) (Figure 57).
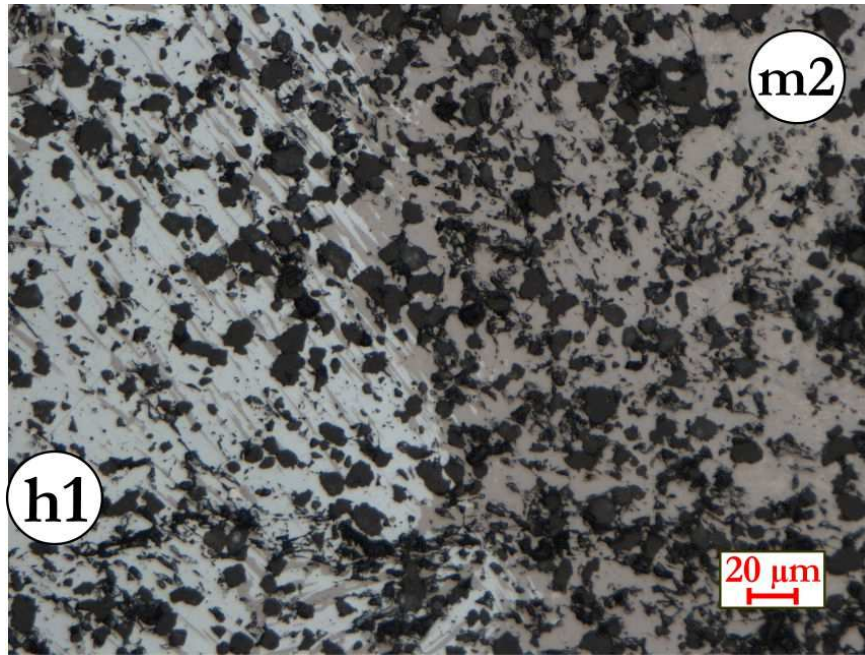
Figure 56: Transformation of hematite (h1) to magnetite (m2) during ISO-4695 test.
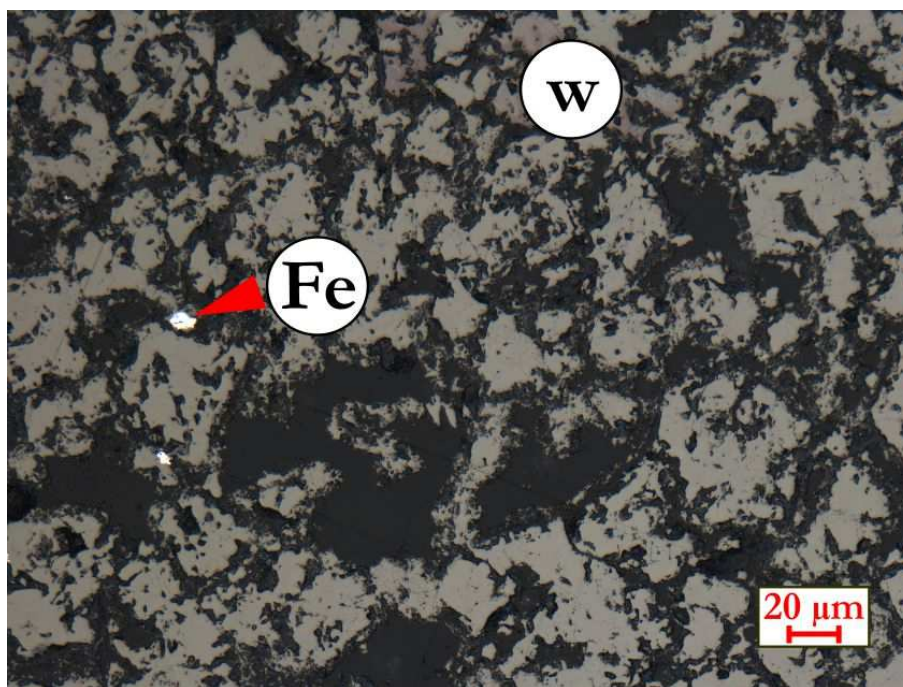
Figure 57: Beginning of the metallization of wuestite (w), some iron sparks (Fe) are already visible.

Figure 58 shows the entire hematite path. In the middle of the sample grain the hematite (h1) is still present. The hematite is surrounded by a shell of m2 magnetite. The shell is approximately 300-200 μm thick. The transition to wuestite (w) is continous, due to similar reflectance. Parts of the wuestite are slightly brighter, which is interpreted as the beginning of the metallization.
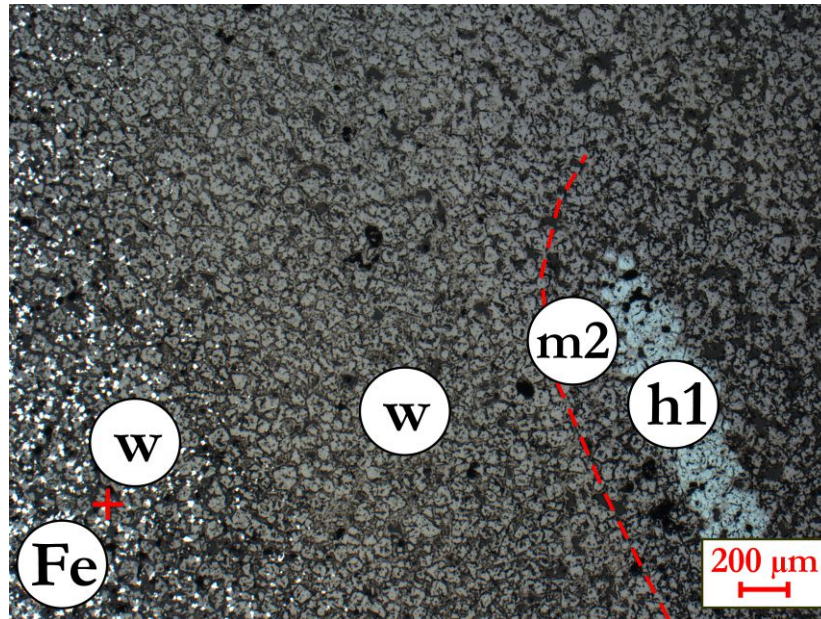
Figure 58: The hematite path in one image. Hematite (h1) is still present in the core, surrounded by a small band of magnetite (m2). The metallization with iron sparks (Fe) already started at the margin of the ore grain within the wuestite (w) zone.

Martite path

Dense martite (mr) with grain size larger than 10 μm will form the same type of magnetite (m2, dense), like in the hematite path (Figure 59). The difference to the hematite path is in the next step. The dense m2 magnetite is transformed to porous wuestite (w, porous) due to the pseudomorphous structure of the former martite. The dense m2 "remembers" the cleavage and crystal outlines of the ancient martite, which leads to bigger surface of wuestite for the reduction gas (Figure 60).
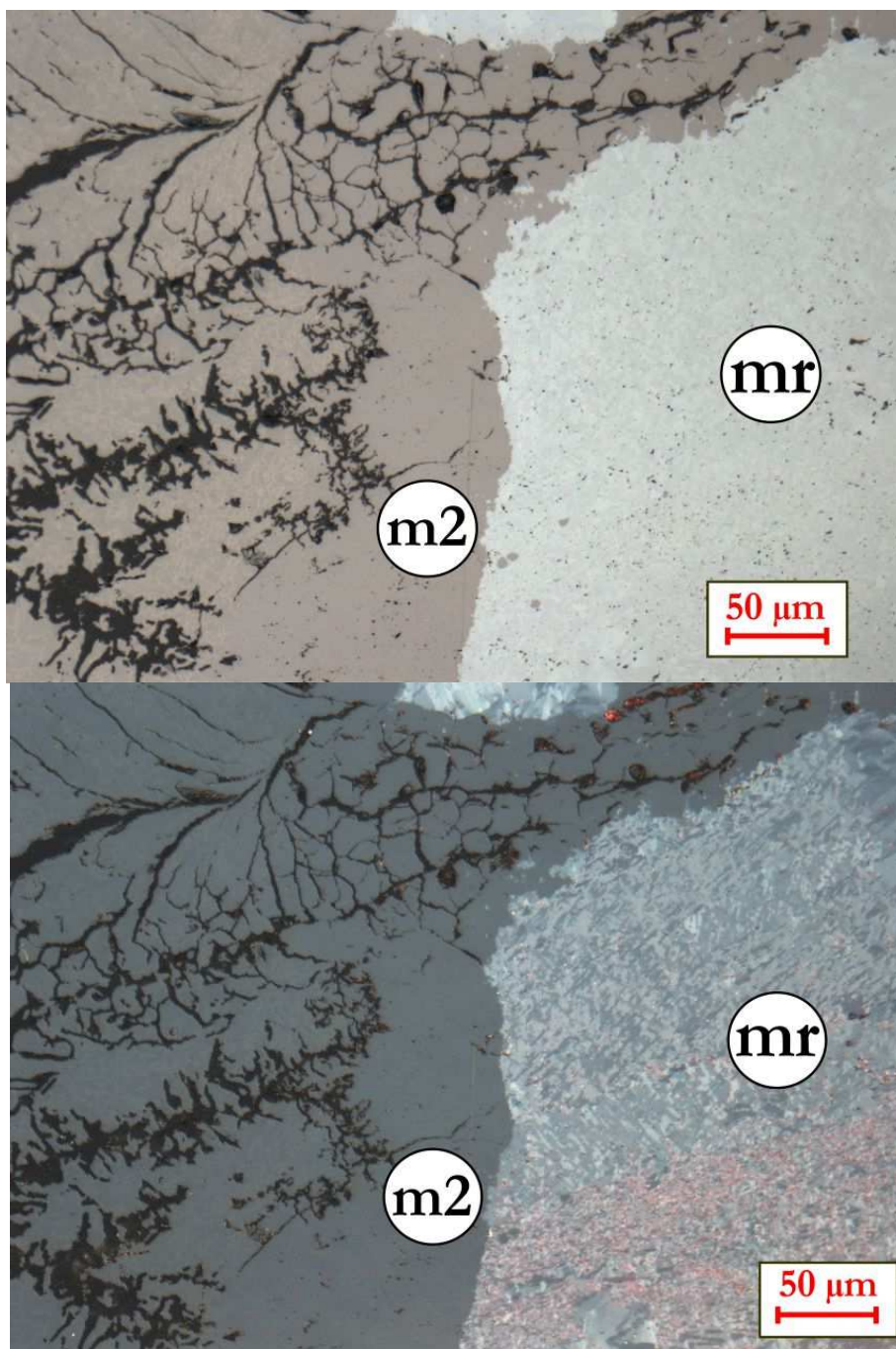
Figure 59: Dense trellis martites (mr) and the dense transformed magnetite (m2). Under-crossed nicols.
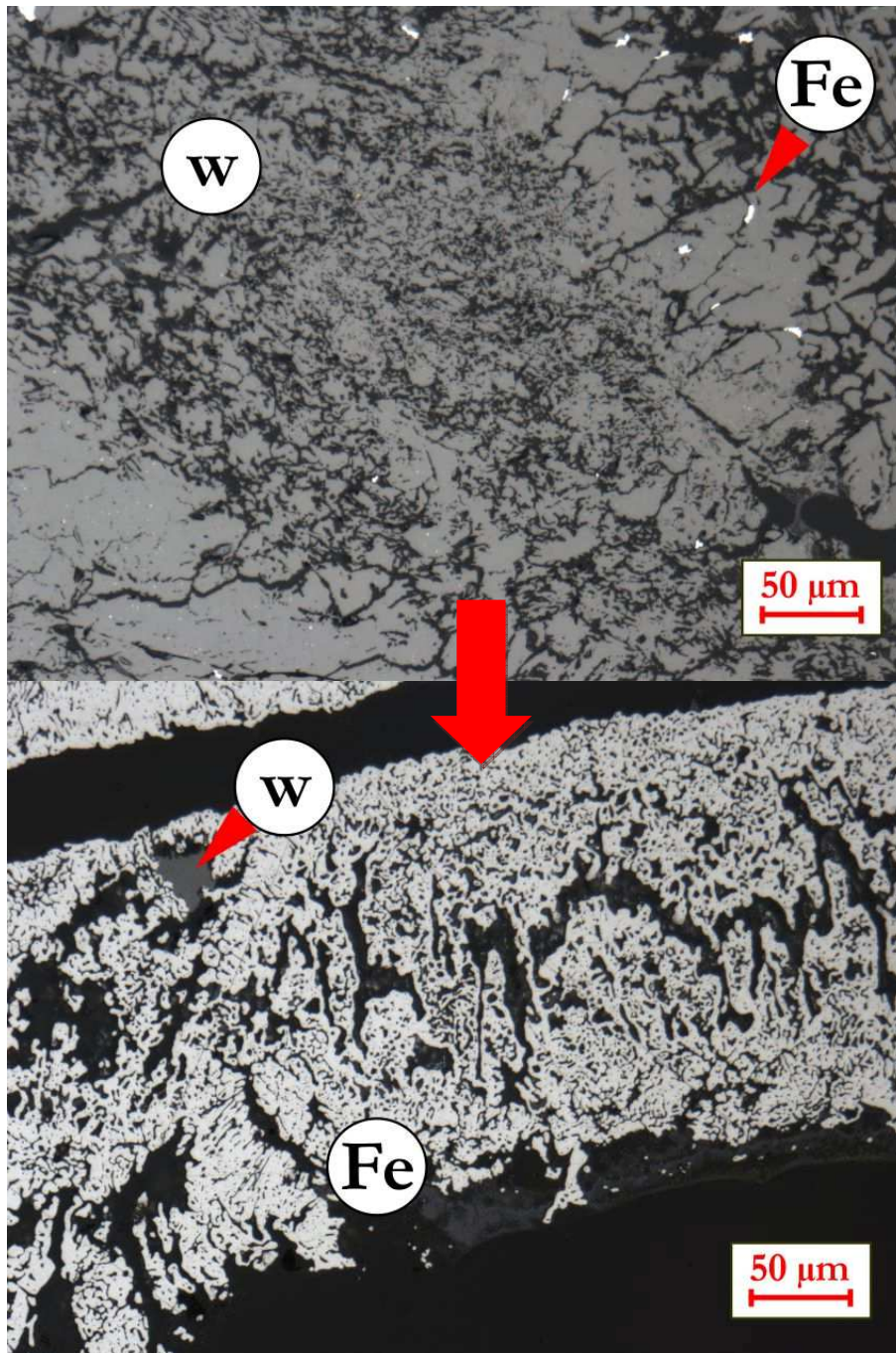
Figure 60: The spongy Fe$_{met}$ (Fe) is generated from a former dense mr via m2 (dense) and w (porous).

Hematite/martite path very fine

The starting mineral of this path is a porous small to very fine hematite (h1, porous) (Figure 61, a). A porous m2 magnetite is formed at first, which leads to a porous wuestite (w) in the next step (Figure 61, b). The intermediate step m2 was not observed in the reduced samples due to the rapid transformation to wuestite.
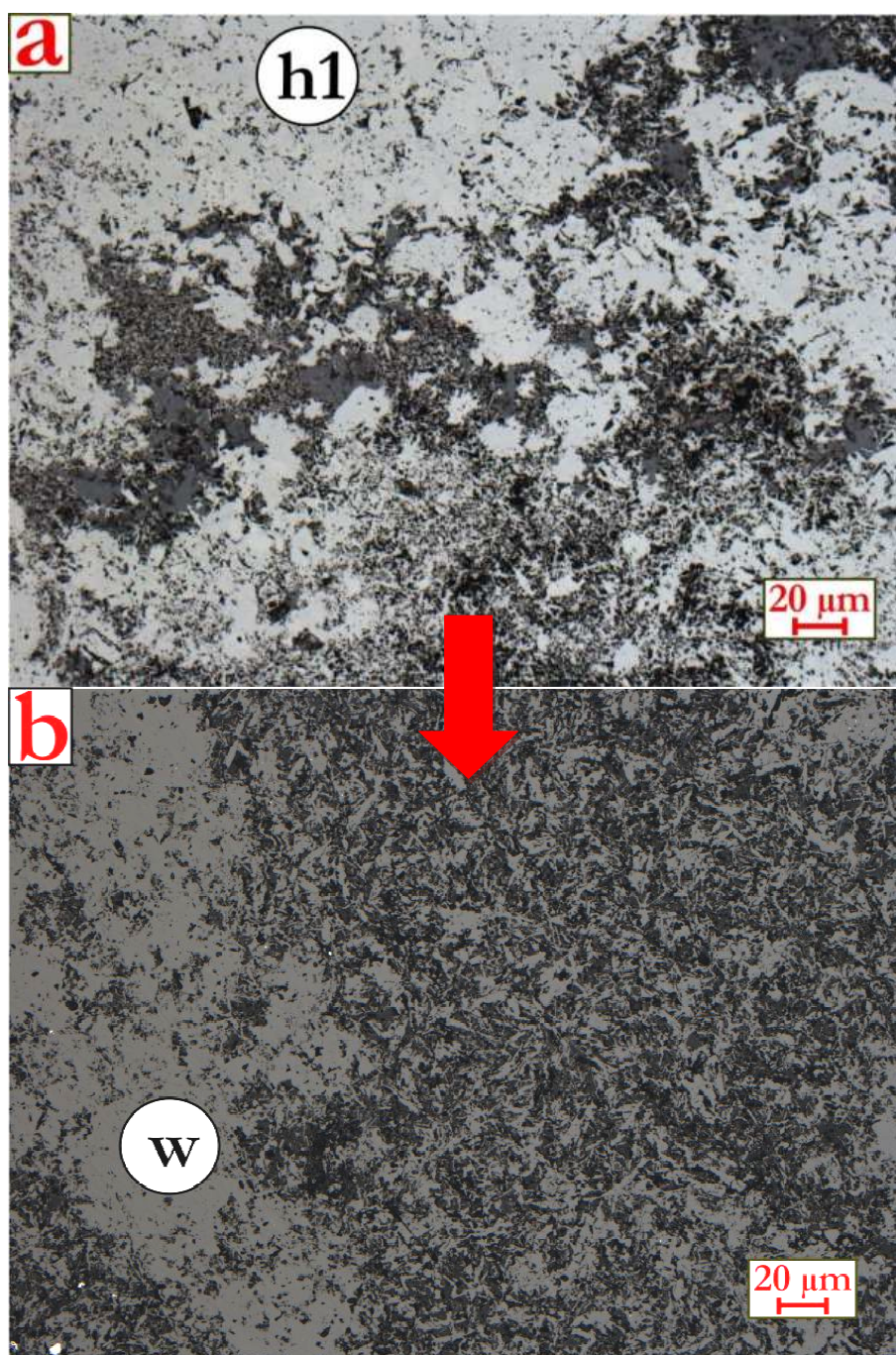
Figure 61: a) Very fine hematite (h1) will be reduced to b) porous wuestite (w).

Coarse trellis martite (mr) with magnetite cores will be reduced to magnetite (m2, porous) and further to porous wuestite (w, porous). Metallic iron appears usually first in the former hematite lamellae, whereas the former magnetite cores are still wuestite (Figure 62).
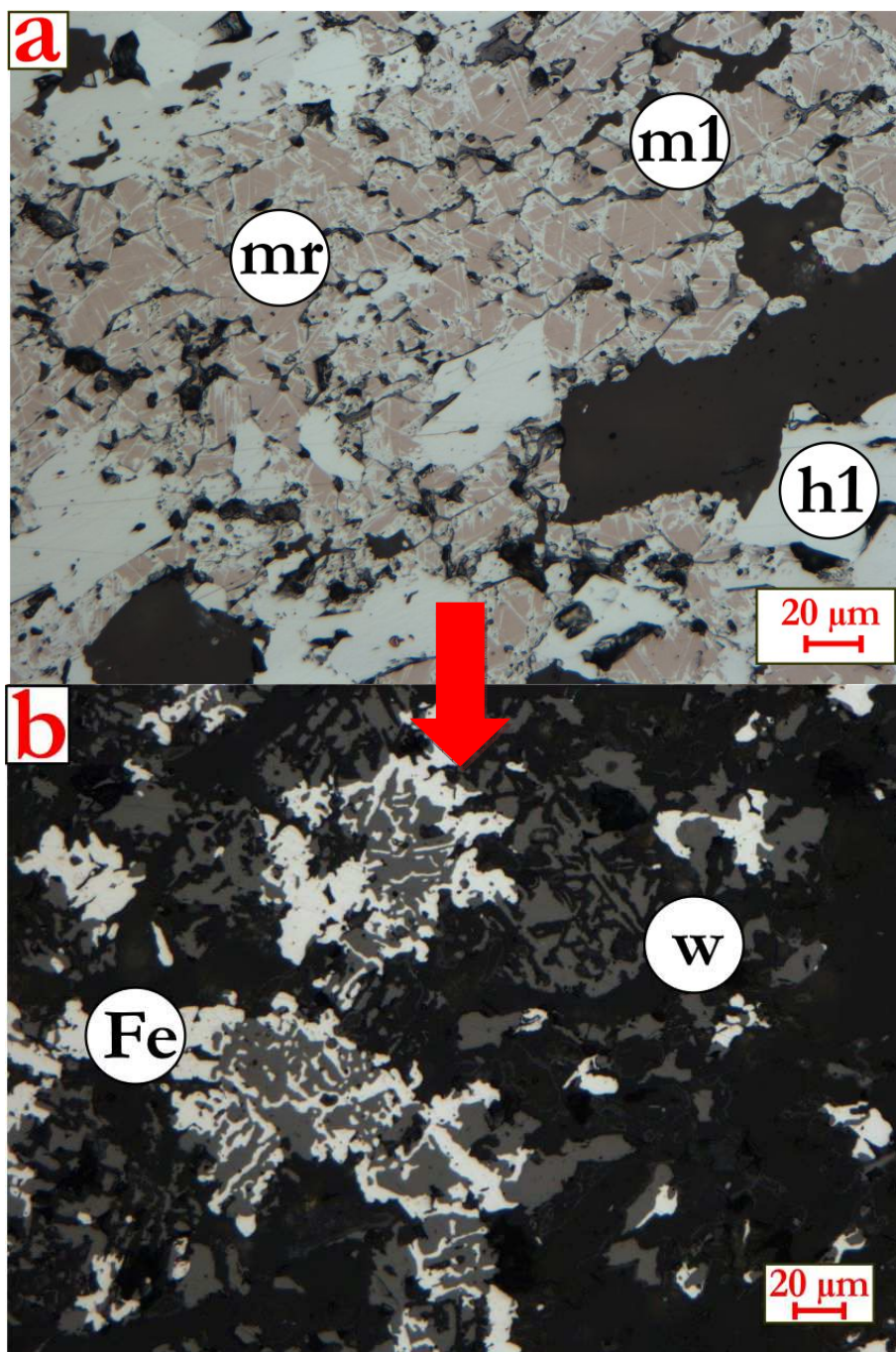
Figure 62: Medium to coarse trellis martite (mr) with magnetite (m1, brown) will be reduced to porous wuestite. The metallic iron is formed first in the former hematite lamellae.

Magnetite path

Dense primary magnetite (m1) will be reduced to dense wuestite (w) (Figure 63).
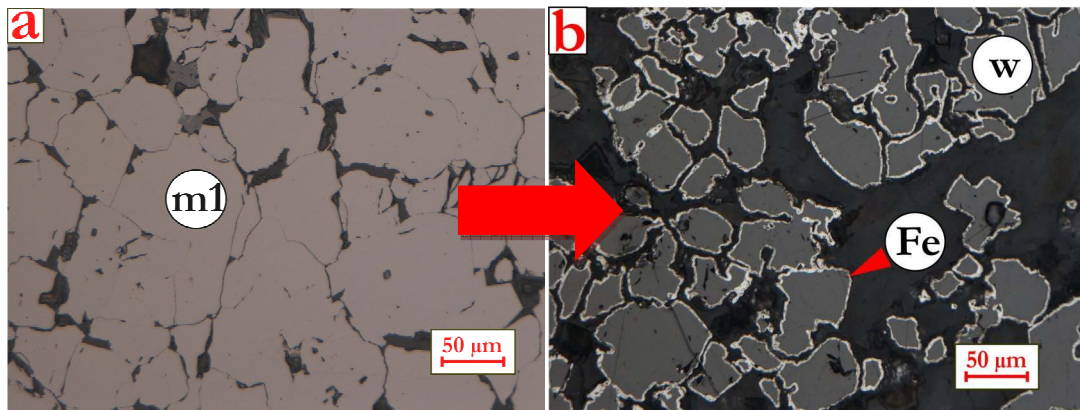
Figure 63: a) Dense coarse primary magnetite (m1). b) Dense wuestite (w) with Fe_{met} layers.

The evolution paths of hematite, martite and magnetite can be applied directly to other types of lumpy iron carriers like pellets and sinter. Pellets consist mainly of more or less rounded hematite. If a magnetite green pellet had not been well burned during the firing process, the core of the pellet consists still of magnetite. The reduction takes place in a more regular way, due to a higher porosity and more homogenous microstructure of pellets. After the transformation to wuestite the metallic iron starts to grow at the margin of the pellet as iron sparks and continues to iron layers (Figure 64, left). The reduction front moves further to core, whereas the margin is already completely reduced to metallic iron (Figure 64, right).
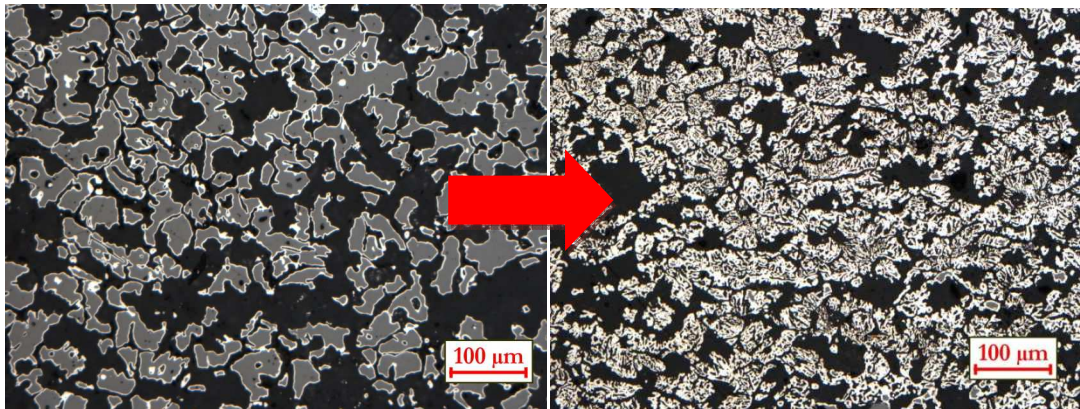
Figure 64: Images of a reduced pellet at the core (left) and the margin (right).

A magnetite core will slow down the reduction rate within the pellet significantly and leaves a wuestite core behind, unless a very long reduction time is applied (Figure 65).
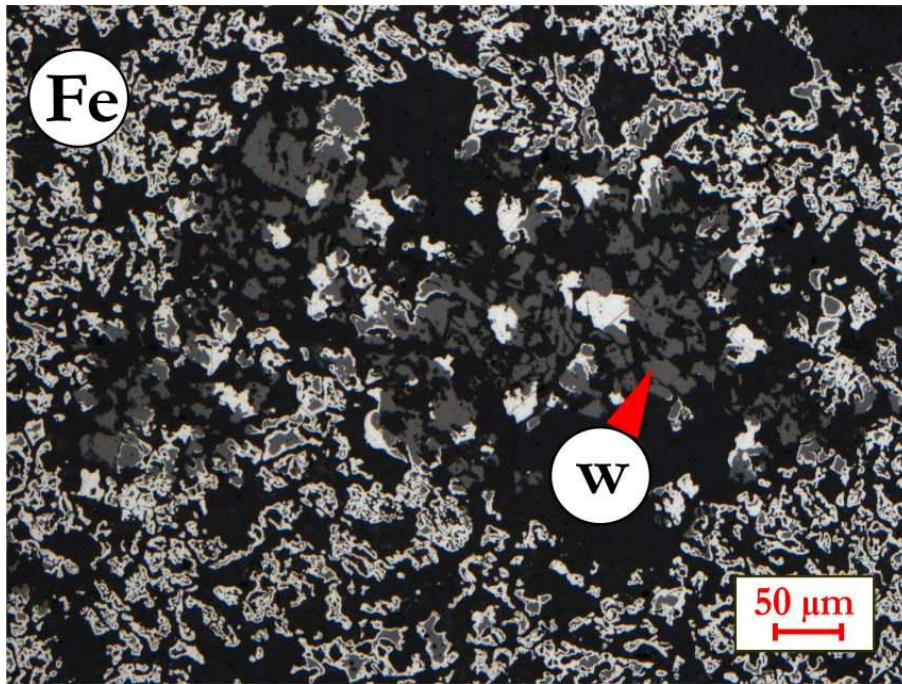
Figure 65: Former magnetite core of a poorly burned pellet is transformed to wuestite (w). The parent hematite is already transformed to metallic iron (Fe).

The description of the evolution of the reduction process of iron-bearing minerals in sinter was not in the focus of this thesis. Only one completely reduced sinter sample was analyzed (Figure 66, above). The intermediate steps of transformation of the minerals during reduction were not visible in the sections. On the basis of the shape and appearance of the metallic iron, some suggestions can be made:

- Magnetite is transformed to dense wuestite and further to porous metallic iron. A "thick" metallic iron layer is formed at the former magnetite crystal surface (Figure 66, below).

- Calcioferrite is reduced to fine metallic iron without a "thick" metallic iron layer, which indicates a quicker reduction (Figure 66, below).

- Tiny iron nuclei are visible within the glass phase of the reduced sinter (Figure 67).

The microscopical observations of the different lumpy iron carrier samples were considered for the development of the image processing software VisuMet. The evolution during the standard reduction tests was the basis for the development of the algorithm, which is described in the chapter 4.
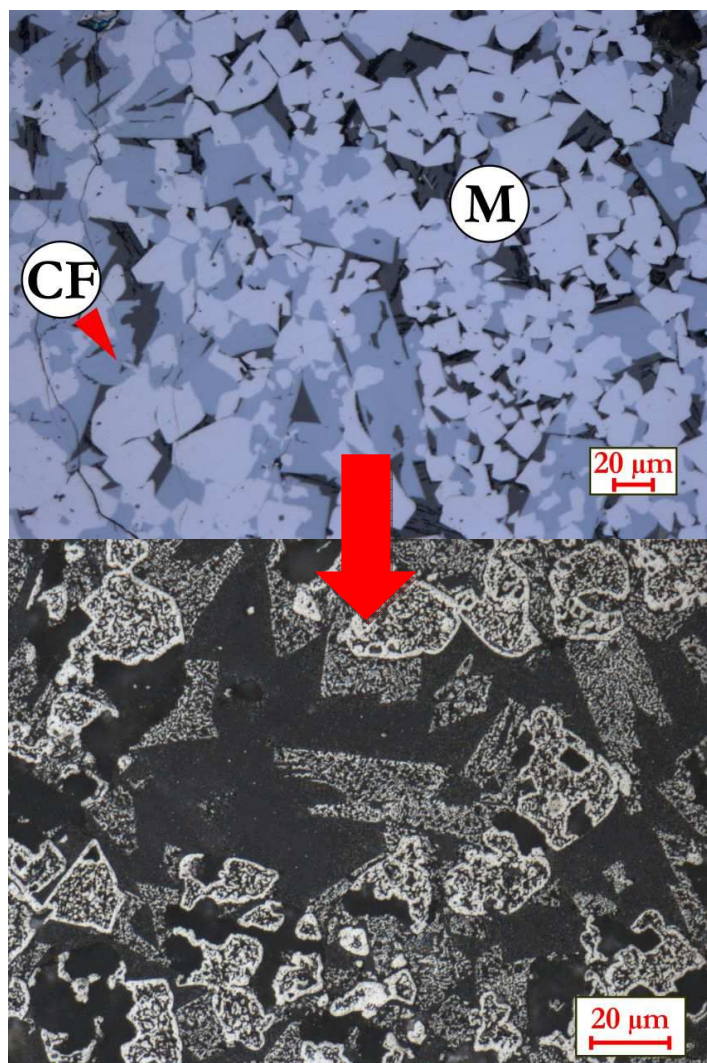
Figure 66: Reduction of sinter under ISO-4695 test conditions. The minerals are transformed to fine spongy metallic iron. The former crystal boundaries are still visible.
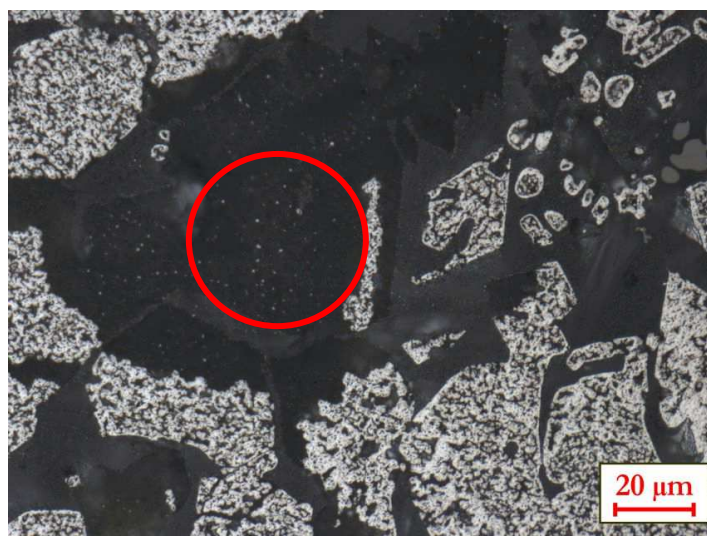
Figure 67: Tiny iron nuclei in the glass phase of a reduced sinter grain.

4.   Methodology

The manual classification and evaluation of iron ores, pellets and sinter by microscopic methods is a time-consuming method. Faster, more objective and reproducible results can be achieved by computer-based image processing. Microscopical observations on polished sections are the basis of a new methodology. The self-developed software VisuMet is the result. The prototype was developed by Heinrich Mali and Bernhard Spuida in 2008. The further development and application are described in this thesis.

4.1.   Optical image processing

Image processing is closely interconnected with stereology and morphology for the analysis of spatial structures. In this chapter, the principles and tools of morphological image analysis will be discussed to understand the different steps of the algorithms of VisuMet.

4.1.1. General

Computer-based image processing and analysis started in the late 1960's in relation to the moon missions. Stereology methods were used by geologists for measurements in 2D plane sections for solving practical problems, like mineral abundance or grain size distribution (Weibel 1979; 1989). Due to the enhancement of computer power the popularity of image processing has been rising since then. The typical steps of image analyses are:

- Image acquisition

- Image enhancement

- Image segmentation

- Image measurements

- Statistical analysis

During image acquisition, a digitization of a continuous object takes place with a suitable camera. Each point at the discrete network space of an image is attributed a numerical value. The raster points are evenly distributed, which is known as the dpi value (dots per inch) or resolution. These regular cells are called pixels. Image types are different in the type of numerical information associated with each pixel. So binary and grayscale images are mono-channel. They only store one value per pixel. On the other hand, a multichannel image can store a vector of scalar values such as red, green, and blue components of color images. In a binary image, a pixel has only the value 1 or 0. An 8-bit image (2^n) can either

save one value per pixel, but from 0 to 255 (256 in total), as for example a grayscale image. VisuMet uses the image type TIF. It is a 32-bit image type and obviously can store more numerical information, up to a size of 4 GB. It is normally used without any compression. The Axio Vision® software from Zeiss® is used as the image grabber. VisuMet loads the tif-images from disk for further processing.

Depending on the image quality or analyzing problem the images are enhanced by filtering. Image filters are neighborhood operators, in which any given pixel of the output image is determined by applying an algorithm to the values of the pixels in the neighborhood of the input pixel. It is possible to improve the sharpness of transitions (high pass filter) or remove insignificant details by smoothing the image (low-pass filter). A particle filter removes small undesired particles.

For image segmentation, the image is divided into different regions, each with certain properties. It connects a set of pixels to the associated region. Measurements and quantitative interpretation of image data can only be performed in segmented images. Thresholding of pixel values is a segmentation method. After thresholding, an image consists of a particle region and a background region. All pixels of the input image lying in a given interval are set to the value 1 and the remaining to the value 0. The result is a binary image. For color images, a minimum of three thresholds must be specified, one for each color. The color layers are called red, green and blue for the RGB-model and hue, saturation and luminance for the HSL-model.

After binarization, morphology operators are performed to improve the transition zones (between bright and dark areas), where misidentification can occur. This usage of the functions depends on the section quality and texture of the sample. The main functions used in VisuMet are:

- *Erosion* eliminates pixels isolated in the background and erodes the contour of particles according to the template defined by the structuring element. For all following examples the template is one pixel ▮ .
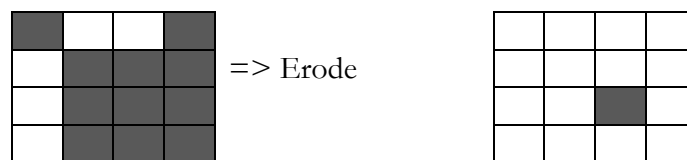
- *Dilation* eliminates tiny holes isolated in particles and expands the particle contours according to the template defined by the structuring element. It is the opposite operation to erosion.

- *Opening (Erode & Dilate)* is defined as an erosion followed by a dilation by the same structuring element. It is used for noise removal. It removes small objects from the edges of foreground pixels. It preserves foreground regions with similar shape of the structuring element.
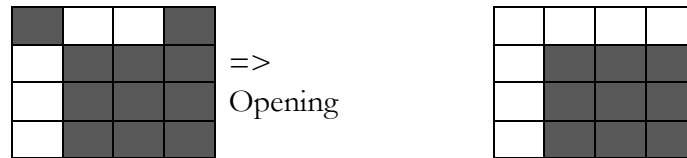
=> Opening

- *Closing (Dilate & Erode)* works reversely to opening. It tends to enlarge the edges of foreground pixels and shrink background holes. However, it is less destructive of the original boundary shape.

=> Closing
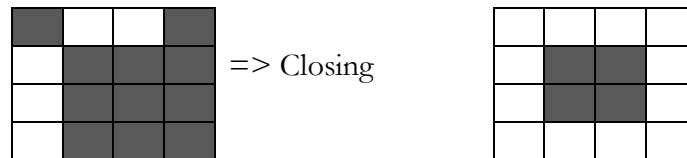
- *Fill holes* fills the holes found in a particle, but if the holes are in contact with the image border they are not filled.

=> Fill holes
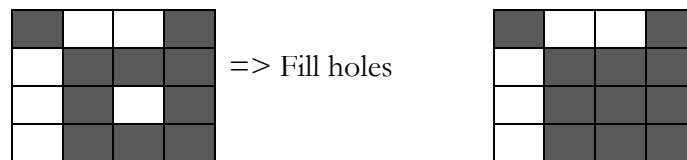
- *Remove border particles* function removes all particles, which touch the border of the image. The real size of such a particle cannot be determined.

=> Remove border particles
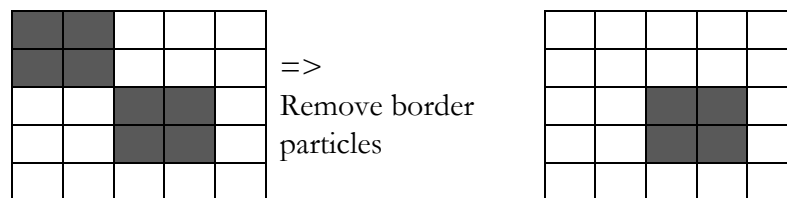
Boolean operations are applied to combine informations from several binary images. They are AND, OR, XOR and NOR (Figure 68).
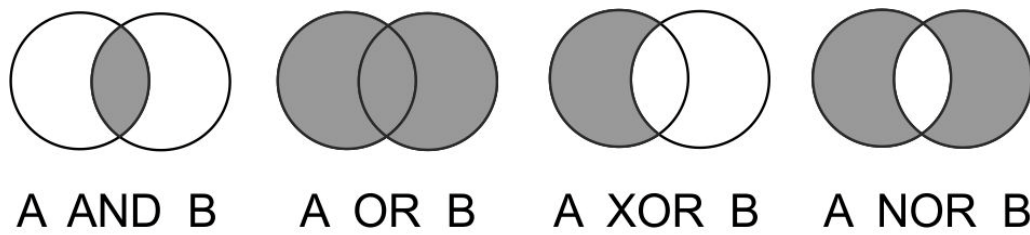
Figure 68: Schematic overview of the four Boolean operators.

After all these steps the image is ready for measurement and statistical analysis. The segmented particles can be measured according to their area, perimeter, diameter etc. Area is defined as the measure of a planar surface in 2D space. Area measurements are strong against translation and rotation of the grid pixels. However, dealing with squared units may be complicated and the diameter measurements are preferred. To compare areas by making any reference to the shape of the particle, it is convenient to convert any area into the diameter of a circle having the same area. Such a recalculation should be restricted to the analysis of a set of particles with similar shape (Francus 2005).

4.1.2. State of the art

Image analysis is probably one most helpful tool of recent years. It has attracted attention due to its further spread in different applications. In the evaluation of iron carriers, two main analysis systems have been established. These are the microscope-based optical image analysis (OIA) and the analysis by scanning electron microscopy (SEM) in combination with suitable image processing software. Both use polished sections of the sample material to determine the mineral abundance, porosity, mineral liberation or other characteristics.

In OIA the identification of the different phases is based on the variation of optical characteristics in polarized light like color, gray level or reflectivity (Sutherland and Gottlieb 1991; Lastra et al. 1998; Pirard and Lebichot 2004; Lane et al. 2008). In particular, a number of studies have focused on iron ore characterization with optical microscopy (Donskoi et al. 2007; Alvarez et al. 2008; Donskoi et al. 2008; Gomes, O. da F. M. et al. 2013; Donskoi et al. 2015). Most of the techniques are semi-automated and need an experienced operator to define the thresholds for classifying the phases. The OIA has several advantages. It is more cost effective and the differentiation of the iron oxides is better than with SEM-based systems.

The alternative approach is the use of SEM with EDS detector and an appropriate image processing software like the popular systems QEMSEM® or MLA® (Pirrie et al. 2004; Tonžetić and Dippenaar 2011; Hapugoda et al. 2016). All elements heavier than carbon can be identified, which is an advantage of these systems. The classification of minerals is based mostly on chemical composition compared to mineral standards. Difficulties arise when phases of similar chemistry have similar average atomic numbers. This occurs with hema-

tite/martite and magnetite. A suitable BSE calibration standard for magnetite and hematite is needed. Due to the atomic substitution of Mg or Ca for Fe in magnetite its reflectivity behavior changes and leads to an underestimation of magnetite (Lu 2015). So the standards of magnetite and hematite have to be as similar as possible to the analyzed minerals. Donskoi et al. (2013) concluded that "a combined approach using both techniques will provide the most detailed understanding of iron ore samples being characterized". Both techniques have their advantages and disadvantages and should be chosen to the specific type of requirements of the analyzing problem.

4.1.3. Errors in Image Processing

Like in other analytical techniques image analysis underlies errors. There are numerous steps that accumulate errors. Pixels build up the digital image, images themselves are parts of a polished section, polished sections are samples of grains and the grains are samples taken from a pile. The quality of the method depends on controlling and estimating the errors. There are three main groups of errors in image analysis (Francus 2005):

- *Preparation errors* affect the quality of representation of the particle during the image acquisition (saturation, exposure time).

- *Integration errors* are linked to errors during the digitization (magnification, resolution)

- *Analysis errors* are all biases during the segmentation and measurement steps (thresholding, diameter estimators, etc.)

The dispersion of the results in quantitative image analysis refers to two main reasons: deviation (heterogeneous material by nature) and error (lack of reproducibility). The deviation cannot be reduced, but the errors can be kept at the lowest possible level (Francus 2005). The aim is to be sensitive for the cumulative error and keep the errors reasonable.

Preparation errors can be minimized by selecting a suitable camera and improving the conditions of image acquisition. So, choosing the right exposure time, white balance or filters and keep them constant will be first and essential step. The next serious step is choosing the right magnification, which influences the resolution of the image and is essential for the phase estimation. The distribution of the grain sizes of the particles is used for the estimation of the suitable magnification. Francus (2005) suggests that "particles should be at least >150 pixels in surface in order to estimate their aspect ratio without bias". Thresholding is an operator dependent factor in image analysis and interferes to the analysis errors. The phase percentage will be more affected than the median of an equivalent diameter. This fact should be considered, therefore automated thresholding function is preferable. All these facts can reduce the errors to a minimum for reliable and reproducible results. In addition, external methods should validate the results of the image analysis.

VisuMet minimizes the preparation and integration errors by keeping the saturation, exposure time, resolution and magnification always the same for a sample. The analysis errors are kept to a minimum by using a combination of manual and automated thresholding functions. In addition, the equivalent pore diameter is only measured in particles with an area larger than 150 pixels. The validation of VisuMet was made by point counting six different polished sections and comparing the results to the VisuMet analyses (see chapter 6).

4.2.   Experimental Setup

The preparation of sections is important. Only a perfect planar polished section will prevent misclassification of mineral particles. The iron carriers are prepared differently and are described as follows:

Sample preparation: Iron ores and pellets

The preparation was made at the Chair of Geology and Economic Geology (MUL). The number of sections varied from 2 up to 4, depending on the grain size. Pellets were cut into quarters and iron ore grains were cut in half. The grain size of the pellet and iron ore material before cutting was between 10-12.5 mm. Up to fourteen grains per section were taken. After embedding in resin, the sections go through several grinding and polishing steps. This leads to an even suitable surface without scratches, holes or any other defects. Otherwise it will affect the image analysis. A summary of the used products for preparation is listed in Table 6.

Table 6: List of used preparation products.

Name	Description	Usage
Araldit F	Resin	Section
Araldit HY905	Hardener	Section
Isopropyl		Cleaning
ATM	Diamond grinding suspension	Water free polishing

Sample preparation: Sinter

Although the polishing process was alcohol-based, etching and dissolution of certain minerals like Ca-Ferrites took place. Therefore, a special preparation routine for sinter samples was developed. The preparation is carried out using an ATM Saphir 520 (Figure 69) and is water-free with a special polishing lubricant. The cleaning of the sections is made with isopropyl (> 99.95 % purity). The sample is embedded in a two-component resin at a ratio of one to one (Araldit F & Araldin HY905). The resin has to be hardened at 120 °C for 48

hours under an extraction fan because toxic fumes are released. Figure 70 is a summary of the individual grinding and polishing steps.

Figure 69: The ATM Saphir 520 polishing machine.

The section surface is ground first using a 74 μm diamond grinding disk with addition of an alcohol-based lubricant (ATM) until the sinter grains are exposed sufficiently at the specimen surface. The properties for the grinding and polishing machine are 150 Newton pressing force with 150 rotations per minute in counter rotation.

Next grinding step is the 40 μm diamond grinding disk with lubricant until the section is even and with a dull shiny surface (about 30 min). Now the polishing part starts with the polishing chemical cloth from ATM called "Alpha". A nine μm silicon carbide powder with lubricant is used on the cloth, too. The settings are 100 Newton with 150 rpm for 30 minutes. Afterward, the section should be slightly reflecting, and few scratches should be remaining. Now the polishing cloth is changed to 3 μm and the polishing suspension is a mixture of 3 μm Al_2O_3-powder with lubricant. This step lasts for about an hour with a quality check after 30 minutes. The settings are 100 Newton pressure and 150 rpm for the machine. Under the microscope, the iron oxides look reasonably polished already. The glass phase is even and some breakouts can be still there. If the breakouts are big or the surface is highly porous, re-resinating should be considered.
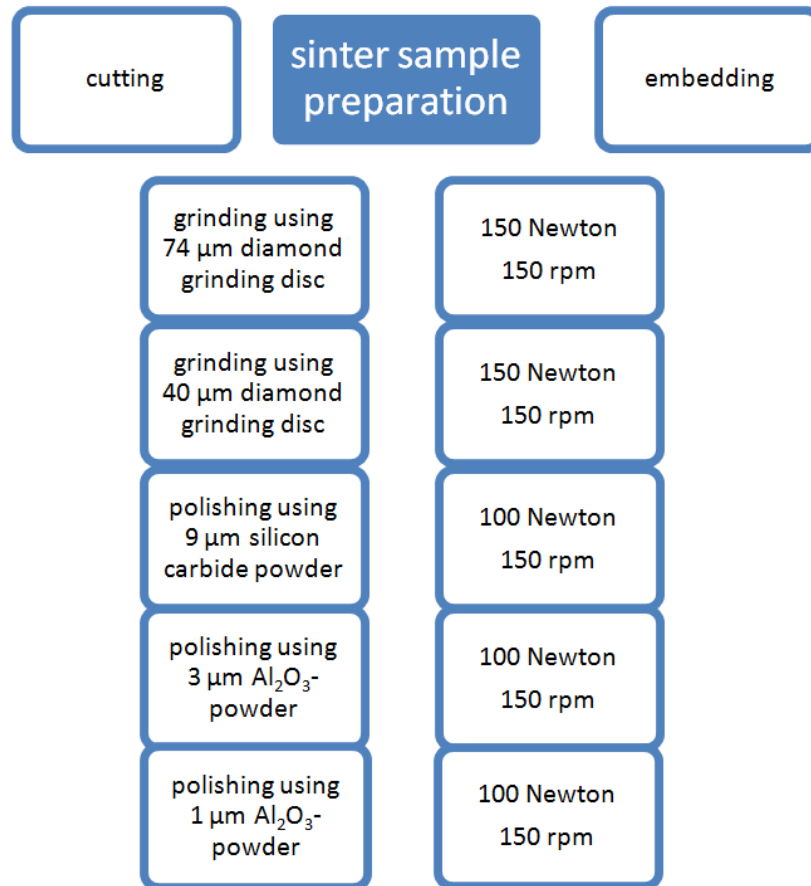
Figure 70: Flow-sheet of the grinding and polishing steps of the sinter sample preparation.

The next step lasts for about an hour with a control of the section after 30 minutes. The polishing material is a 1 μm cloth with a polishing suspension of lubricant and 1 μm Al_2O_3-powder. The final sections should have a mirror-like reflecting surface. The crystal and grain borders should have no local relief. The cleaning is made with isopropyl and an ultrasonic device. For storage, a desiccator is used due to the hydroscopic nature of some minerals.

4.3.   VisuMet

The images are taken with a Zeiss Axio Observer Z1m and the Axio Vision Software. The Axio Observer Z1m is a reversed microscope with an automated table. The properties like exposure time, white balance etc. are held constant during a sample series. The definition of the image is managed by the built-in auto focus. The pictures have a size of 4164x3120 pixels and a resolution of 150 dpi. The image width is 0.0354 mm at a magnification of 250. It is saved as a tiff file with a size of 38 Mb without any compression. The positions for image taking are chosen randomly and 500 to 1000 pictures are taken for each polished section. For pellets and sinter samples the total number varies from 500 to 750 pictures.

The total number of images per sample is sufficient, so that the cumulative value of the segmented phases does not change significantly by processing an additional picture.

VisuMet is programmed in LabVIEW® from National Instruments. The programming design software is graphically and incorporates the NI Vision Development platform. This module includes a library with several scientific imaging and machine vision functions for customizing applications. It is based on a sequence structure, where the program steps contain one or more subroutines, which will execute in sequential order. The simplified software flow sheet is charted in Figure 71. LabVIEW® is not a code-based programming language, it consists of bricks (modules), which are combined to a sequence (algorithm).
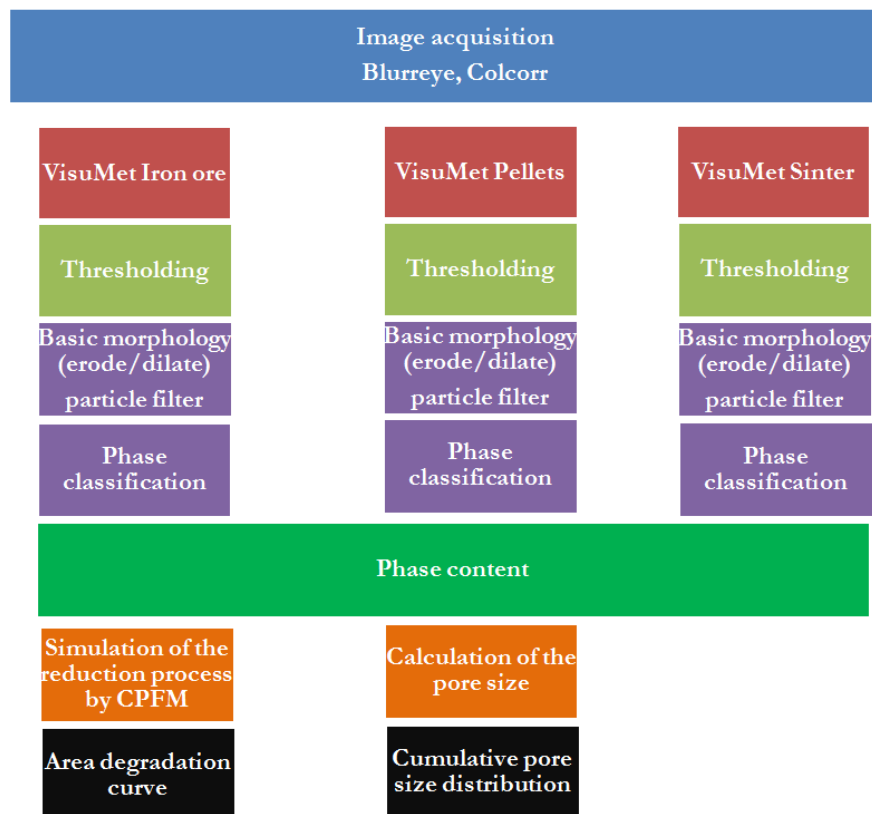
Figure 71: Simplified VisuMet flow sheet.

The quality of the images is checked with a self-programmed tool called Blurreye. It is an edge detection program with a differentiation filter. The filter produces continuous contours by highlighting each pixel where an intensity variation occurs between itself and its neighbors (Figure 72). Every image is divided into four rectangles. After filtering the tool calculates the histogram for each rectangle and returns the mean value of the highlighted pixels. The higher the mean value, the better is the definition of an image.
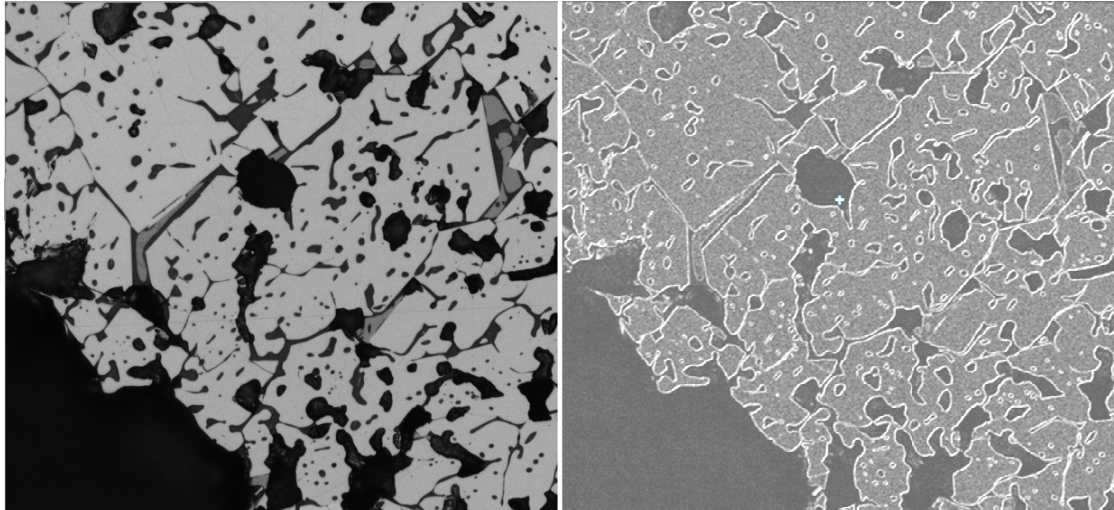
Figure 72: Example images for the edge detection (before and after).

A box plot symbolizes the distribution of the mean values and the drop out value is chosen (Figure 73). The tool sorts out black images, partly focused images (one rectangle with low mean value) and totally blurred ones.
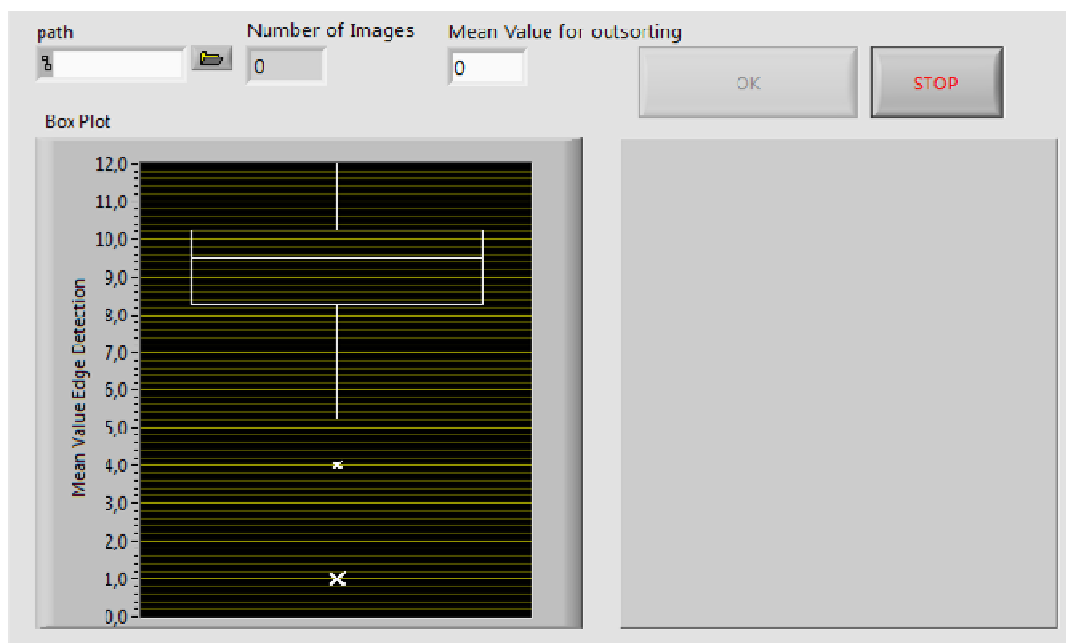
Figure 73: Front panel of the tool Blurreye with the box plot.

At the contact between different minerals, color fringes occur (Figure 74). This effect depends on the digital camera. With the tool 'Colcorr' (programmed by DI Louis Hohl) the fringes are minimized. The tool works with a low-pass filter and by moving each color layer for a certain level.
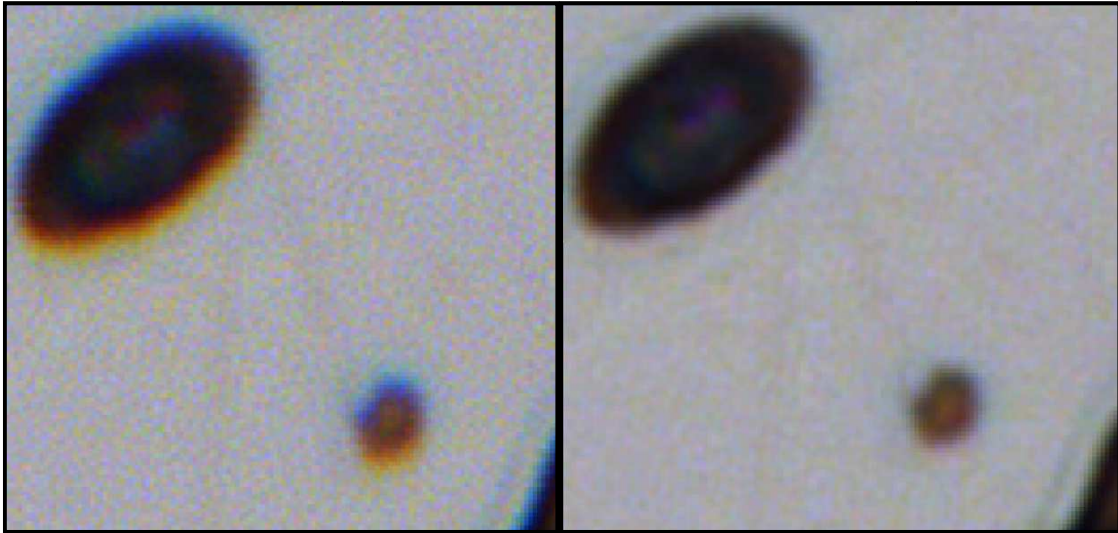
Figure 74: Example image for color fringes between dark and bright areas and the image after shifting the color layers using the program Colcorr.

VisuMet starts with Blurreye and Colcorr. Depending on the sample type (iron ore, pellet or sinter) the phases in the images will be classified by thresholding. The thresholding with six values works for lumpy and fine iron ores. The six values are taken from the red-green-blue plane and hue-saturation-luminance-plane of the pixels. Thus, limonite, hematite, and magnetite are segmented. Table 7 shows the thresholding variants for the different samples and which phases are being identified. For pellet samples, the user has to change first the BCG values (brightness, contrast, and gamma) of the image for glass and pore determination.

Table 7: Overview of the thresholding parameters for the identification of the phases and pores of different iron ore carriers.

Target	Threshold values	Phases
Iron ore	RGB, HSL	limonite, hematite, magnetite
Pellet	BCG, low and high value	Fe-oxide (hematite, magnetite), glass, pore
Sinter	BCG, low and high value Grayscale	hematite, magnetite, Ca-ferrite, Si-ferrite/glass, pore

For glass analyses in pellets only the red color plane is changed because the difference between glass and resin-filled pore is significant. After that hematite and magnetite are identified automatically and are summarized to Fe-oxide. It is possible to discriminate between hematite and magnetite but, for further evaluation, it is not necessary. The image processing of sinter images works with the different reflectivity of the phases. For every phase, the BCG values are modified, and the different thresholding processes included in the LabVIEW® software produce a binary image for each phase.

There are subroutines integrated into VisuMet for finding the appropriate threshold values. These tools are self-programmed as a state machine. Each state can lead to one or multiple sub-states and can end the process flow. A state machine relies on user input or in-state calculation which leads to the following processing step. It starts with the default or initial state and ends with the shutdown state, where the thresholds will be saved to *.txt-file. Depending on the kind of sample the user finds the right threshold values by trial and error. The settings are changed on the monitor simultaneously. Figure 75 shows the user interface of the tool and an example of iron ore thresholding. With the bars, the value ranges are set for RGB and HSL. The binary image for each mineral is displayed as well as the compilation of all binary images to control. The same tool is available for pellets and sinter, where the user can find the suitable preferences for the BCG values.
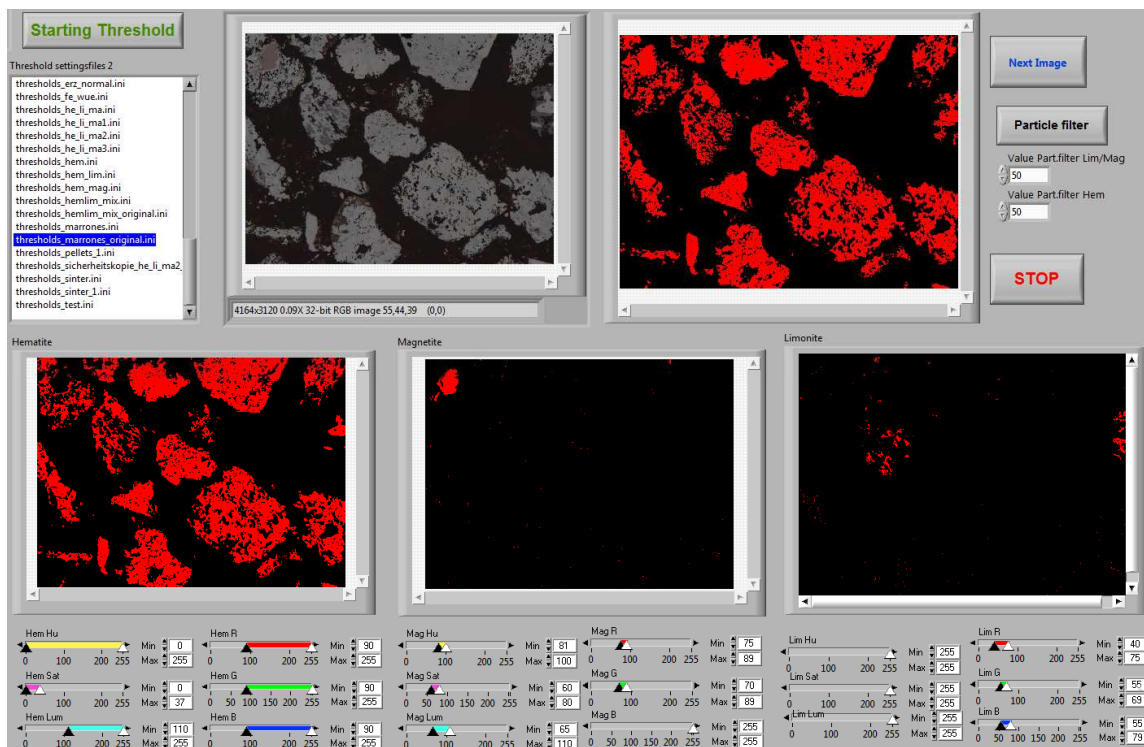
Figure 75: Tool for setting the thresholds for iron ore images (steady state machine).

After thresholding, basic morphology tools (erode, dilate, etc.) eliminate artefacts from incorrectly classified particles. They can be adjusted for every image's series. A particle filter removes particles with an area below 150 pixels (<2 μm in diameter). Now the binary image for each phase is ready for measuring the area and calculating the content of the individual components.

4.3.1. VisuMet Iron Ore

The reduction (phase transformation) of a mineral starts at the crystal and grain border and proceeds into the center. This is described as the shrinking core model (see chapter 2.3).

Every investigated iron mineral has different reducibility. The general path from iron oxides to metallic iron includes the simplified stages: limonite – hematite – magnetite – wuestite – Fe_{met} ($\pm Fe_3C$), depending on the "start" mineral and reduction conditions (temperature and gas composition).

With a function included in LabVIEW® a distance map is created, where a pixel value of a particle is encoded as a function of the location of that pixel in relation to the distance to the border of the particle. This is based on the algorithms of Danielsson (1980). Every particle is split into concentric shells with a width of 1 pixel (Figure 76) in a different color.
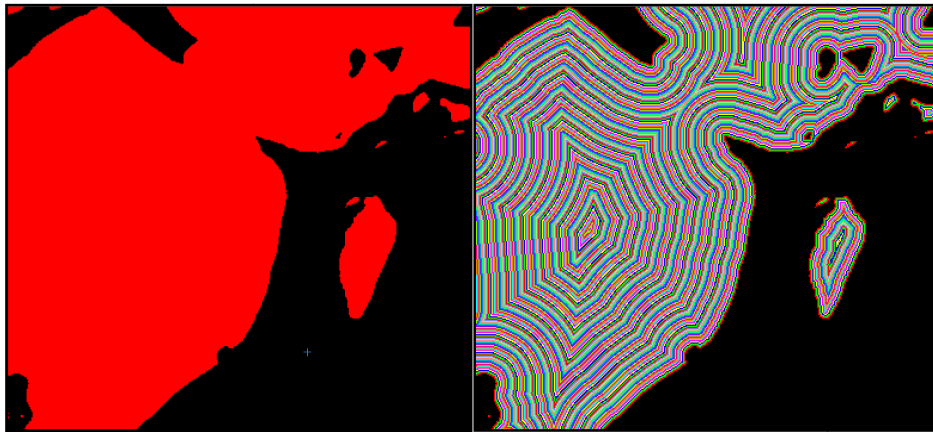
Figure 76: Example of a particle in the binary image (left) and the particle after Danielsson distance mapping with concentric shells (right) of one-pixel thickness.

Due to the different reducibility of the minerals, a distinct number of shells will be removed step by step. A step is defined as one loop pass in the algorithm. The reducibility of synthetic mineral components was reported from Wyderko-Delekta and Bolewski (1995). The parameters of the reduction process were 900 °C, 40 min and the atmosphere was pure CO.

Table 8: Reducibility of synthetic mineral components after Wyderko-Delekta and Bolewski (1995)

Mineral	Reducibility [%]
Hematite	49.4
Magnetite	25.5

The ratio of the reducibility is 1:2, so hematite is reduced two times faster than magnetite. Limonite is reduced much faster than hematite, so more shells per step are removed (Figure 77). The ratio for the shells is 1:2:5 for the minerals magnetite, hematite and limonite. The ratio is based on the tests of Wyderko-Delekta and Bolewski (1995) and observations of reduced iron ore sample under ISO-4695 conditions. After each step, the remaining area is measured and the cumulative removed area (percentage) versus steps is displayed

in a diagram (see chapter 5.2, Figure 83). These removing steps simulate the reduction front movement through the particle.
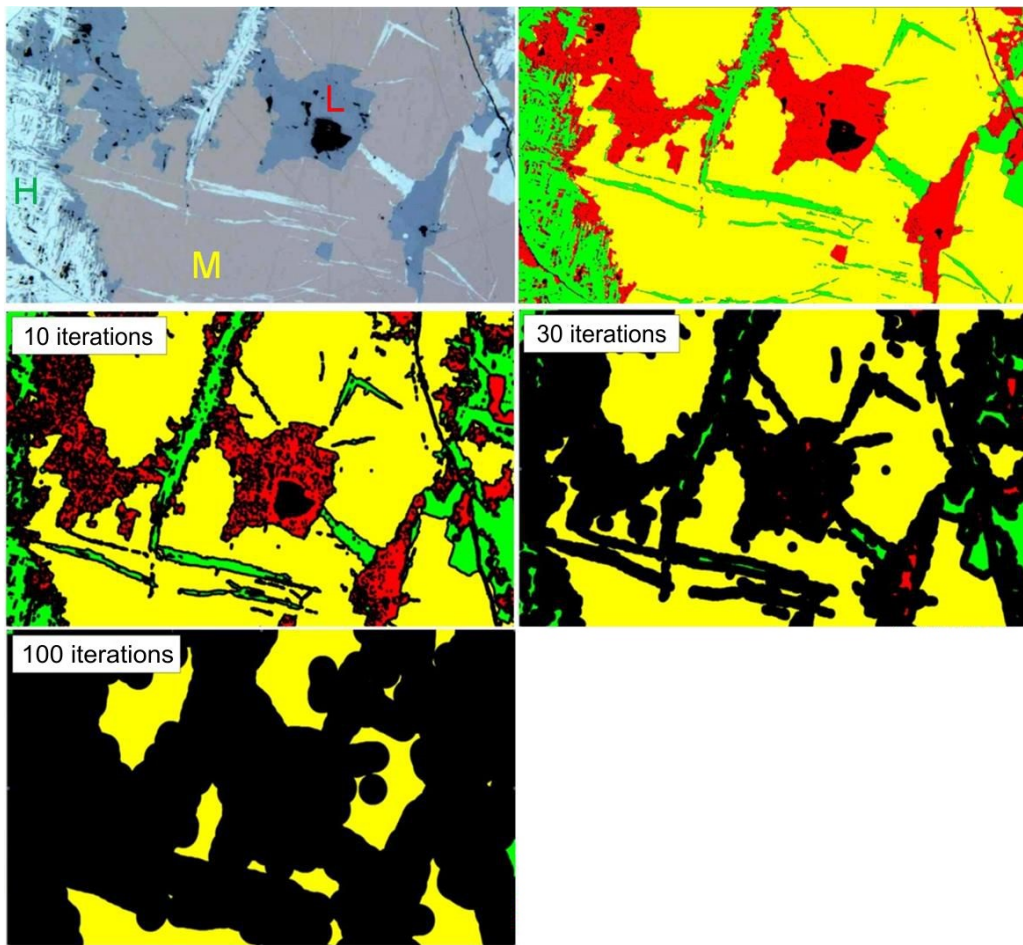
Figure 77: Example of the CPFM model, magnetite (yellow), limonite (red), hematite (green), modified after Mali and Spuida (2013).

After the evaluation of the sample, a report (*.doc/pdf) and a *.csv-file are automatically generated with all parameters, settings, and results.

4.3.2. VisuMet Pellet

Simulations with pellet samples showed that the CPFM-evaluation and the crystal size of iron oxides do not correlate with the reduction behavior of different pellet brands. By checking petrographic and geometrical parameters of pellets, it turned out that only the pore size distribution coincides well with the ISO-4695 test results. Thus, the area of each pore is measured in micro images. This area will be equaled to a circle with the same area and the equivalent diameter is calculated. The cumulative distribution is displayed in a diagram with the equivalent diameter to the sum distribution Q(x) (Figure 78). Pores with an equivalent diameter lower than < 2 µm were excluded from the statistical analyses.
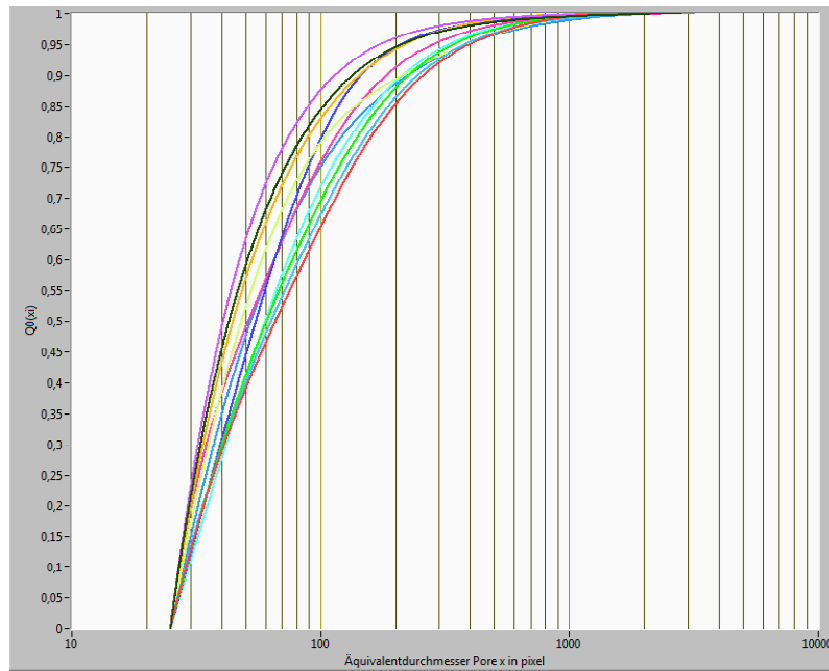
Figure 78: Example of the cumulative distribution diagram for the equivalent pore diameter of different pellet brands.

For further information, a homogeneity evaluation of the equivalent pore diameter is done with the homogeneity quantification method after Rossi et al. (2014) for microstructures. The method is based on the Gini index (G), which is defined mathematically out of the Lorenz curve (Gastwirth 1972). The Gini index measures a statistical dispersion of data (Figure 79). The partial homogeneity (H) is defined as $H_{(y)} = 1 - G_{(y)}$ of an attribute y.
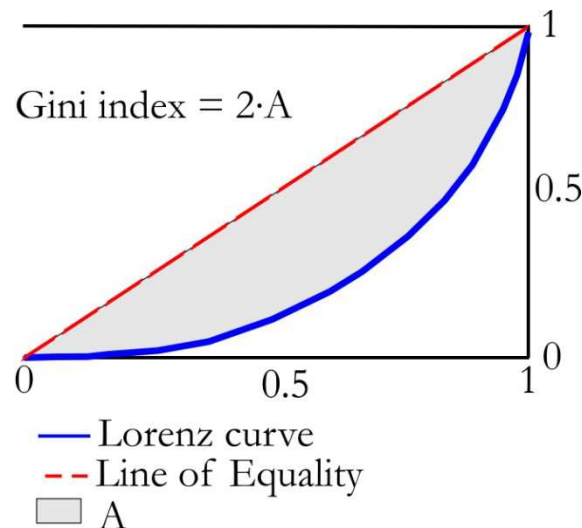
Figure 79: Simplified illustration of the Gini index. The Line of Equality represents the even distribution of two attributes.

The homogeneity can obtain values between 1 and 100 %. A high value of the homogeneity represents, how similar the values of a given attribute are. Here the equivalent pore di-

ameter is chosen as attribute. The median value of the equivalent pore diameters and the homogeneity (H(Ø) in %) are calculated automatically in VisuMet.

4.3.3. VisuMet Sinter

The first step for the evaluation is done by programming the sinter classification for mineral phases, glass, and pores. The minerals hematite, magnetite, Ca-ferrite as well as glass and pores are classified due to their color and the abundance is calculated. The glass phase includes Silicio-ferrite, because the reflectance is similar, and the Silicio-ferrites are usually below a crystal size of < 5 μm. In addition, a neighbor to neighbor evaluation is done, where the preferred mineral neighbors are being identified.

The algorithm for the neighbor to neighbor evaluation is based on the binary phase identification. Every phase receives a different color/value (black, red, green, blue, yellow; 0-4). The first phase is dilated by one pixel, which leaves behind a black one-pixel rim around the first phase. The rim gets the value of the first phase +1 and the value of the first phase is reduced by one. This is done for all other phases too. In Figure 80 hematite (yellow) has the value 3 and so the 'one-pixel' border zone between pore and hematite has the value 4 (blue). The blue pixels are measured and can be converted in mm or as a ratio. This presents phases preferentially in contact with each other or situated at the sinter/pore surface.
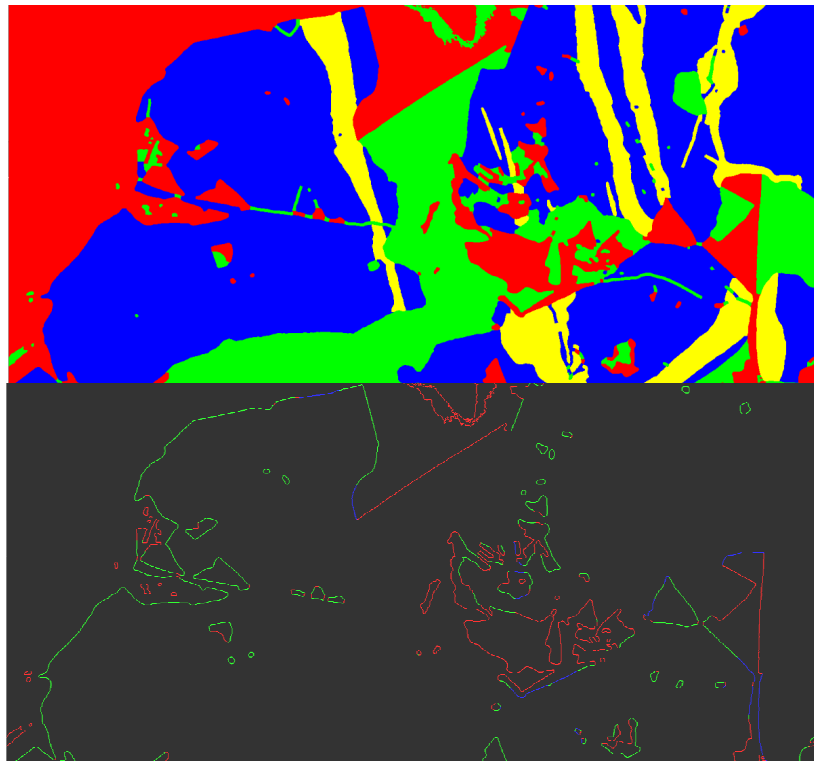
Figure 80: Neighbor to neighbor evaluation, above different phases and below the 'one-pixel' border zone in different colors for the different phases in contact. Here the contact of the red phase (pores) to the others are visualized.

5.   Results of VisuMet

The VisuMet results were obtained by processing up to 1000 micro images of polished sections of different iron ore carriers. The detailed algorithms are described in chapters 4.3.1 and 4.3.2. The algorithms are based on the microscopical examinations of the raw material before and after the ISO-4695 test. The mineral type and morphological attributes are combined to predict the reduction behavior. In total 20 different iron carrier samples (iron ores, pellets, sinter) were analyzed and the results are described in the following sections. The quantification of the mineral phases and pores were validated by the point counting method.

5.1.   Comparison of VisuMet to Point counting

It is common practice to determine the mineral abundance by point counting (Chayes 1956). This statistical method is based on identifying phases (minerals, pore, etc.) at the crossing points of a grid. The grid size depends on the crystal size. In general, more than 1000 points are counted per section. The number of points depends on the homogeneity of the mineral distribution.

For the reliability check of VisuMet, a comparison of manual point counting and VisuMet was done. For each kind of lumpy iron carrier, two sections were selected. A grid containing five vertical and four horizontal lines at a magnification of 25 was chosen to select the positions for image acquisition (Figure 81, left). Afterward, point counting was performed with the equal grid by a magnification of 250 (Figure 81, right).
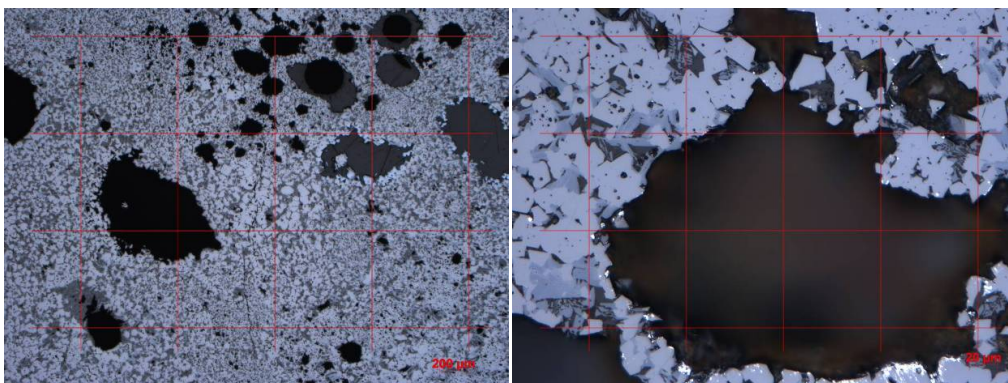
Figure 81: Point counting of a sinter section, (left) getting the positions at 25x magnification; (right) grid points for counting at 250x magnification.

120 images (6 different positions) were taken and in total 2400 points were counted per sample. Each image covers an area of 0.096 mm². The detailed data are shown Annex 1. The correlation coefficient R² of the mineral percentage values of the images resulting from

the point counting and VisuMet was 0.9967 (Figure 82). These comparisons thus exhibited positive cross-correlation.
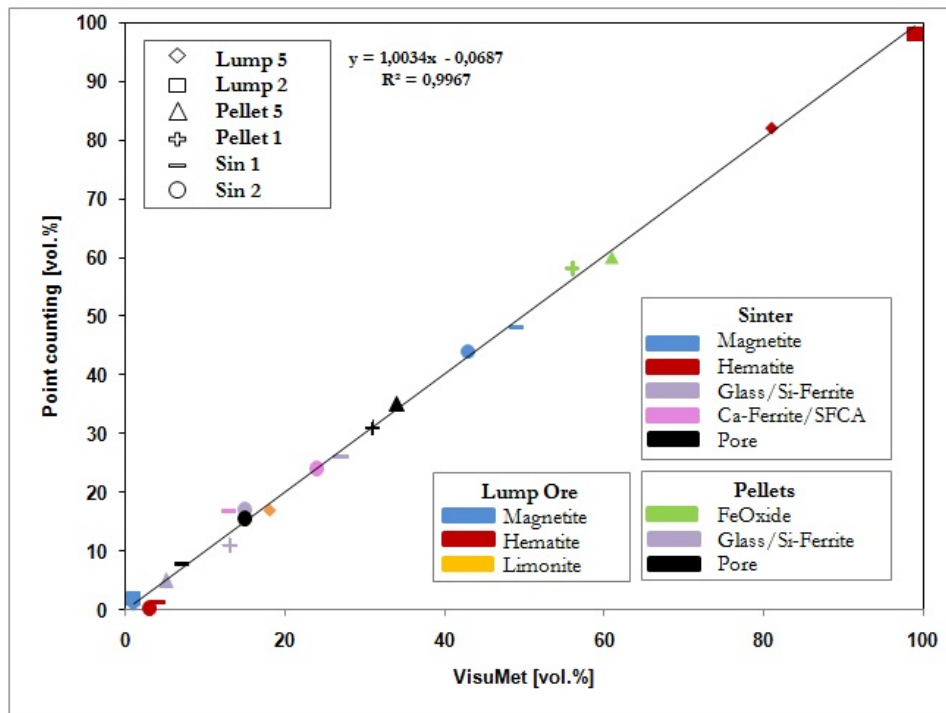
Figure 82: The cross-correlation graph of phase volume percentages by using point counting and image processing by VisuMet.

5.2. Iron Ores

First the ore type characterization was made under the microscope for every polished section of a sample. The ore types were summarized, and the reducibility was estimated optically. In total 5545 images were analyzed, on average 616 images per sample, but not less than 500. The mineral content was calculated by summarizing the areas of the classified ore particles after binarisation by thresholding. The area percentage is equal to volume percentage. This is based on the assumption that a sufficient number of images is taken into account, which contain almost all possible interfaces of the constituents. It is a common way to calculate the volume of an irregular object by summarizing an infinite number of infinitesimal pieces to compute the total. Three minerals were classified by their color: limonite, hematite and magnetite. In all samples the limonite content varies between 0 and 59 vol.%, whereas the hematite content ranges between 3 and 100 vol.%. The magnetite content is low (<2 vol.%), except sample KI, where it is 97 vol.%. The mineral contents of the lump ore samples are given in Table 9. The optical classifications are summarized from chapter 3.2.

Table 9: Mineral content [vol.%] of the investigated lump ores and the number of steps required to remove a certain percentage of the iron oxide particle area, calculated by VisuMet.

Sample	Lim	Hem	Mag	Reducibility optically	Steps [30 %]	Steps [60 %]	Steps [70 %]	Steps [80 %]
MN	5	95	0	+	3	7	10	13
KI	0	3	97	-	14	44	59	81
SI	0	100	0	+/-	6	14	17	23
AC	0	100	0	+	5	10	13	16
NA	3	97	0	+	3	7	10	13
CL	46	54	0	+	2	6	8	12
HA	0	98	2	+/-	6	15	19	25
SA	59	40	1	+	2	6	8	12
CI	0	99	1	+/-	8	19	26	35

+…good   +/-…moderate   -…bad

The VisuMet algorithm for iron ores is based on the shrinking core model. The concept was realized by simulating the reduction from outside by generating shells. These shells are removed at every loop run in a specific ratio, depending on the mineral type. The area of the ore particle before and after shell removing is measured. The difference of both values is cumulated for each removing step, which can be displayed as area degradation curve. The curves of the iron ore samples are displayed in Figure 83.

Due to the cumulative curves, the lump ores can be divided into three groups. The particular values for the amount of steps required for removing specific area segments are given in Table 9. First group are lump ores (SA, CL, MN, NA) with a certain amount of limonite (3-59 vol.%). This group needs less than 13 steps to remove 80 % of the particle area. The curves become only flatter after 90 % removed area. Forty to sixty steps are necessary to completely remove all ore particles.
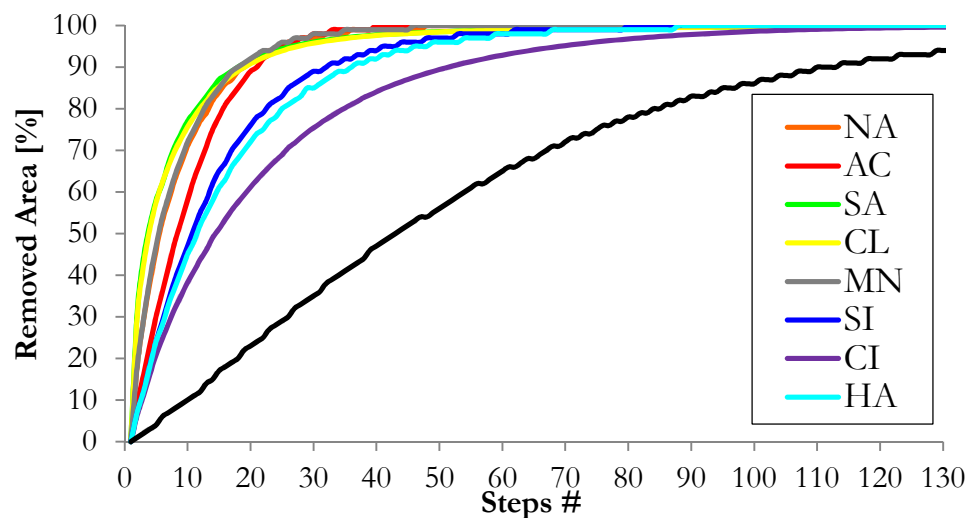
Figure 83: Results of the VisuMet analyses of the investigated lump ores.

The second group consists of lump ores with more than 95 vol.% of hematite in different forms (AC, HA, CI, SI). The grain size of the hematite varies from so-called microplaty (<5µm) to dense >>50 µm grains. Group 2 requires 16 to 35 steps to remove 80 % of the particle area of the iron oxides. AC is the only sample, which needs less than 20 steps for removing 80 %. Furthermore, the curve of AC flattens out later (>90 % removed area) than the curves of SI and HA (>80 % removed area). CI has the lowest gradient of this group and the curve becomes flatter before 70 % of the ore particle area are removed. Between 40 and 120 steps are necessary to completely remove all ore particles of this group. The last lump ore (KI) represents iron ores with high magnetite content. KI needs 81 steps to reach 80 % removed area. This is on average four times more than the others. The curve of KI has the lowest gradient of all samples.

5.3.   Pellets

Nine pellet brands have been analyzed by microscope and image processing (Table 10). In difference to the lump iron ore, hematite and magnetite are cumulated to Fe-oxide. Limonite is not present, due to the production conditions of pellets. However, a slag phase is generated during firing. In total 5186 images were analyzed for the determination of the mineral content, leading in average to 576 images per sample. Sections of RR9 and AL2 are shown separately to demonstrate the variation between sections of the same sample. The maximum difference is 4 vol.% in the Fe-oxide and porosity values of the AL2 sections. The mineral content varies only 1 vol.% at the RR9 sections.

Table 10: Phase and pore content of the pellet samples, as well as the median of the equivalent pore diameter and the homogeneity.

Sample	Pore [vol.%]	Glass [vol.%]	Fe Oxide [vol.%]	Median p ø [µm]	H(ø) [%]
RR9_1	48	14	38	3.4	57
RR9_2	47	14	39	3.8	55
PO8	38	9	53	3.6	52
CV7	31	13	56	4	45
MP3	38	5	57	4.3	50
KP6	36	5	59	4.3	49
TU5	34	5	61	4.3	44
TA4	27	6	67	4.6	58
AL2_1	32	10	58	5.4	50
AL2_2	36	10	54	5.4	48
BR1	31	13	56	5.5	49

The Fe-oxide content is over 50 vol.% in all pellet brands. The exception is the sample RR9, where the cumulative Fe-oxide content is below 40 vol. %. The glass content is below 15 vol.% in all samples. The porosity differs largely between 25 and 45 vol.%. The highest porosity was found in the sample RR9. The cumulative values are illustrated as a ternary diagram in Figure 84.
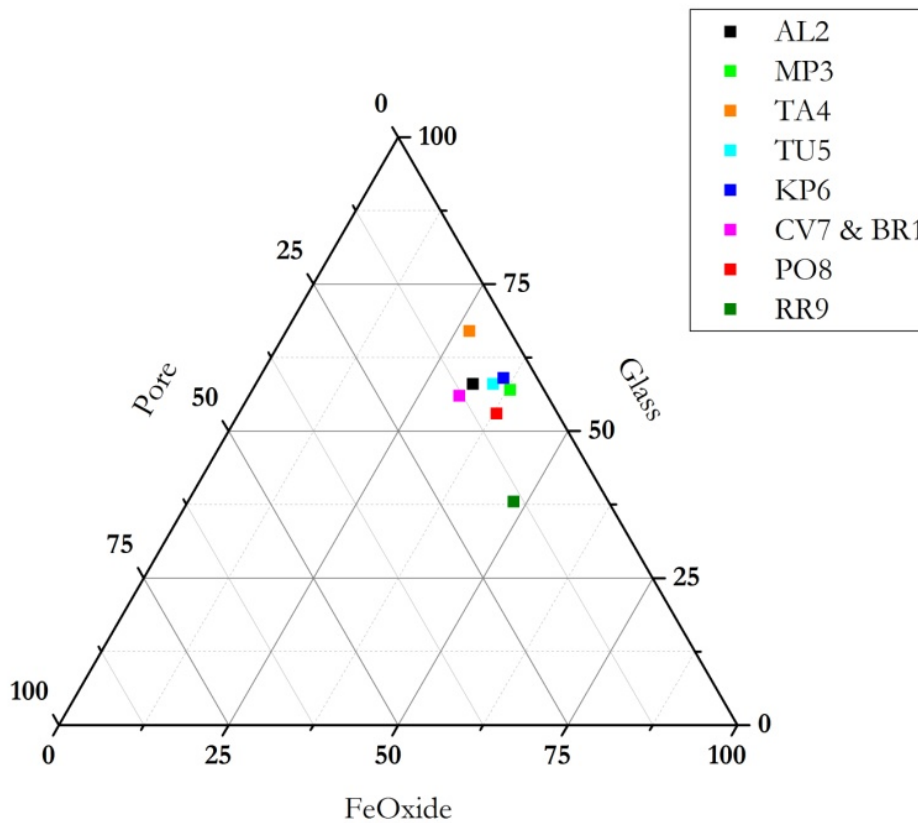
Figure 84: Ternary diagram of the cumulative constituents of the pellet samples.

In contrast, Figure 85 visualizes the variation of the phase content of every image of a sample. Most of the images plot in narrow band, where the Fe-oxide content is inversely correlated to the glass content. The porosity has a lower variation within a sample. The Fe-oxide content varies between 25-70 % for all images. The glass comprises up to 50 %. The porosity values range from 25 % to 48 %.
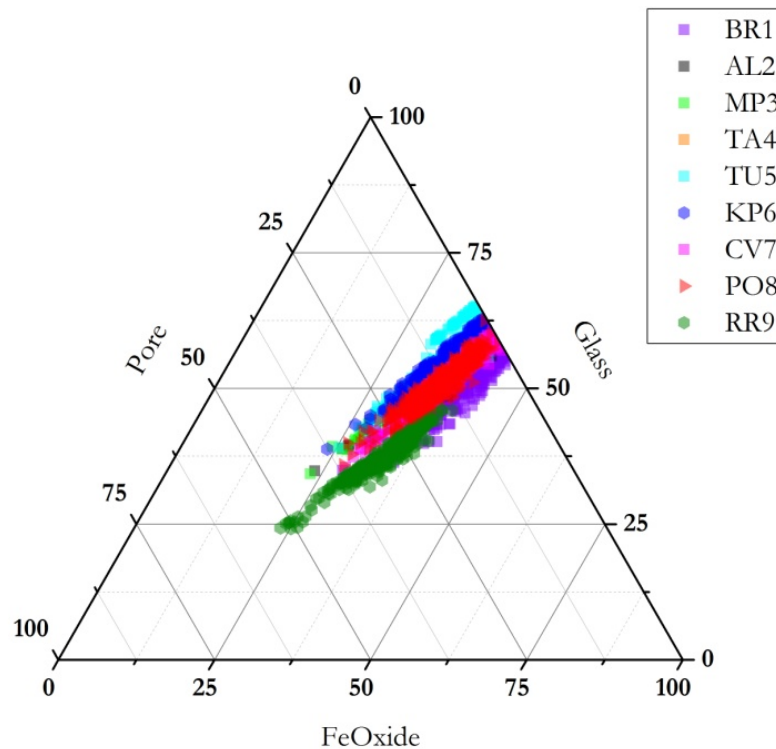
Figure 85: Ternary diagram of the phase association for each image of an image series.

Different evaluation methods were tested. First, the pellet images were treated like iron ore by the simulation of the reduction front by the CPFM. The results are not in coherence with the microscopical observations of the raw pellets to the reduced ones. In the followings, the settings were changed:

a) Fe-oxide (magnetite and hematite) was degraded like magnetite -> no correlation to the reduction behavior.

b) In addition, the glass phase was degraded like magnetite -> no effect on the shape of the curve.

c) Pores smaller than 5 μm in diameter were filled -> effect visible

e) The size of the glass particles was measured, and the cumulative distribution was plotted -> no significant difference between the pellet brands.

f) The specific perimeter of the solid phases, which is an indicator for the specific surface was calculated (= cum. perimeter/(cum. image area − cum. pore area)) -> no correlation to the reduction behavior.

After these tests a statistical analysis of the pore size distribution was carried out. The *Heywood Circularity Factor* was calculated for all pore particles. This factor is the perimeter of the particle (pore) divided by the circumference of a circle with the same area. The closer the shape of a particle is to a disk, the closer the Heywood circularity factor is to 1. The cumulative Heywood factor of the pores of all samples is between 0.8 and 1. Due to that fact

pores were handled as circles. The area of the pores is equaled to a circle area and the equivalent diameter (EQD) is calculated. The resolution of the digital camera cannot resolve particles smaller than 2 μm in diameter (area of 150 pixels at 250 magnification). As a result, pores smaller than 2 μm in EQD are excluded in the statistical analysis and the cumulative distribution diagram. The median values of the pore diameter vary between 40 to <70 pixels, which correspond to 3-<6 μm in diameter, respectively. The distribution of the pore sizes is plotted in a cumulative distribution graph with a logarithmical abscissa and is given in Figure 86. Ninety percent of all pores are smaller than 25 μm in EQD.
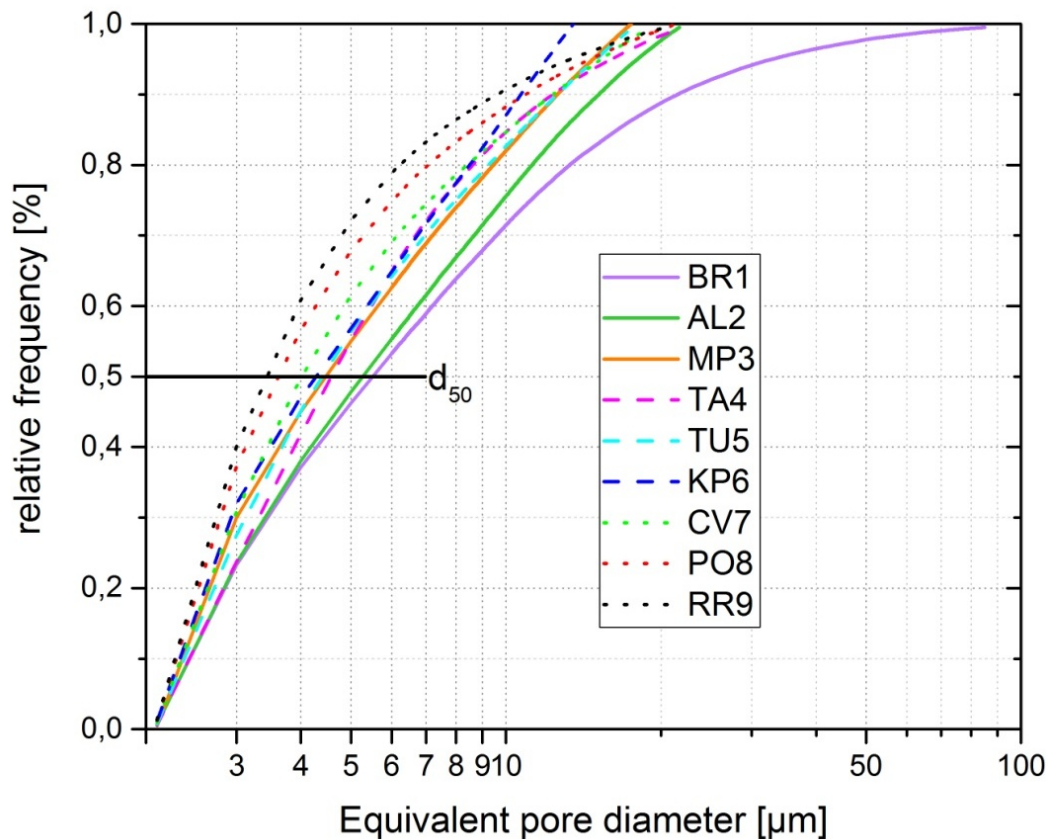
Figure 86: The cumulative distribution curves of the equivalent pore diameter of the investigated pellet samples.

The samples can be divided according to their median EQD into three groups. Group one consists of BR1 and AL2 with a median EQD over 5.4 μm. Group two are CV7, KP6, MP3 and TA4, where the median EQD is between 4 and 4.6 μm. Group three (PO8, RR9) has the lowest median EQD of 3.6 μm.

The homogeneity H(ø) demonstrates how even the pore sizes are distributed within the images of a sample (for more details see 4.3.2). The method is based on an interpretation of the Gini index and it was developed specifically for microstructure homogeneity (Rossi et al. 2014). The homogeneity ($H_{(ø)}$) of the pore size defines the similarity of the component (pore) considering the given attribute (equivalent diameter of the pore). The homogeneity gives a value between 0 and 100 % (inhomogeneous to homogeneous). The H(ø) is higher

for the samples TA4, RR9 and PO8, whereas CV7, TU5 and AL2 have the lowest one. The pore sizes are more evenly distributed in TA4 (58 %) than in TU5 (44 %).

6.   Discussion and Conclusion

Understanding the iron carrier behavior during the reduction process is the basis for efficient process control and production maximization. Aim of this research work was to trace the reduction (phase transformation) of ferrous minerals during the ISO-4695 test and to develop a method of evaluating iron ores and pellets regarding their reducibility. There are different lab testing methods available that are used in daily quality checks, but the morphological and mineralogical characteristics of iron carriers have not gained much attention. In addition, results from standardized testing methods cannot be transferred to one-to-one basis to blast furnace conditions (Loo and Bristow 1998; Geerdes et al. 2015). The microscopical analysis of the iron carriers before, during and after the reducibility test present the following findings:

Iron ores

The morphological characteristics of iron ores are the size and shape of the mineral crystals, the intragranular and overall porosity, and of course the type of ferrous mineral. The simplified reduction paths depend on the preliminary mineral (limonite, hematite/martite or magnetite) (Figure 87). As described in chapter 3.5 the iron oxides follow these paths during the ISO-4695 test. The transformations were observed in the polished sections of the aborted ISO-4695 test conducted at the Chair of Ferrous Metallurgy (MUL).

Only the reduction from limonite to hematite could not be monitored. This transformation starts between 120 °C and 140 °C by removing the free moisture. The dehydroxylation of limonite occurs between 210 and 370 °C (O'Connor et al. 2006). The specific decomposition temperature depends on the crystallinity of the limonite. The tests were aborted between 33 % and 66 % reduction degree with no secondary hematite left. Limonite, to a certain extent, will enhance the overall reducibility by improving the formation of iron nuclei. However, limonite has the lowest total iron content and often a high content of undesired elements (Al etc.).

The morphology of the hematite together with the intragranular porosity determines the factors for the reducibility. In fact, the inner porosity is more decisive at larger crystal sizes than the morphology (see Table 11). Martite is pseudomorphous hematite after magnetite. The octahedral crystal structure of the magnetite is preserved. The trellis structure may be weathering-related by oxidation of magnetite (Angerer et al. 2012) or hydration of maghemite (Morris 1980). However, the trellis structure can also be caused by hydrothermal alteration (Beukes and Gutzmer 2008). The lamellae and interlobate one results from a structural change and create structural defects. The magnetite formed by reduction of dense martite looks dense in first place. But the ancient structure appears during further

reduction creating a porous wuestite structure (see Figure 60). On the contrary, primary magnetite or secondary magnetite formed from dense hematite lead to dense wuestite.

The reduction rate is controlled chemically (removal of oxygen) and by a diffusion process. The last step from wuestite to metallic iron is seen as the rate determining step (Bradshaw 1970). The rate will be influenced by the specific surface of the wuestite, which is determined by the appearance of the starting mineral. The metallic iron forms at the surface of the crystals as a layer and becomes thicker during reduction progress. The layer forms a boundary for the diffusion of the oxygen and lowers the reduction rate. This effect depends on the diameter of the wuestite crystal. Porous wuestite, independent of the crystal size, forms iron scraps and further porous iron. The appearance of the metallic iron depends on the one hand on the temperature, gas conditions and duration of reduction and on the other hand on the textural characteristics of the raw material. Depending on these properties the metallic iron forms sparks, specks, dense seams or a spongy mass.
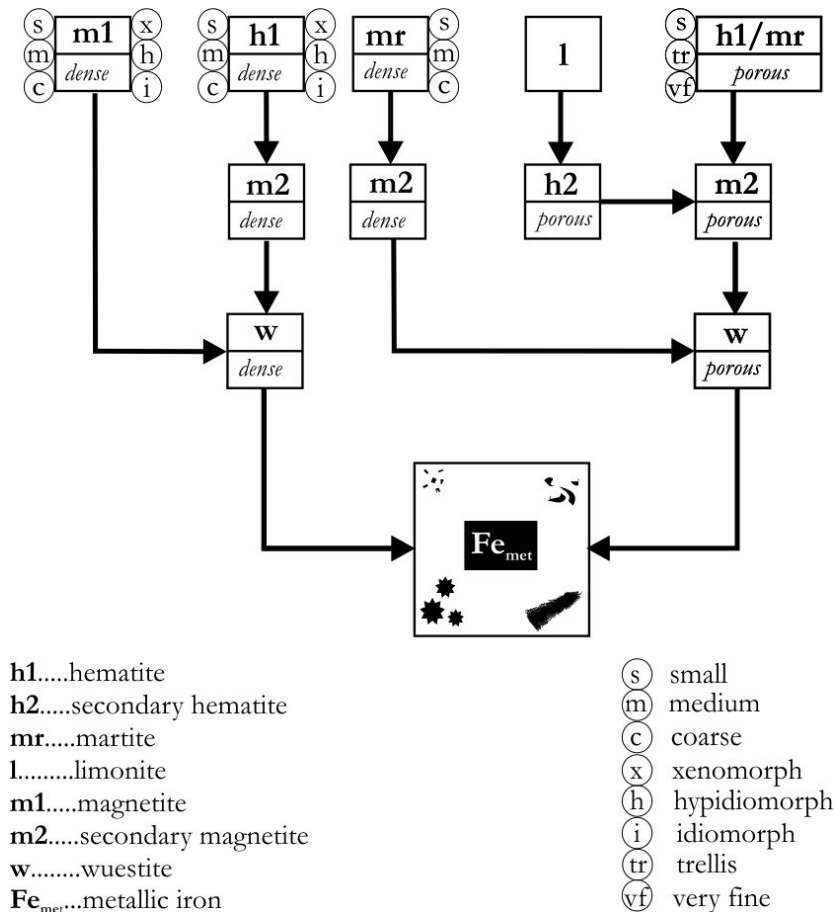
Figure 87: Summary of the phase transformations during reduction of the minerals limonite, hematite/martite and magnetite. These paths results in metallic iron in various shapes.

The ideal reducible iron ore should consist, at the mineralogical point of view, of porous small to medium (<20 μm) xenomorphic hematite and/or martite. A porous texture will to increase the specific surface for the reducing gas. The reduction from hematite to wuestite takes longer, if the hematite is recrystallized or secondary grown due to metamorphic pro-

cesses. Table 11 combines morphology and the intracrystalline porosity of the ferrous minerals for the reducibility evaluation.

Table 11: Classification of the reducibility according the morphological characteristics of the iron-bearing minerals.

morphology		crystal size							
		very fine		small		medium		coarse	
porous/dense		p	d	p	d	p	d	p	d
limonite									
hematite	idiomorphic								
	hypidiomorphic								
	xenomorphic								
martite									
magnetite									

Reducibility

excellent	
good	
intermediate	
bad	

This evaluation is to a certain extent subjective, as every microscopical analysis made by humans. The image processing software VisuMet has been developed to minimize this error. It combines the structural characteristics of the minerals and the different reducibilities of ferrous minerals to simulate the reduction progress. The CPFM model was implemented through the Danielsson distance map and the different degradation of the minerals. The results of this area degradation are now compared to the ISO-4695 tests conducted at the Chair of Ferrous Metallurgy (MUL)(Figure 88).

The nine iron ore samples were tested and the results are displayed as reduction curves (reduction degree vs. time). The samples can be divided into two groups. Group one reaches 80 % reduction degree (R_{80}) between 75-85 min. The second group needs approximately 140-160 min, respectively. The tests of the samples SI and KI were cancelled before reaching R_{80}, due to lack of further progression.
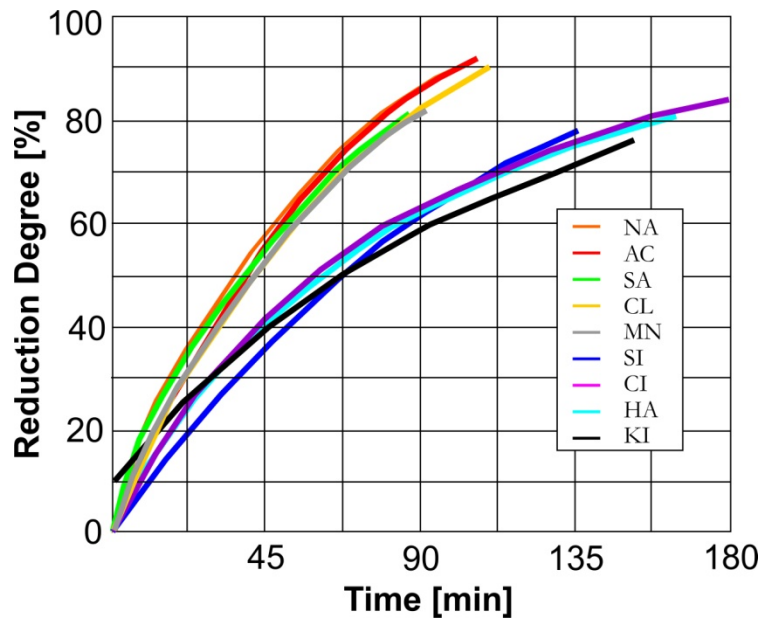
Figure 88: Reduction curves as a result of the ISO-4695 testing procedure from the Chair of Ferrous Metallurgy (MUL).

The results of the ISO-tests were compared to the VisuMet degradation curves by correlation of the values' time [min] and steps for removing the particle area. The cross correlation of time needed to reach a reduction degree of 70 % and the number of steps to remove 70 % of the particle area is 61.7% (Figure 89). One step in VisuMet corresponds to approximately 5 min in a reduction test.
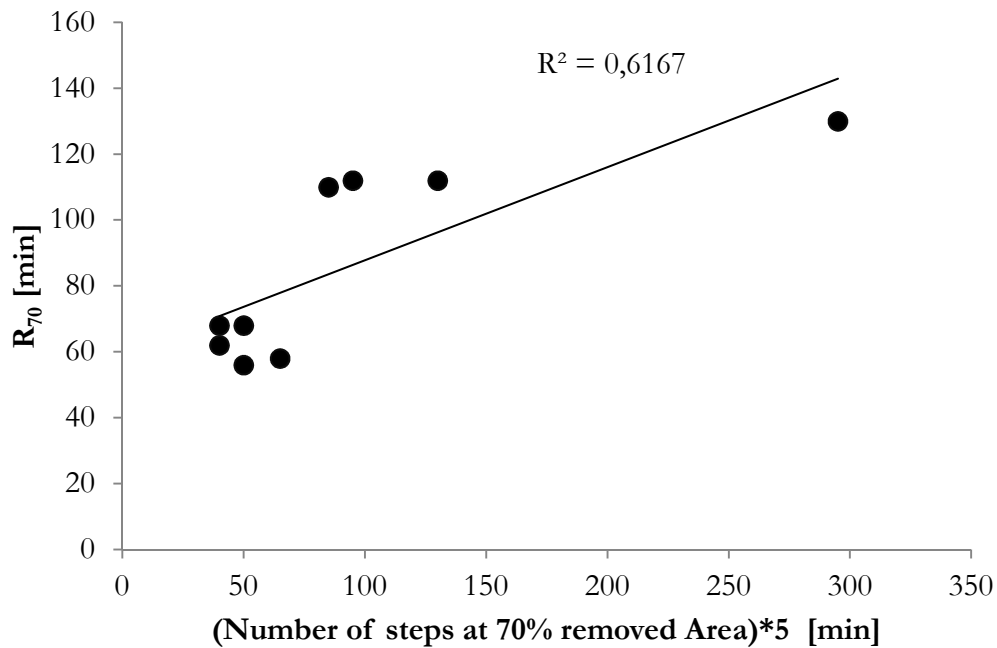
Figure 89: Cross-correlation of the time needed to achieve 70 % reduction degree and the number of steps needed to remove 70 % of particle area of all classified phases.

The reducibility (RI) is described as $(dR/dt)_{40}$ [%/min] by the formula $= 33.3/(t_{60}-t_{30})$. The terms t_{60} and t_{30} refer to the time needed for 30 % and 60 % reduction degree, respectively. The area degradation rate of the VisuMet curve can be calculated in a similar way: $(dR_A/ds)_{40}= 33.3/(s_{60}-s_{30})$ [%/steps], where s_{60} and s_{30} are the number of steps needed to remove 30 % and 60% of the particle area. The correlation has an R-squared of 0.92 (Figure 90). The reducibility between 30 % and 60 % reduction degree correlates with the CPFM based area degradation rate of the mineral particles. The mineral type, the crystal size and shape are decisive for the reducibility. The specific values for the cross correlations are given in Table 12.
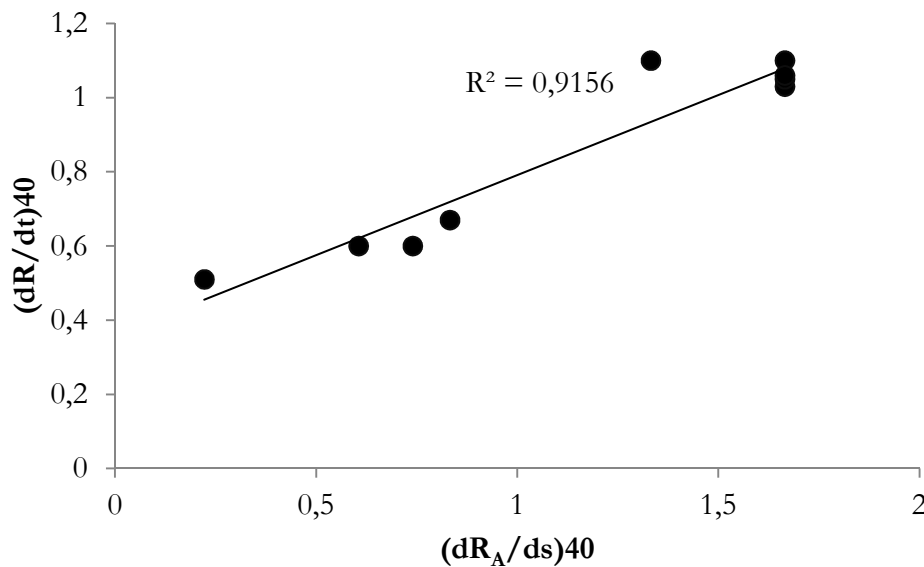
Figure 90: Cross correlation of reducibility and the respective VisuMet area degradation rate.

Table 12: Values of the cross correlation. The curves of the reduction test and the data were made available by the Chair of Ferrous Metallurgy.

Sample	R_{70} [min]	$(dR/dt)_{40}$ [%/min]	S_{70} [steps*5min]	$(dR_A/ds)_{40}$ [%/steps]
MN	68	1.05	50	1.7
KI	130	0.51	295	0.2
SI	110	0.67	85	0.8
AC	58	1.1	65	1.3
NA	56	1.1	50	1.7
CL	68	1.06	40	1.7
HA	112	0.6	95	0.7
SA	62	1.03	40	1.7
CI	112	0.6	130	0.6

The comparison of the VisuMet results and the standard reduction test results demonstrate clearly that the algorithm of the CPFM includes the morphological key factors for the prediction of reducibility of lumpy iron ores.

Other key factors for the reduction behavior can be the impurities build in the lattice of the iron oxides or other elements of the gangue. But these effects cannot be determined by optical microscopy, but need chemical methods.

Pellets

The morphological characteristics of pellets are simpler than in iron ore. The main mineral is hematite, more or less rounded due to the pelletization process. Magnetite occurs in the cores of poorly burned pellets. The binder, together with the gangue of the iron ore fines is transformed to glass. The glass is incorporated in the growing hematite or surrounds the crystals and the pores. The reduced samples demonstrate that the reduction takes place in a more regular way than for iron ores. The crystal size of the iron oxides is small to medium. The raw material of the pellets are iron ore fines with a specific grain size. During the pelletization process the iron oxide crystals start to accumulative crystallize and become more rounded. Under favorable conditions partial melting occurs. The microstructure is more homogenous and the pores are evenly distributed building a connected pore network from the margin to the core of the pellet.

The reduction starts at the margin of the pellet and proceeds in the core in accordance to the shrinking core model. The hematite is transformed to magnetite and further to wuestite, like the hematite (h1, dense) path in iron ores. Metallic iron forms first as iron sparks at the margin of the pellet and the reduction front migrates further towards the core. In the next stage the metallic iron forms thin layers around the iron oxides. The layers grow further inside during the ISO-4695 test until the entire wuestite crystal is changed to metallic iron (Figure 91).

The size of the iron oxides plays a role in the reducibility of pellets, but the results by applying the algorithm of the CPFM demonstrate that the size or specific thickness of the iron oxide crystal are not the key factors for the reduction rate. There is no significant difference in the area degradation curves of the individual pellet samples. In addition the area was removed too fast (steep area degradation curve), which was not in correspondence to the microscopical studies of the reduced samples.

The major noticeable difference is the pore size and distribution among the investigated pellet samples. The statistical evaluation of the pore size indicates that the higher the amount of pores with an EQD > 5 μm, the better is the reducibility. The nine pellet samples were tested at the Chair of Ferrous Metallurgy after ISO-4695 and the reduction curves are displayed in Figure 92. The values for R_{80} and RI are given in Table 13.
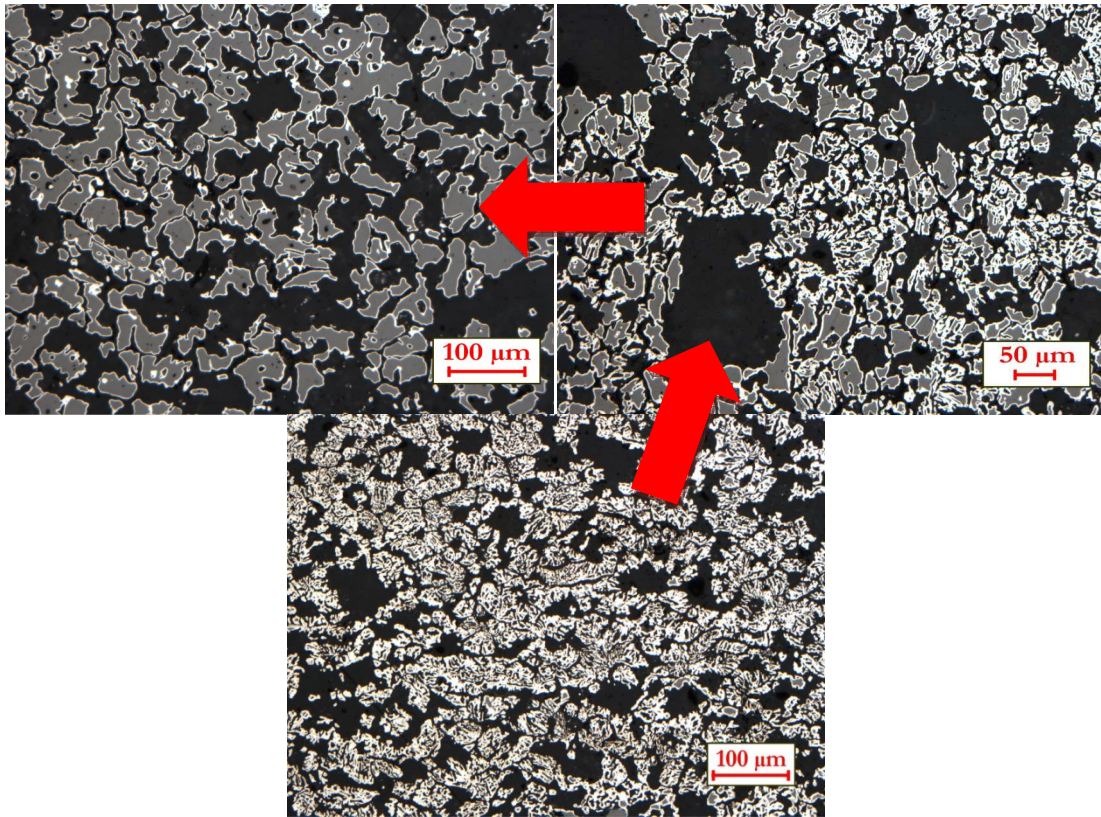
Figure 91: Reduction progress from the margin to core within a pellet.
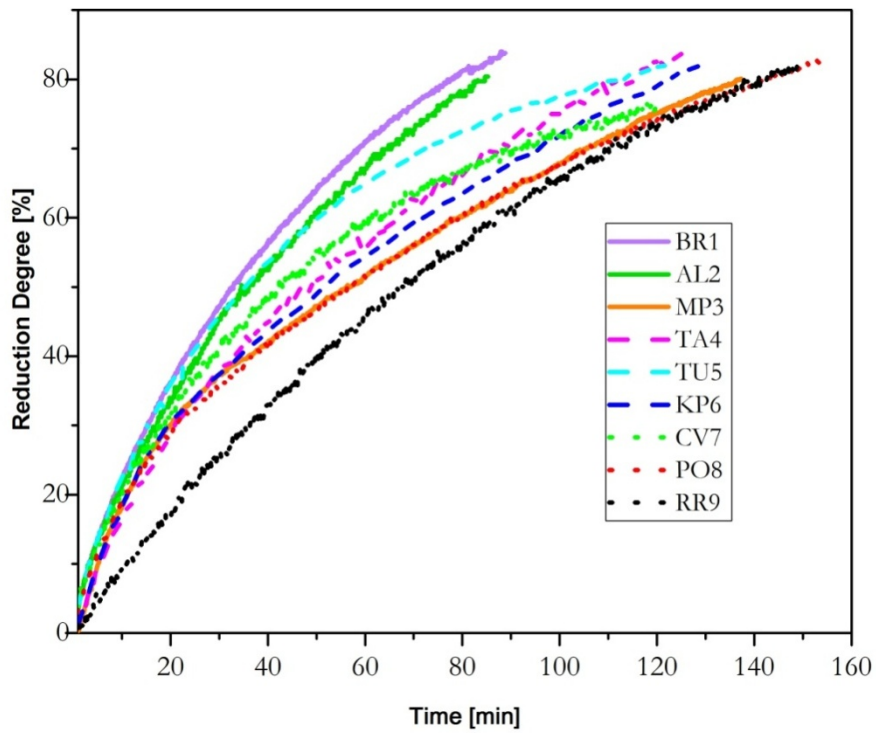
Figure 92: Reduction curves after ISO-4695 test conducted at the Chair of Ferrous Metallurgy of the same pellet samples.

According to the reduction curves the pellets can be divided into three groups. Group 1 consists of BR1 and AL3, which reach 80% reduction degree (80-84 min) fastest. The second group (TA4, TU5, KP6) needs 114 to 122 min to get 80% reduction degree. The last group requires 137 to 142 min. The reduction test of CV7 was aborted before reaching 80% reduction degree.

Table 13: Summary of the results of VisuMet and the reduction tests made at the Chair of Ferrous Metallurgy (MUL).

Sample	Median p ø [µm]	Pore [%]	H(ø) [%]	$RI=(dR/dt)_{40}$ [%/min]	R_{80} [min]
RR9_1	3.4	48	57	0.65	142
RR9_2	3.8	47	55		
PO8	3.6	38	52	0.58	142
CV7	4	31	45	0.78	App. 142*
MP3	5	38	50	0.57	137
KP6	4.3	36	48	0.65	122
TU5	4.3	34	44	0.95	120
TA4	4.6	27	58	0.74	114
AL2_1	5.4	32	44	1.03	84
AL2_2	5.4	36	48		
BR1	5.5	31	48	1.15	80

*The reduction test was aborted before reaching 80% reduction degree.

The effect of the pore size on the reduction rate (RI) is demonstrated by the cross correlation of the median EQD and the RI in Figure 93. The R^2 is 0.67, which indicates a certain influence. This indicates that the RI depends to a certain extent on the morphological characteristics of the pellets. By considering the R_{80} and the median EQD this effect emerges stronger.
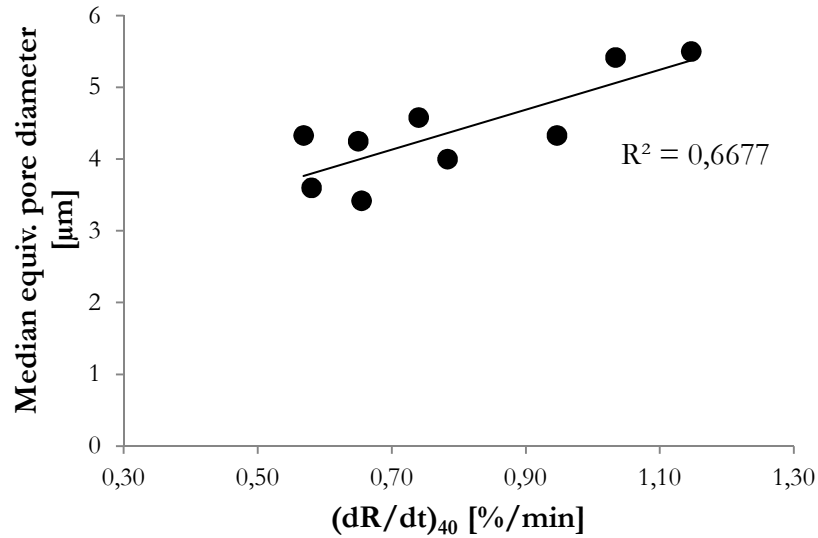
Figure 93: Correlation of the median equivalent pore diameter and RI of the investigated pellet samples.

The correlation of the median of the EQD and R_{80} of the pellet samples demonstrates that the pore size is a key factor for the reducibility of pellets. The R-squared of the trendline is 0.91 (Figure 94). This relationship indicates that the pore size distribution and pore network can be enhanced by the pelletization process concerning the pore formation to improve the reducibility. It is possible to statistically analyze the pore size and homogeneity distribution of the pellets by optical and image processing methods like VisuMet in simple and favorable way.
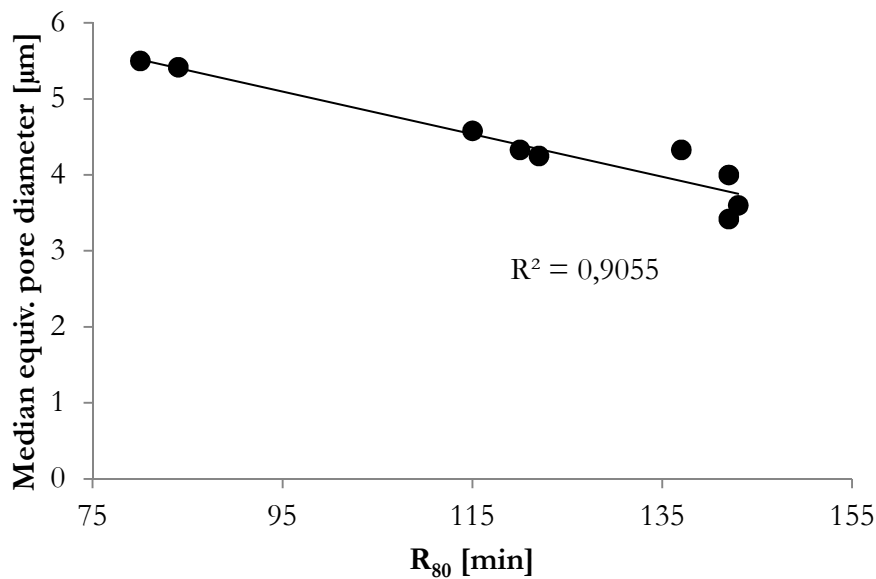
Figure 94: Cross correlation of the median EQD and the R_{80} of the investigated pellet samples.

The research has shown that the reducibility and reduction rate of lumpy iron carriers are related to the morphological and mineralogical characteristics. These characteristics can be determined by time-consuming microscopical investigation or by the newly developed image processing software VisuMet. VisuMet combines the structural properties (size, shape, porosity) with the different behavior of the iron oxides during the phase transformations from the starting mineral to metallic iron. VisuMet will not replace first detailed microscopical analyses, but supports the evaluation by quantifying the mineral abundance and simulating the reduction progress of lump ores. Furthermore, it is possible to statistically analyze the pore size and homogeneity distribution of pores in the pellets, which can be used as a tool to evaluate pellets for their usage and enhance the pelletization process.

References

Alvarez, J. C.; Wagner, D.; Schinazi, G.; Gomes, O. D. M.; Maurício, M. H.P.; Paciornik, S.; Vieira, M. B. (2008): Qualitative and quantitative evaluation of iron ore sinters through digital microscopy. In, vol. 9. International congress on applied mineralogy. Brisbane, pp. 669–672.

Angerer, T.; Hagemann, S. G.; Danyushevsky, L. V. (2012): Geochemical Evolution of the Banded Iron Formation-Hosted High-Grade Iron Ore System in the Koolyanobbing Greenstone Belt, Western Australia. In *Economic Geology* 107 (4), pp. 599–644. DOI: 10.2113/econgeo.107.4.599.

Angerer, Thomas; Duuring, Paul; Hagemann, Steffen G.; Thorne, Warren; McCuaig, T. Campbell (2015): A mineral system approach to iron ore in Archaean and Palaeoproterozoic BIF of Western Australia. In *Geological Society, London, Special Publications* 393 (1), pp. 81–115. DOI: 10.1144/SP393.11.

Angerer, Thomas; Hagemann, Steffen G.; Walde, Detlef H.G.; Halverson, Galen P.; Boyce, Adrian J. (2016): Multiple metal sources in the glaciomarine facies of the Neoproterozoic Jacadigo iron formation in the "Santa Cruz deposit", Corumbá, Brazil. In *Precambrian Research* 275, pp. 369–393. DOI: 10.1016/j.precamres.2016.01.002.

Babich, A. (2008): Ironmaking. Textbook. Aachen: RWTH Univ. Dep. of Ferrous Metallurgy.

Beukes, N.; Gutzmer, J. (2008): Origin and Paleoenvironmental Significance of Major Iron formations at the Archean-Paleoproterozoic Boundary. In *Reviews in Economic Geology* 15, pp. 5–47, checked on 1/8/2018.

Beukes, N. J.; Gutzmer, J.; Mukhopadhyay, J. (2013): The geology and genesis of high-grade hematite iron ore deposits. In *Applied Earth Science* 112 (1), pp. 18–25. DOI: 10.1179/037174503225011243.

Bogdandy, L.; Engell, H. J. (1967): Die Reduktion der Eisenerze. Berlin, Heidelberg: Springer Berlin Heidelberg.

Bradshaw, A. V. (1970): Rate-Controlling Factors in Gas-Solid Reactions of Metallurgical Interest. In *Transactions of the Institution of Mining and Metallurgy* (79).

Carney, M. D.; Mienie, P. J. (2013): A geological comparison of the Sishen and Sishen South (Welgevonden) iron ore deposits, Northern Cape Province, South Africa. In *Applied Earth Science* 112 (1), pp. 81–88. DOI: 10.1179/0371745032501171.

Chaigneau, R. (1994): Complex calcium ferrites in the blast furnace process. Fluxed sinter formation and SFCA reduction under simulated conditions. Delft: Delft University Press.

Chayes, F. (1956): Petrographic modal analysis. An elementary statistical appraisal. New York: John Wiley.

Clout, J. M. F. (2003): Upgrading processes in BIF-derived iron ore deposits. Implications for ore genesis and downstream mineral processing. In *Applied Earth Science* 112 (1), pp. 89–95. DOI: 10.1179/0371745032501153.

Cornell, R. M.; Schwertmann, U. (2003): The Iron Oxides. Structure, Properties, Reactions, Occurences and Uses. 2nd, Completely Revised and Extended ed. Weinheim: Wiley-VCH Verlag GmbH & Co. KGaA. Available online at http://www.myilibrary.com/?id=56077.

Danielsson, P.-E. (1980): Euclidean distance mapping. In *Computer Graphics and Image Processing* 14 (3), pp. 227–248. DOI: 10.1016/0146-664X(80)90054-4.

Donskoi, E.; Manuel, J.; Austin, P.; Poliakov, A.; Peterson, M.; Hapugoda, S. (2013): Comparative study of iron ore characterisation using a scanning electron microscope and optical image analysis. In *Applied Earth Science* 122 (4), pp. 217–229. DOI: 10.1179/1743275814Y.0000000042.

Donskoi, E.; Poliakov, A.; Manuel, J.; Peterson, M.; Hapugoda, S. (2015): Novel developments in optical image analysis for iron ore, sinter and coke characterisation. In *Applied Earth Science*, 1743275815Y.000. DOI: 10.1179/1743275815Y.0000000013.

Donskoi, E.; Suthers, S. P.; Campbell, J. J.; Raynlyn, T. (2008): Modelling and optimization of hydrocyclone for iron ore fines beneficiation — using optical image analysis and iron ore texture classification. In *International Journal of Mineral Processing* 87 (3-4), pp. 106–119. DOI: 10.1016/j.minpro.2008.02.006.

Donskoi, E.; Suthers, S. P.; Fradd, S. B.; Young, J. M.; Campbell, J. J.; Raynlyn, T.; Clout, J. M. F. (2007): Utilization of optical image analysis and automatic texture classification for iron ore particle characterisation. In *Minerals Engineering* 20 (5), pp. 461–471. DOI: 10.1016/j.mineng.2006.12.005.

Dwarapudi, S.; Ghosh, T. K.; Shankar, A.; Tathavadkar, V.; Bhattacharjee, D.; Venugopal, R. (2011): Effect of pellet basicity and MgO content on the quality and microstructure of hematite pellets. In *International Journal of Mineral Processing* 99 (1-4), pp. 43–53. DOI: 10.1016/j.minpro.2011.03.004.

Eisele, T. C.; Kawatra, S. K. (2003): A review of binders in iron ore pelletization. In *Mineral Processing and Extractive Metallurgy Review* 24 (1), pp. 1–90. DOI: 10.1080/08827500306896.

Ferenčić, Ante J. (1969): Geology of the San Isidro iron ore deposit, Venezuela. In *Mineralium Deposita* 4 (3), pp. 283–297. DOI: 10.1007/BF00207131.

Flickenschild, J.; Hauk, Rolf; Steffen, R. (2013): Iron, 4. Smelting Reduction Processes. In : Ullmann's Encyclopedia of Industrial Chemistry: Wiley-VCH Verlag GmbH & Co. KGaA.

Francus, P. (Ed.) (2005): Image Analysis, Sediments and Paleoenvironments. Dordrecht: Springer Science + Business Media Inc (Developments in Paleoenvironmental Research, 7). Available online at http://dx.doi.org/10.1007/1-4020-2122-4.

Gastwirth, Joseph L. (1972): The Estimation of the Lorenz Curve and Gini Index. In *The Review of Economics and Statistics* 54 (3), p. 306. DOI: 10.2307/1937992.

Geerdes, M.; Chaigneau, R.; Kurunov, I. (2015): Modern Blast Furnace Ironmaking. An Introduction (Third Edition, 2015). 32015th ed. Burke: IOS Press. Available online at http://gbv.eblib.com/patron/FullRecord.aspx?p=2033826.

Gomes, O. da F. M.; Iglesias, J.C.A; Paciornik, S. (2013): Classification of hematite types in iron ores through circularly polarized light microscopy and image analysis. In *Minerals Engineering* (52), pp. 191–197. Available online at http://www.sciencedirect.com/science/article/pii/S0892687513002379, checked on 2/24/2015.

Habermann, A.; Winter, F.; Hofbauer, H.; Zirngast, J.; Schenk, J. (2000): An Experimental Study on the Kinetics of Fluidized Bed Iron Ore Reduction. In *ISIJ International* 40 (10), pp. 935–942. DOI: 10.2355/isijinternational.40.935.

Hagemann, S. G.; Angerer, T.; Duuring, P.; Rosière, C. A.; Figueiredo e Silva, R. C.; Lobato, L. et al. (2016): BIF-hosted iron mineral system. A review. In *Ore Geology Reviews* 76, pp. 317–359. DOI: 10.1016/j.oregeorev.2015.11.004.

Hagemann, Steffen Gerd (2008): Banded iron formation-related high-grade iron ore. Littleton, Colo.: Society of Economic Geologists (Reviews in economic geology, v. 15).

Hanel, M. (2014): Characterization of Ferrous Burden Material for Use in Ironmaking Technologies. PhD Thesis. Montanuniversität Leoben, Leoben. Chair of ferrous metallurgy.

Hapugoda, S.; Lu, L.; Donskoi, E.; Manuel, J. (2016): Mineralogical quantification of iron ore sinter. In *Mineral Processing and Extractive Metallurgy* 125 (3), pp. 156–164. DOI: 10.1080/03719553.2016.1164797.

Higuchi, K.; Orimoto, T.; Koizumi, F.; Furuta, H.; Takamoto, Y.; Sato, T.; Shinagawa, K. (2006): Quality improvement of sintered ore in relation to blast furnace operation. In *Nippon Steel Technical Report* 94.

Hsieh, L.-H. (2005): Effect of Raw Material Composition on the Sintering Properties. In *ISIJ International* 45 (4), pp. 551–559. DOI: 10.2355/isijinternational.45.551.

Jonsson, Erik; Troll, Valentin R.; Högdahl, Karin; Harris, Chris; Weis, Franz; Nilsson, Katarina P.; Skelton, Alasdair (2013): Magmatic origin of giant 'Kiruna-type' apatite-iron-oxide ores in central Sweden. In *Scientific reports* 3, p. 1644. DOI: 10.1038/srep01644.

Jozwiak, W. K.; Kaczmarek, E.; Maniecki, T. P.; Ignaczak, W.; Maniukiewicz, W. (2007): Reduction behavior of iron oxides in hydrogen and carbon monoxide atmospheres. In *Applied Catalysis A: General* 326 (1), pp. 17–27. DOI: 10.1016/j.apcata.2007.03.021.

Kain-Bückner, B.; Mali, H. (June/2015): Valuation and optimization of iron carriers in reduction processes. Project 4.2 Area IV. Montanuniversität Leoben. Leoben, checked on unpublished.

Kalenga, M. K.; Garbers-Craig, A. M. (2010): Investigation into how the magnesia, silica, and alumina contents of iron ore sinter influence its mineralogy and properties. In *Journal of the Southern African Institute of Mining and Metallurgy* 110 (8), pp. 447–456.

Komatina, M.; Gudenau, H. W. (2004): The sticking problem during direct reduction of fine iron ore in the fluidized bed. In *Metalurgija* 10 (4), pp. 309–328.

Lane, G. R.; Martin, C.; Pirard, E. (2008): Techniques and applications for predictive metallurgy and ore characterization using optical image analysis. In *Minerals Engineering* 21 (7), pp. 568–577. DOI: 10.1016/j.mineng.2007.11.009.

Lastra, R.; Petruk, W.; Wilson, J. (1998): Image analysis techniques and applications to mineral processing. In *Modern Approaches to Ore and Environmental Mineralogy* 27, pp. 327–366.

Levenspiel, O. (1999): Chemical reaction engineering. 3. ed. Hoboken, NJ: Wiley. Available online at http://www.loc.gov/catdir/description/wiley033/97046872.html.

Loo, C. E.; Bristow, N. J. (1998): Properties of iron bearing materials under simulated blast furnace indirect reduction conditions. Part 1-review and experimental procedure. In *Ironmaking & Steelmaking* 25 (3), p. 222.

Lu, L. (Ed.) (2015): Iron ore. Mineralogy, processing and environmental sustainability. Cambridge, UK: Woodhead Publishing (Woodhead Publishing series in metals and surface engineering, number 66).

Mali, H.; Spuida, B. (2013): Automatisierte Mikrobild-Analyse zur Klassifizierung von Eisenerz für die Roheisenherstellung. In *BHM Berg- und Hüttenmännische Monatshefte* 158 (2), pp. 47–52. DOI: 10.1007/s00501-013-0119-y.

Meinert, L. (1992): Skarns and Skarn Deposits. In *Geoscience Canada* 19 (4).

Midrex Technologies Inc. (2014): The MIDREX® Process. Available online at http://www.midrex.com/assets/user/media/MIDREX_Process-Brochure.pdf.

Mochón, J.; Cores, A.; Ruiz-Bustinza, I.; Verdeja, L. F.; Robla, J. I.; Garcia-Carcedo, F. (2014): Iron ore sintering part 2. Quality indices and productivity. In *DYNA* 81 (183), pp. 168–177. DOI: 10.15446/dyna.v81n183.41568.

Morris, R. C. (1980): A textural and mineralogical study of the relationship of iron ore to banded iron-formation in the Hamersley iron province of Western Australia. In *Economic Geology* 75 (2), pp. 184–209. DOI: 10.2113/gsecongeo.75.2.184.

Morris, R. C. (2012): Microplaty hematite—its varied nature and genesis. In *Australian Journal of Earth Sciences* 59 (3), pp. 411–434. DOI: 10.1080/08120099.2011.626453.

Morris, R. C.; Thornber, M. R.; Ewers, W. E. (1980): Deep-seated iron ores from banded-iron formation. In *Nature* 288, 250 EP -. DOI: 10.1038/288250a0.

Noguchi, D.; Ohno, K.-i.; Maeda, T.; Nishioka, K.; Shimizu, M. (2013): Kinetics of Reduction Step of Wustite to Iron of Hematite and Quaternary Calcium Ferrite Mixtures. In *ISIJ International* 53 (8), pp. 1350–1357. DOI: 10.2355/isijinternational.53.1350.

O'Connor, F.; Cheung, W. H.; Valix, M. (2006): Reduction roasting of limonite ores. Effect of dehydroxylation. In *International Journal of Mineral Processing* 80 (2-4), pp. 88–99. DOI: 10.1016/j.minpro.2004.05.003.

Paananen, T. (2013): The effect of minor oxide components on reduction of iron ore agglomerates: Ph. D. thesis. University of Oulu, Finland.

Pichler, A.; Mali, H.; Plaul, F. J.; Schenk, J.; Skorianz, M.; Weiss, B. (2016): Reduction Behavior and Structural Evolution of Iron Ores in Fluidized Bed Technologies-Part 2. Characterization and Evaluation of Worldwide Traded Fine Iron Ore Brands. In *Steel research international* 87 (5), pp. 642–652. DOI: 10.1002/srin.201500176.

Pirard, E.; Lebichot, S. (Eds.) (2004): Image Analysis of Iron Oxides under the Optical Microscope. Developments in science and technology. With assistance of M. Pecchio, F. R. D. de Andrade,, L. Z. D'Agostino, H. Kahn, L. M. Sant'Agostino, M. Tassinari. ICAM-2004. Águas de Lindoia. São Paulo: ICAM (Applied Mineralogy: Developments in Science and Technology, 1). Available online at http://hdl.handle.net/2268/41167.

Pirard, E.; Lebichot, S.; Krier, W. (2007): Particle texture analysis using polarized light imaging and grey level intercepts. In *International Journal of Mineral Processing* 84 (1-4), pp. 299–309. DOI: 10.1016/j.minpro.2007.03.004.

Pirrie, D.; Butcher, A. R.; Power, M. R.; Gottlieb, P.; Miller, G. L. (2004): Rapid quantitative mineral and phase analysis using automated scanning electron microscopy (QemSCAN); potential applications in forensic geoscience. In *Geological Society, London, Special Publications* 232 (1), pp. 123–136. DOI: 10.1144/GSL.SP.2004.232.01.12.

Prochaska, Walter (2016): Genetic concepts on the formation of the Austrian magnesite and siderite mineralizations in the Eastern Alps of Austria. In *Geol Cro* 69 (1), pp. 31–38. DOI: 10.4154/GC.2016.03.

Ramanaidou, E. R.; Morris, R. C. (2013): Comparison of supergene mimetic and supergene lateritic iron ore deposits. In *Applied Earth Science* 119 (1), pp. 35–39. DOI: 10.1179/037174510X12853354810589.

Rossi, P.; Engstler, M.; Mücklich, F. (2014): Homogeneity Quantification Method and its Application to Microstructure Assessment. In *Practical Metallography* 51 (3), 180-199. DOI: 10.3139/147.110287.

Skorianz, M.; Mali, H.; Pichler, A.; Plaul, F. J.; Schenk, J.; Weiss, B. (2016): Reduction Behavior and Structural Evolution of Iron Ores in Fluidized Bed Technologies. Part 1. Method for the Determination. In *Steel research international* 87 (5), pp. 633–641. DOI: 10.1002/srin.201500175.

Stahl-Zentrum. Available online at http://en.stahl-online.de/index.php/topics/technology/steelmaking/.

Sutherland, D. N.; Gottlieb, P. (1991): Application of automated quantitative mineralogy in mineral processing. In *Minerals Engineering* 4 (7-11), pp. 753–762. DOI: 10.1016/0892-6875(91)90063-2.

Szekely, J.; Evans, J. W. (1970): A structural model for gas—solid reactions with a moving boundary. In *Chemical Engineering Science* 25 (6), pp. 1091–1107. DOI: 10.1016/0009-2509(70)85053-9.

Tonžetić, I.; Dippenaar, A. (2011): An alternative to traditional iron-ore sinter phase classification. In *Minerals Engineering* 24 (12), pp. 1258–1263. DOI: 10.1016/j.mineng.2011.04.012.

Umadevi, T.; Kumar, P.; Lobo, N. F.; Prabhu, M.; Mahapatra, P. C.; Ranjan, M. (2011): Influence of Pellet Basicity (CaO/SiO_2) on Iron Ore Pellet Properties and Microstructure. In *ISIJ International* 51 (1), pp. 14–20. DOI: 10.2355/isijinternational.51.14.

Urban, H.; Stribrny, B.; Lippolt, H. J. (1992): Iron and manganese deposits of the Urucum District, Mato Grosso do Sul, Brazil. In *Economic Geology* 87 (5), pp. 1375–1392. DOI: 10.2113/gsecongeo.87.5.1375.

USGS (1998,2017): Mineral Commodity Summaries. Iron Ore Statistics and Information. Edited by U.S. Geological Survery. Available online at https://minerals.usgs.gov/minerals/pubs/commodity/iron_ore/index.html.

Weibel, E. R. (1979): Practical methods for biological morphometry. London: Acad. Press (Stereological methods, / Ewald R. Weibel ; Vol. 1).

Weibel, E. R. (1989): Measuring through the microscope. Development and evolution of stereological methods. In *Journal of Microscopy* 155 (3), pp. 393–403. DOI: 10.1111/j.1365-2818.1989.tb02898.x.

Westhues, A.; Hanchar, J. M.; Whitehouse, M. J.; Martinsson, O. (2016): New Constraints on the Timing of Host-Rock Emplacement, Hydrothermal Alteration, and Iron Oxide-Apatite Mineralization in the Kiruna District, Norrbotten, Sweden. In *Economic Geology* 111 (7), pp. 1595–1618. DOI: 10.2113/econgeo.111.7.1595.

Wyderko-Delekta, Marta; Bolewski, Andrzej (1995): Mineralogia spieków i grudek rudnych: Wydawnictwa AGH.

Xu, Deru; Wang, Zhilin; Cai, Jianxin; Wu, Chuanjun; Bakun-Czubarow, Nonna; Wang, Li et al. (2013): Geological characteristics and metallogenesis of the shilu Fe-ore deposit in Hainan Province, South China. In *Ore Geology Reviews* 53, pp. 318–342. DOI: 10.1016/j.oregeorev.2013.01.015.

Annex 1

Overview of point counting

%	Lump 5	Lump 2	Pellet 5	Pellet 1	Sin 1	Sin 2
Limonite	17	-	-	-	-	-
Hematite	82	98	60	58	1	<1
Magnetite	1	2			48	44
Pore	-	-	35	31	8	16
Glass	-	-	5	11	-	-
Glass + Si- Ferrite	-	-	-	-	26	17
Ca-Ferrite + SFCA	-	-	-	-	17	24
Σ	100	100	100	100	100	100

Overview of VisuMet

%	Lump 5	Lump 2	Pellet 5	Pellet 1	Sin 1	Sin 2
Limonite	18	-	-	-	-	-
Hematite	81	99	61	56	4	3
Magnetite/ Spinel	1	1			49	43
Pore	-	-	34	31	7	15
Glass	-	-	5	13	-	-
Glass + Si- Ferrite	-	-	-	-	27	15
Ca-Ferrite +SFCA	-	-	-	-	13	24
Σ	100	100	100	100	100	100

Lump 5

Mineral	Pos1	Pos2	Pos3	Pos4	Pos5	Pos6	Sum	Vol%
Hematite	305	325	339	340	342	317	1968	82
Magnetite	6	1	5	8	0	4	24	1
Limonite	89	74	56	52	58	79	408	17
Σ	**400**	**400**	**400**	**400**	**400**	**400**	**2400**	**100**

Lump 2

Mineral	Pos1	Pos2	Pos3	Pos4	Pos5	Pos6	Sum	Vol%
Hematite	389	389	391	392	393	390	2344	98
Magnetite	11	11	9	8	7	10	56	2
Limonite	0	0	0	0	0	0	0	0
Σ	**400**	**400**	**400**	**400**	**400**	**400**	**2400**	**100**

Pellet 5

Mineral	Pos1	Pos2	Pos3	Pos4	Pos5	Pos6	Sum	Vol%
FeOxide	242	231	236	202	297	234	1442	60
Pore	147	152	151	175	79	145	849	35
Glass	11	17	13	23	24	21	109	5
Σ	**400**	**400**	**400**	**400**	**400**	**400**	**2400**	**100**

Pellet 1

Mineral	Pos1	Pos2	Pos3	Pos4	Pos5	Pos6	Sum	Vol%
FeOxide	208	256	232	206	263	232	1397	58
Pore	152	117	123	155	95	108	750	31
Glass	40	27	45	39	42	60	253	11
Σ	**400**	**400**	**400**	**400**	**400**	**400**	**2400**	**100**

Sin 1

Mineral	Pos1	Pos2	Pos3	Pos4	Pos5	Pos6	Sum	Vol%
Magnetite	161	100	244	272	265	115	1157	48
Hematite	15	0	5	8	0	5	33	1
Ca-Ferrite +SFCA	102	84	51	37	45	82	401	17
Glass + Si-Ferrite	83	212	45	45	41	198	624	26
Pore	39	4	55	38	49	0	185	8
Σ	**400**	**400**	**400**	**401**	**400**	**400**	**2401**	**100**

Sin 2

Mineral	Pos1	Pos2	Pos3	Pos4	Pos5	Pos6	Sum	Vol%
Magnetite	158	100	242	202	272	80	1054	44
Hematite	0	1	0	0	0	4	5	0
Ca-Ferrite +SFCA	57	15	102	124	78	20	396	17
Glass + Si-Ferrite	90	200	44	29	0	210	573	24
Pore	95	84	12	45	50	86	372	16
Σ	**400**	**400**	**400**	**400**	**400**	**400**	**2400**	**100**

Data for the cross-correlation (PC= Point counting, VM= VisuMet)

%		Lump 5	Lump 5	Pellet 5	Pellet 1	Sin 1	Sin 2
Limonite	PC	17					
	VM	18					
Magnetite	PC	1	2	60	58	48	44
	VM	1	1	61	56	49	43
Hematite	PC	82	98			1	0
	VM	81	99			4	3
Ca-Ferrite +SFCA	PC					17	24
	VM					13	24
Glass + Si-Ferrite	PC			5	11	26	17
	VM			5	13	27	15
Pore	PC			35	31	8	16
	VM			34	31	7	15

Summary of the VisuMet results of the pellet samples:

Samples	Nr. Images	%-pore <2μm ø	Pore [%]	Glass [%]	Fe Oxide [%]
RR9_1	299	4	48	14	38
RR9_2	248	3	47	14	39
PO8	564	3	38	9	53
CV7	510	1	31	13	56
MP3	528	1	38	5	57
KP6	529	2	36	5	59
TU5	582	1	34	5	61
TA4	585	1	27	6	67
AL2_1	394	3	32	10	58
AL2_2	368	2	36	10	54
BR1	579	1	31	13	56

Curriculum Vitae

Birgit Kain-Bückner (formally Birgit Kain)

Date of birth: 10th December 1984

Education

2012-2018	Doctoral Thesis, Chair of Geology and Economic Geology, Montanuniversitaet Leoben
2003-2010	Academic studies at the Montanuniversitaet Leoben, Bachelor and Masterstudy (passed with distinction) Applied Geoscience
	Master Thesis at Chair of Resource Mineralogy
	Bachelor Thesis I at Chair of Geology and Economic Geology
	Bachelor Thesis II at Chair of Resource Mineralogy
2003	Higher School Certificate
2003-1999	Higher School BORG Kindberg, Hammerbachgasse 12, 8650 Kindberg
1995-1999	Secondary modern school Kindberg
1991-1995	Elementary School Kindberg

Work Experience:

2015- ongoing	Researcher, K1-Met GmbH, Leoben
2012–2015	Research Assistant, Montanuniversitaet Leoben, Chair of Geology and Economic Geology; Doctoral Thesis within the K1-Met metallurgical competence centre
2010-2011	Freelancer at Mag. Kurt Stadlober, Office for Technical Geology
2006–2010	Partially employed at Mag. Kurt Stadlober, Office for Technical Geology
2003-2006	Internships for one month at Böhlerit GmbH & Co KG (3 times), OMYA (1 time)

Publications

B. Kain-Bückner, H. Mali, M. Hanel, J. Schenk, F. Hauzenberger, H. Stocker, C. Thaler: Charakterisierung von Rohmaterialien für die Eisenerzherstellung mit Bildverarbeitung. – BHM 158, 2013

B. Kain-Bückner, G Rantitsch, M. Hanel, H. Mali, J. Schenk, H. Stocker, C. Thaler, F. Hauzenberger: Characterization of raw materials for efficient use in iron making processes. – K1-MET Scientific Exchange Day 2013

B. Kain-Bückner, H.Mali, J.Schenk, F.Hauzenberger, C.Thaler, H.Stocker: Image analysis for evaluation of iron ore carriers. – Prakt. Met. Sonderband 46 (2014)

B. Kain-Bückner, M. Hanel, H. Mali: Charakterisierung von Eisenträgern mittels Bildverarbeitung - Mitt.Österr.Miner.Ges. 161 (2015)

Hanel, M, Kain-Bückner, B, Schenk, J, Mali, H, Hauzenberger, F, Thaler, C & Stocker, H 'Chemistry vs. Morphology vs. Reducibility — Some (Non-) Existing Correlations' Beitrag in AISTech, Indianapolis, Indiana, 2015, 4/05/14 - 8/05/14, S. 593-602.

B. Kain-Bückner, H. Mali: VisuMet – analyses of lumpy iron carriers with image processing – Iron Ore 2017, Perth, p.557-560.